U.S. Department
of Transportation
Federal Railroad
Administration

Office of Research,
Development and Technology
Washington, DC 20590

Improving Tank Car Crash Energy Management (CEM)

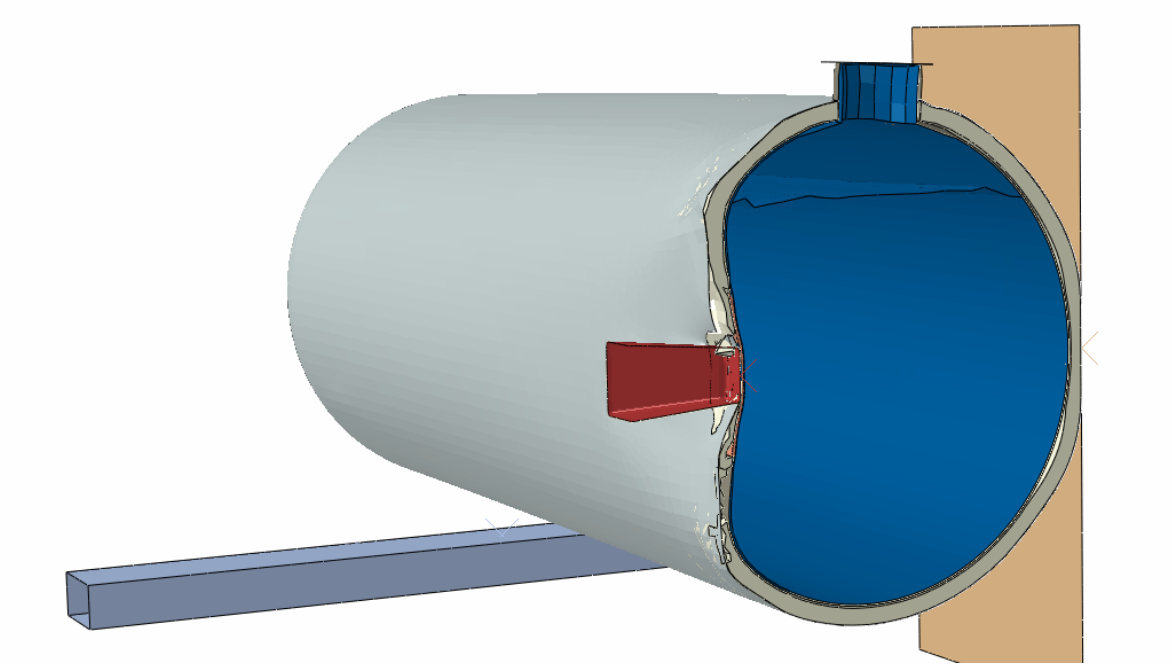

DOT/FRA/ORD-24-05

Final Report | February 2024

REPORT DOCUMENTATION PAGE

Form Approved OMB No. 0704-0188

1. REPORT DATE *(DD-MM-YYYY)*	2. REPORT TYPE	3. DATES COVERED *(From - To)*
2/1/24	Technical Report	08/12/2020 to 08/31/2022

4. TITLE AND SUBTITLE

Improving Crash Energy Management (CEM) of Tank Cars

5a. CONTRACT NUMBER
693JJ620C000011

5b. GRANT NUMBER

5c. PROGRAM ELEMENT NUMBER

6. AUTHOR(S)
Philip S. Taylor – ORCID: 0000-0002-8043-6546
Juan Londono – ORCID: 0000-0003-2467-4686l
Pawel Woelke – ORCID: 0000-0003-0114-9635
John W. Hutchinson – ORCID: 0000-0001-6435-3612
David Tyrell – ORCID: 0000-0001-8156-0277
David Jeong – ORCID: 0000-0003-3514-5739

5d. PROJECT NUMBER

5e. TASK NUMBER

5f. WORK UNIT NUMBER

7. PERFORMING ORGANIZATION NAME(S) AND ADDRESS(ES)
Thornton Tomasetti Inc
120 Broadway,
New York NY 10271

8. PERFORMING ORGANIZATION REPORT NUMBER
NN20212.00-R-01

9. SPONSORING/MONITORING AGENCY NAME(S) AND ADDRESS(ES)
U.S. Department of Transportation
Federal Railroad Administration
Office of Railroad Policy and Development
Office of Research, Development and Technology
Washington, DC 20590

10. SPONSOR/MONITOR'S ACRONYM(S)

11. SPONSOR/MONITOR'S REPORT NUMBER(S)
DOT/FRA/ORD-24-05

12. DISTRIBUTION/AVAILABILITY STATEMENT
This document is available to the public through the FRA website.

13. SUPPLEMENTARY NOTES
COR: Francisco González, III

14. ABSTRACT
The Federal Railroad Administration sponsored a 2-year research effort between August 2020 and August 2022 to investigate multiple mitigation concepts for hazmat tank cars, aimed at improving their puncture resistance. The team first developed and validated a finite element (FE) model of a full-scale tank car subject to shell (i.e., side) impact. Researchers then evaluated the effectiveness of different mitigation solutions by exercising the validated FE model. Validated FE models were used to explore different solutions including key material properties of tank car steel, the effects of changing shell thickness, the effects of splitting a single thick plate into multiple plates, and internal liner solutions. Results indicated the key parameter to improving puncture resistance is to increase total steel thickness; however, a double-tank arrangement offers improved benefit over an equivalent monolithic shell because of the high strength or high ductility steel used for the outer layer. Moreover, FE analyses indicated the ductility of steel in plane strain bending reduces with increasing plate thickness; the resistance of thick shells may be over-estimated if this is not considered.

15. SUBJECT TERMS
Rolling stock research, FEA, mitigation, hazmat, tank car, puncture resistance, TC128-B

16. SECURITY CLASSIFICATION OF:			17. LIMITATION OF ABSTRACT	18. NUMBER OF PAGES	19a. NAME OF RESPONSIBLE PERSON
a. REPORT	b. ABSTRACT	c. THIS PAGE		136	Francisco González, III
					19b. TELEPHONE NUMBER *(Include area code)* 202-493-6076

Standard Form 298 (Rev. 8/98)
Prescribed by ANSI Std. Z39.18

METRIC/ENGLISH CONVERSION FACTORS

ENGLISH TO METRIC	METRIC TO ENGLISH
LENGTH (APPROXIMATE)	**LENGTH (APPROXIMATE)**
1 inch (in) = 2.5 centimeters (cm)	1 millimeter (mm) = 0.04 inch (in)
1 foot (ft) = 30 centimeters (cm)	1 centimeter (cm) = 0.4 inch (in)
1 yard (yd) = 0.9 meter (m)	1 meter (m) = 3.3 feet (ft)
1 mile (mi) = 1.6 kilometers (km)	1 meter (m) = 1.1 yards (yd)
	1 kilometer (km) = 0.6 mile (mi)
AREA (APPROXIMATE)	**AREA (APPROXIMATE)**
1 square inch (sq in, in^2) = 6.5 square centimeters (cm^2)	1 square centimeter (cm^2) = 0.16 square inch (sq in, in^2)
1 square foot (sq ft, ft^2) = 0.09 square meter (m^2)	1 square meter (m^2) = 1.2 square yards (sq yd, yd^2)
1 square yard (sq yd, yd^2) = 0.8 square meter (m^2)	1 square kilometer (km^2) = 0.4 square mile (sq mi, mi^2)
1 square mile (sq mi, mi^2) = 2.6 square kilometers (km^2)	10,000 square meters (m^2) = 1 hectare (ha) = 2.5 acres
1 acre = 0.4 hectare (he) = 4,000 square meters (m^2)	
MASS - WEIGHT (APPROXIMATE)	**MASS - WEIGHT (APPROXIMATE)**
1 ounce (oz) = 28 grams (gm)	1 gram (gm) = 0.036 ounce (oz)
1 pound (lb) = 0.45 kilogram (kg)	1 kilogram (kg) = 2.2 pounds (lb)
1 short ton = 2,000 pounds (lb) = 0.9 tonne (t)	1 tonne (t) = 1,000 kilograms (kg)
	= 1.1 short tons
VOLUME (APPROXIMATE)	**VOLUME (APPROXIMATE)**
1 teaspoon (tsp) = 5 milliliters (ml)	1 milliliter (ml) = 0.03 fluid ounce (fl oz)
1 tablespoon (tbsp) = 15 milliliters (ml)	1 liter (l) = 2.1 pints (pt)
1 fluid ounce (fl oz) = 30 milliliters (ml)	1 liter (l) = 1.06 quarts (qt)
1 cup (c) = 0.24 liter (l)	1 liter (l) = 0.26 gallon (gal)
1 pint (pt) = 0.47 liter (l)	
1 quart (qt) = 0.96 liter (l)	
1 gallon (gal) = 3.8 liters (l)	
1 cubic foot (cu ft, ft^3) = 0.03 cubic meter (m^3)	1 cubic meter (m^3) = 36 cubic feet (cu ft, ft^3)
1 cubic yard (cu yd, yd^3) = 0.76 cubic meter (m^3)	1 cubic meter (m^3) = 1.3 cubic yards (cu yd, yd^3)
TEMPERATURE (EXACT)	**TEMPERATURE (EXACT)**
[(x-32)(5/9)] °F = y °C	[(9/5) y + 32] °C = x °F

QUICK INCH - CENTIMETER LENGTH CONVERSION

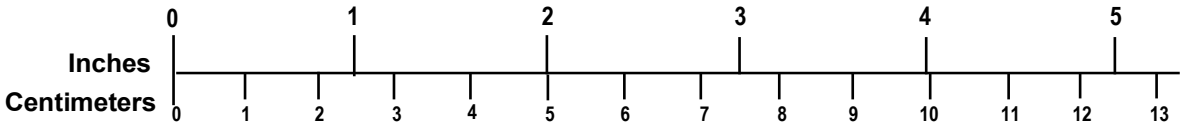

QUICK FAHRENHEIT - CELSIUS TEMPERATURE CONVERSIO

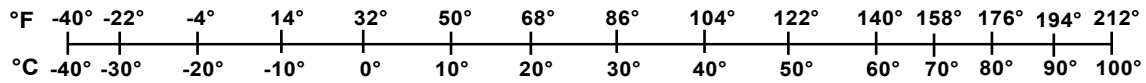

For more exact and or other conversion factors, see NIST Miscellaneous Publication 286, Units of Weights and Measures. Price $2.50 SD Catalog No. C13 10286

Acknowledgements

The authors gratefully acknowledge the technical contributions and guidance provided by Michael Carolan, Volpe National Transportation Systems, and Francisco González, III FRA, throughout the research. In particular, previous work undertaken by Michael Carolan and subsequent guidance in developing a robust mechanism for developing and validating a full-scale finite element model of tank car puncture was invaluable to the project.

Contents

Illustrations

Tables

Executive Summary

The increasing volume of rail transport inevitably leads to an increased number of accidents, which raises safety concerns and presents challenges related to hazmat transportation. In the event of an accident or derailment, the puncture resistance of the tank is key to preventing hazmat release and escalation of the incident.

The Federal Railroad Administration (FRA) sponsored a 2-year research effort led by Thornton Tomasetti (TT) to investigate multiple mitigation concepts for hazmat tank cars, aimed at improving their puncture resistance. The research was conducted between August 2020 and August 2022. The team first developed and validated a finite element (FE) model of a full-scale tank car subject to shell (i.e., side) impact. Researchers then evaluated the effectiveness of different mitigation solutions by exercising the validated FE model.

The team used a side impact test of a water-filled DOT-105 tank car in the validation exercise to establish the baseline condition. The tank car featured a 0.775-inch-thick TC128-B steel shell that was tested for puncture resistance, achieving puncture of the shell at 15.16 mph. A survival speed of 13.0 mph was subsequently calculated using the validated FE model.

The team then assessed a new low-carbon version of TC128-B steel developed by ArcelorMittal (AM). The new steel featured higher ductility and reduced strength and AM had predicted it would provide 12 - 14 percent improvement in puncture energy. Using information published by AM, the research team evaluated the performance of this new steel in comparison to the baseline. The calculated improvement in puncture energy was very similar to that estimated by AM, representing an incremental improvement in the puncture resistance of tank cars.

Considering the available tank car space and weight constraints, one of the simplest theoretical ways to address puncture resistance would be to increase the thickness of the tank shell. This applies to the design of new tank cars only, and the tank car industry has made generational improvements in which head and shell thickness have been increased. The team investigated this option by increasing the tank shell thickness to 1.5 inches and calculating the tank car response to side impact. A survival speed of approximately 22 - 23 mph (an approximate threefold increase in energy) was achieved using around 90 percent of the available weight.

Recognizing the challenges related to manufacturing a tank car with 1.5-inch-thick shell, researchers conducted a parametric study to investigate the effect of increased ductility and strength. In both cases, the puncture energy approximately doubled, with survival speeds increasing to 19 mph and 20 mph for the high ductility and high strength materials, respectively. These findings are consistent with those of previous researchers.

The team also considered implementing a multi-layer (i.e., tank-within-a-tank) approach. The results indicated that in various configurations the survival speed could approximately match that of the 1.5-inch-thick shell provided that the total steel thickness was consistent. Researchers found that splitting the outer plates into a series of rings did not significantly change the puncture resistance. One significant benefit the multi-layer solution offers is the use of increased strength or ductility steels for the outer layers. Additionally, a numerical investigation of the effect of plate thickness on ductility showed that increasing the thickness can significantly reduce ductility in bending. Applying a multi-layer solution avoids this ductility penalty.

Team members also investigated the use of an internal tank car liner, which appeared potentially effective purely as a containment mechanism in the event of puncture (i.e., no improvement in puncture speed was observed). Researchers also considered mitigation solutions aimed at blunting the indenter, finding the effectiveness of this approach similar to increasing the shell thickness, but with significant added complexity and cost. Therefore, the team does not recommend pursuing mitigation solutions aimed primarily at blunting.

In summary, the most promising mitigation approach to improve tank car puncture resistance is likely to be the multi-layer (i.e., tank-within-a-tank) approach, in which different steel grades can be used for the outer layers with the specific purpose of enhancing the overall puncture resistance of the tank car. These findings match one of the key findings of the Advanced Tank Car Collaborative Research Program (ATCCRP), although it is not yet clear what level of puncture resistance may be achieved using this approach. The team recommends further research to investigate the level of puncture resistance possible using the multi-layer approach.

1. Introduction

This report documents a 2-year research effort funded by the Federal Railroad Administration (FRA) to investigate multiple mitigation concepts for tank cars to improve their puncture resistance. The research was conducted between August 2020 and August 2022 and was led by Thornton Tomasetti (TT), an engineering consulting firm with extensive experience in the design and assessment of various structural systems subjected to extreme loads. TT was supported by independent project consultants Dr. David Jeong and David Tyrell, both of whom had contributed significantly to previous tank car integrity research efforts. The team was further supported by Prof. John Hutchinson, a renowned expert in the field of solid mechanics.

1.1 Background

Increasing volume of rail transport inevitably leads to an increased number of accidents, which raises safety concerns and illustrates the challenges related to hazmat transportation. Most of the accidents that have occurred since the Minot, North Dakota, derailment on January 18, 2002, have involved two main classes of hazmat: (1) toxic inhalation hazmat (TIH), also referred to as poison inhalation hazardous (PIH) materials (e.g., anhydrous ammonia – Minot [1]); and (2) flammable liquids (primarily crude oil and ethanol). In the case of the latter, rapid expansion of oil extraction from the Bakken Shale site in North Dakota beginning in 2006 led to a more than tenfold increase in the volume of crude oil transportation via unit trains (i.e., trains with all cars carrying the same commodity, shipped from the same origin to the same destination). This led to a significant increase in accidents resulting in hazmat release; some key accidents are summarized in Table 1.

Table 1. Selection of Hazmat Accidents

Date	Location	Hazmat	Reference
10/20/2006	New Brighton, PA	Ethanol	[2]
10/10/2007	Painesville, OH	Ethanol	[3]
06/19/2009	Cherry Valley, IL	Ethanol	[4]
10/07/2011	Tiskilwa, IA	Ethanol	[5]
07/11/2012	Columbus, OH	Ethanol	[6]
12/30/2013	Casselton, ND	Crude Oil	[7]
07/06/2013	Lac-Mégantic, Quebec	Crude Oil	[8]

A particularly disastrous accident occurred in 2013 in Lac-Mégantic, Quebec, Canada, which involved the derailment of an unsecured (i.e., runaway) train [8]. In total, 16 significant accidents (9 involving crude oil and 7 involving ethanol) occurred between October 2006 and February 2014. The consequences of these 16 accidents included 48 fatalities, 281 DOT-111 tank cars derailed, 2.8 million gallons of crude oil released, and 2.0 million gallons of ethanol released. Selected examples of specific accident effects and hazmat release are shown in Figure 1.

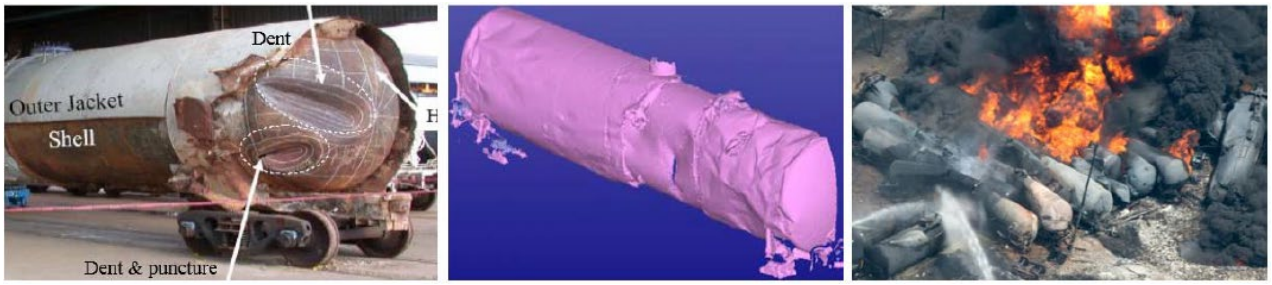

Figure 1. Left to Right: Macdona, TX, Accident – Head Puncture [9]; Granitville, SC, Accident – Shell Puncture [10]; Lac-Mégantic, Canada, Car Pileup [8]

Prior to these accidents, FRA tank car safety research had focused on maintaining tank integrity under normal tank car operating conditions (e.g., fatigue crack propagation). However, most of the hazmat releases discussed above occurred during derailment where the car coupler and/or broken rail impacted the tank car shell causing its puncture. This presents an entirely different problem than pressurization cycles and fatigue cracks and requires investigation of tank car crashworthiness and structural integrity when subjected to the extreme loading conditions of derailments and collisions. Thus, government- and industry-sponsored research shifted toward these topics, focusing specifically on puncture resistance and maintaining tank car integrity during derailments. In 2006, the Next Generation Rail Tank Car Project (NGRTCP) was begun as an industry research and development effort under the sponsorship of Dow Chemical Company, Union Pacific Railroad (UP), and Union Tank Car Company (UTLX).

Later in 2006, FRA and the Pipeline and Hazardous Materials Safety Administration (PHMSA) initiated a Notice of Proposed Rulemaking (NPRM) for transporting hazmat by railroad tank cars [11]. In 2007, FRA and Transport Canada (TC) signed a Memorandum of Cooperation (MOC) to participate in the NGRTCP with the understanding that the research results would be used to support rulemaking for North American regulatory agencies (i.e., FRA and TC) and to help develop improved tank car designs for the railroad tank car industry. In 2009, the Advanced Tank Car Collaborative Research Program (ATCCRP) was initiated as another joint industry effort by the Association of American Railroads (AAR) and is still on-going. In 2015, the U.S. Department of Transportation (USDOT) released a final safety rule governing the transportation of flammable liquids by rail, primarily crude oil and ethanol [12]. The rule stipulated that new tank cars constructed after October 1, 2015, must meet design and performance requirements for a new USDOT specification, DOT-117 (in Canada, the new class of tank car is designated as TC-117).

While all these government- and industry-led activities resulted in improved safety in hazmat transportation by rail, many challenges remain. One of the most important of these challenges is related to operation of the existing fleet of tank cars, both in the US and Canada, which were constructed before 2015.

Throughout these government- and industry-led impact test activities, both head and shell (i.e., side) impact scenarios were investigated in detail, although the technology for head impact protection can be considered at a more advanced stage than that for shell impact protection. This is mainly due to prior research into tank car head vulnerability resulting in federal regulations instituted in the 1980s requiring head shields to protect railroad tank cars carrying certain classes of hazardous materials [13]. Introduction of the head shields has led to improved safety of hazmat transport by rail through the significant reduction of the conditional probability of release

for head losses (for unshielded heads) [14]. More recent efforts to improve puncture resistance built on that experience and validated performance improvements for both head and shell impacts.

One of the most important steps to improve tank car puncture resistance is to identify the critical collision conditions and loading scenarios. As done previously for head impact, shell impact scenarios were identified by examining past accidents with the most severe impact conditions. Examples of these accidents are shown in Figure 2 [15].

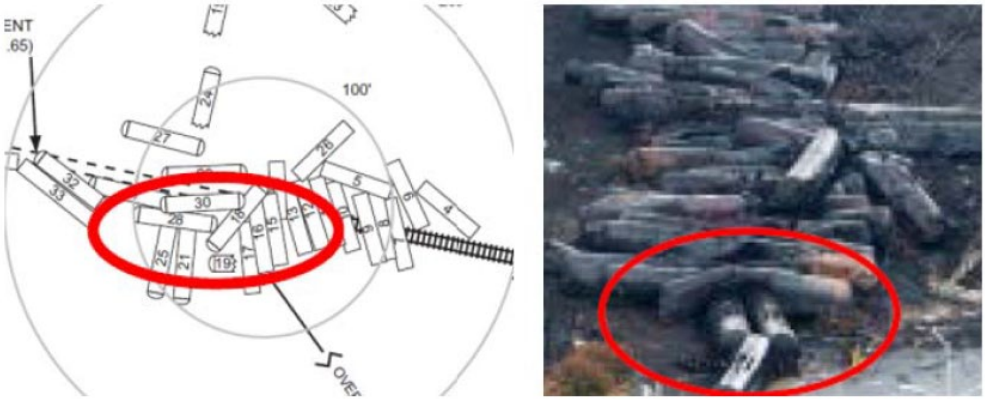

Figure 2. Derailment Pileups, Left To Right: Minot, ND, 2002; Lac-Mégantic Car Pileup

These considerations led to the development of a shell impact scenario and full-scale testing protocol analogous to the head impact test stipulated in Code of Federal Regulations (CFR) §179.16 [13]. The regulations describe a general coupler-head impact test in which a moving ram car with a minimum weight of 263,000 lb strikes the head of a subject tank car below the centerline of the head. The subject tank car, with its brakes released, is braced by three fully loaded backup cars with their brakes applied. Additionally, Appendix A to Part 179 [13] describes a test procedure to verify the head puncture resistance and system survivability after coupler-to-tank impacts at a relative speed of 18 mph.

A similar test setup has been proposed for shell impacts. In the shell impact scenario, which is a subject of ongoing research (and not yet subject to any existing regulation), a moving ram car strikes the side of a subject tank car at its centerline, with the subject car braced against a rigid barrier (Figure 3). This scenario was conceived as an idealized, full-scale, side impact test that would result in puncture and other failure modes that occur in actual accidents. Other important considerations of the shell impact test include safety, repeatability, controllability, and the ability to numerically simulate the test conditions and tank car response. Since 2007, a series of full-scale shell impact tests have been performed along with an extensive simulation effort and small-scale lab experiments to investigate the conditions experienced during possible crash and impact scenarios.

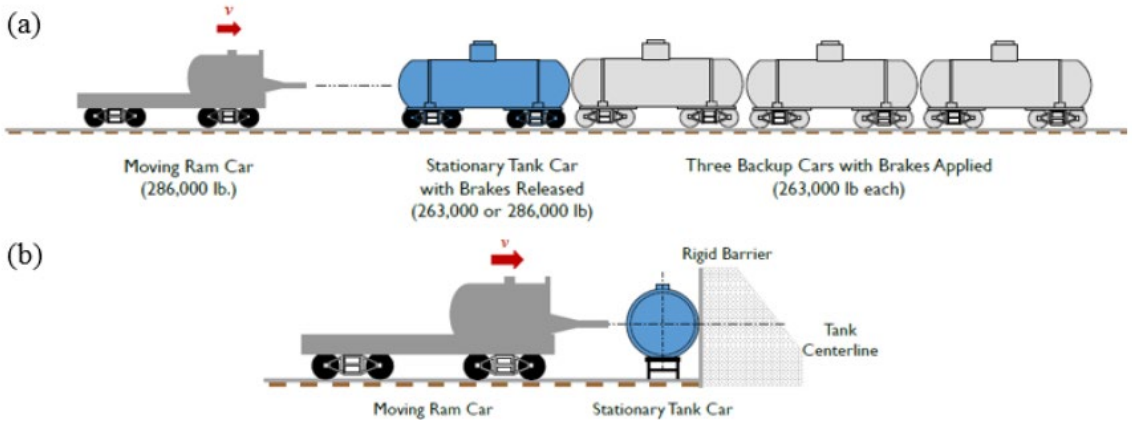

Figure 3. Generalized Impact Scenarios: (a) Head – CFR §179.16 [13], and (b) Shell – Ongoing Research [15]

Alongside full-scale impact tests, the team undertook parallel work to evaluate the behavior of current design equipment in these scenarios and to develop mitigation strategies aimed at doubling the maximum impact speed for which tank integrity is maintained and/or hazmat is contained. A general framework was developed for screening and evaluating potentially improved designs [16]. The key design functions of different mitigation strategies were:

1. Blunting the impact loads
2. Absorption of the collision energy
3. Tank strengthening
4. Controlling the load path

Researchers proposed specific design features and concepts and evaluated their ability to achieve these functions. These included innovative solutions such as sacrificial panels and shields (addressing 1 and 2 above), head and shell reinforcements (addressing 3), and carbody redesign to allow the support of service loads [16]. An initial integrated concept design was also developed, with tank strengthening, load blunting, energy dissipation measures, and an auxiliary structural system to carry the service loads as well as impact within the existing weight and space constraints [17]. The integrated concept design (Figure 4) included not only performance during impact, but also feasibility, scalability, and cost.

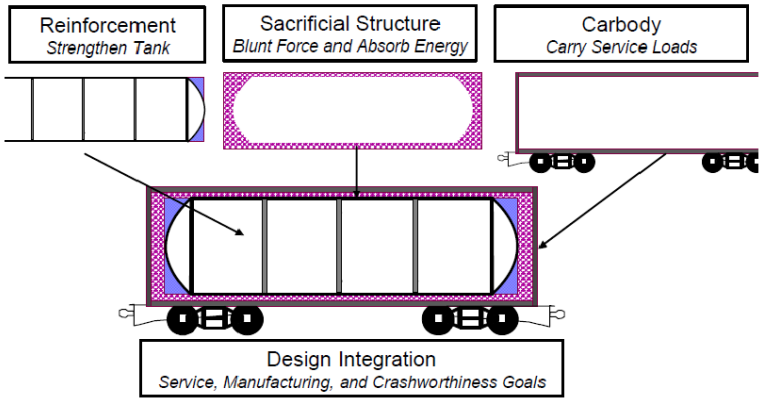

Figure 4. Schematic Illustration of Integrated Conceptual Design [17]

To address the multiple design functions discussed above, researchers investigated engineered sandwich panels with multiple geometries and core features [18], [19], [20], [21]. A detailed experimental and numerical study was performed, culminating in full-scale testing to demonstrate the concept [22]. Figure 5 shows a basic design concept with a structural carbody including the sandwich panels and the full-scale test setup.

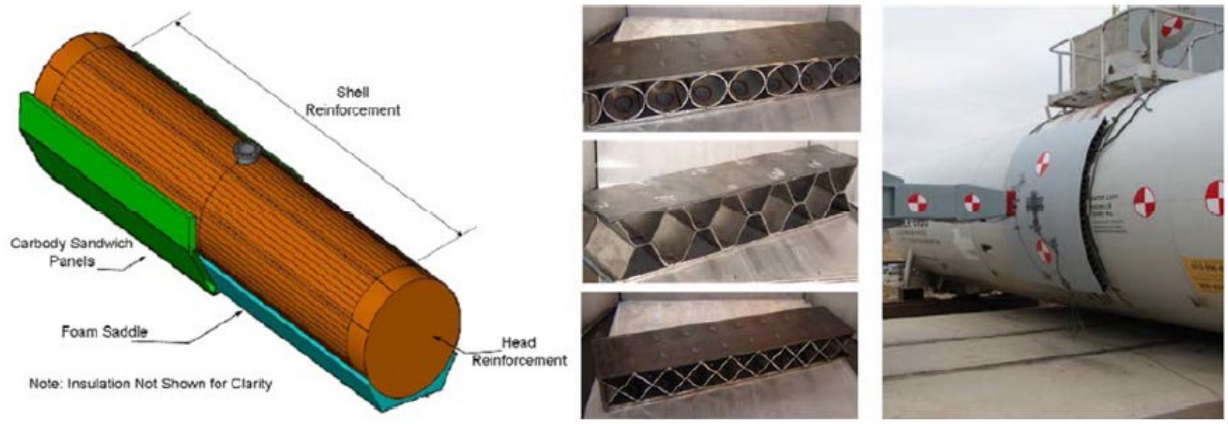

Figure 5. Use of Sandwich Panels to Improve Tank Car Integrity [18], [19], [22]

Most of the conceptual developments discussed above were accomplished through a combination of detailed finite element (FE) simulations and experimental testing. This required significant advancement of the appropriate approaches to simulate the response of the tank car components, including the mitigation elements [22], [23]. One of the most important components of the effective simulation of tank car response to localized impact is accurate representation of material failure on a large scale.

Significant effort was made to characterize the tank car material response (TC128-B steel) and calibrate the appropriate constitutive model [24], building on recent advances in understanding of the ductile failure of metals [25], [26].

1.2 Objectives

The overall objective of the research was to provide fundamental insights into the design and integrity of tank cars subjected to localized impact to make tank car manufacturers and rule makers aware of the potential puncture resistance enhancements that are achievable by changing different parameters of tank car design. A further objective was to evaluate potential mitigation measures for the existing fleet of tank cars.

1.3 Overall Approach

The overall approach adopted in this research was to investigate different mitigation solutions using FE methods. Recent full-scale testing and associated numerical simulations conducted in related research enabled the team to efficiently develop validated full-scale FE models of the side impact test. These models were used to evaluate the effectiveness of various mitigation solutions with a high degree of confidence. The different material properties of steel that contribute to puncture resistance were investigated, as were the effects of varying steel thickness and splitting plates into multiple layers. This led to an investigation of the relationship between steel thickness and ductility, with ductility having been found to strongly influence puncture resistance.

1.4 Scope

The research focused on mitigation of the side impact case specifically in relation to pressurized hazmat tank cars; however, the findings are considered relatable to non-pressurized tank cars.

1.5 Organization of the Report

The report is arranged as follows:

- Section 2 provides background into the history of side impact testing and details the steps undertaken to develop and validate a full-scale FE model of a DOT-105 tank car.
- Section 3 details the development of a more efficient sub-model for use in subsequent mitigation analyses.
- Section 4 documents the methodology for and results from a series of mitigation analyses.
- Section 5 describes an investigation into the relationship between ductility and plate thickness.
- Section 6 considers the feasibility, cost, and scalability of the most promising mitigation solutions.
- Section 7 summarizes the key conclusions.
- Supplementary information is supplied in Appendices A through D.

2. Development of a Full-Scale Finite Element Model

To evaluate the effectiveness of different mitigation measures, it was necessary for the team to develop a well-validated FE model upon which the selected solutions could be tested. This section describes the selection, development, and verification of a full-scale FE model.

2.1 Full-Scale Tests

Since 2007, FRA has been working collaboratively with industry research partners to undertake a series of full-scale shell (i.e., side) impact tests to improve the understanding of tank car impact behavior and puncture resistance. The tests were conducted at FRA's Transportation Technology Center, Inc. (TTCI), in Pueblo, Colorado, and have been accompanied by FE analysis (FEA) primarily performed at USDOT's National Transportation Systems Center (Volpe)[1].

A table summarizing the tank car shell impact tests is shown in Table 2.

Table 2. Summary of Tank Car Shell Impact Tests [27]

Test #	Test Date	Specification	Impact Speed (mph)	Impactor Size (inches)
1	4/26/2007	DOT-105	14.0	17 x 23
2	7/11/2007	DOT-105	15.1	6 x 6
3	5/18/2011	DOT-105 (w/ panel)	17.8	12 x 12
4	12/18/2013	DOT-111	14.0	12 x 12
5	2/26/2014	DOT-112	14.7	12 x 12
6	4/27/2016	DOT-105	15.2	12 x 12
7	9/28/2016	DOT-117	13.9	12 x 12
8	8/1/2018	DOT-105	9.7	6 x 6
9	10/30/2018	DOT-111 (CPC-1232)	13.9	12 x 12
10	11/19/2019	DOT-113	16.7	12 x 12
11	6/11/2020	DOT-113 (surrogate)	17.3	12 x 12
12	07/24/2021	DOT-113 (surrogate)	18.3	12 x 12

As shown in Table 2, researchers physically tested various tank car specifications, with 5 of the 12 tests involving DOT-105 tank cars. DOT-105 are insulated tank cars that carry pressurized gases (often TIH materials) and are slightly smaller than the non-pressurized DOT-111 and DOT-117 tank cars that carry flammable liquids. DOT-112 is a pressurized tank car, like DOT-105, while DOT-113 is a double-walled tank car designed to transport cryogenic liquids. The number of DOT-113 tank cars in service is very small in comparison to the other specifications

[1] FEA for Tests 1, 2, and 4 was performed by Applied Research Associates, Inc.

(approximately 67 in 2020 [28]), although this number is expected to increase following FRA's Final Rule (July 24, 2020 [29]) permitting transportation of liquified natural gas (LNG) by rail in DOT-113C120W specification cars.

The team chose to use the DOT-105 specification for the development of a full-scale FE model after four different impactor sizes were considered. The team chose DOT-115 because it was the most tested specification, had been tested with sandwich panels aimed at improving puncture resistance (Test 3), and recent FRA tests and analyses provided great detail on the methods for developing a validated full-scale FE model using this specification [30], [31]. Specifically, the full-scale FE model developed during this research was to align with prior Tests 6 and 8. These tests, and the accompanying analysis reports [30], [31], were commissioned by FRA with the intention of generating useful data for researchers and entities seeking to develop validated and verified FE models.

2.2 Tests 6 and 8 Overview

Tests 6 and 8 in Table 2 involved DOT-105 tank cars constructed between 1979 and 1980 and equipped with both head protection and foam insulation within the exterior jacket. The 0.775-inch-thick tank car shell was constructed from TC-128 Grade B steel and the internal diameter was 100.45 inches. The tank was covered with a 4-inch-thick layer of foam enclosed within an 11-gauge steel jacket. An example of the general arrangement for a DOT-105 tank car is shown in Figure 6 [32].

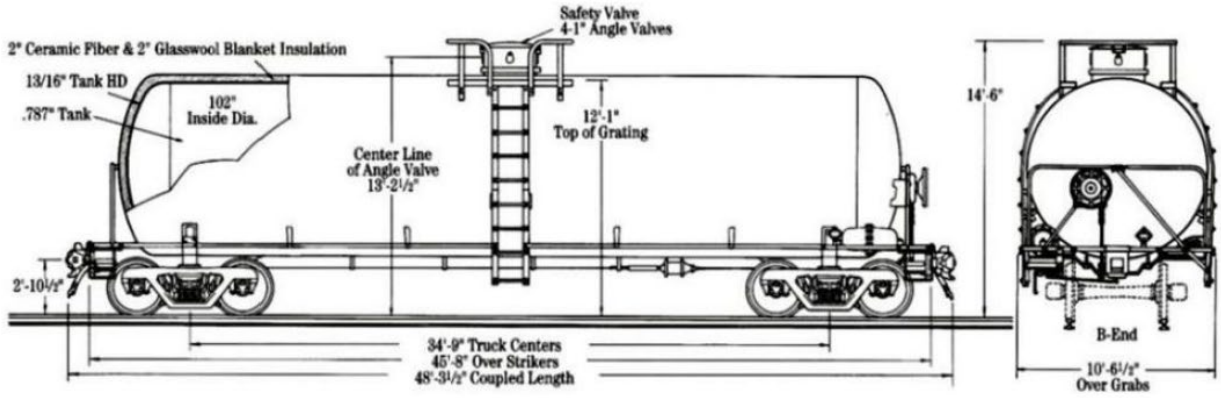

Figure 6. Example DOT-105 Tank Car Design Specification [32]

In both tests, the tank cars were water-filled to an outage of 10.6 percent. The manhole lid was sealed and the car was pressurized to 100 psi before the test. The indenters were positioned to align with the mid-length and mid-height of the target, with a 12 x 12-inch indenter used in Test 6, and a 6 x 6-inch indenter used in Test 8. The indenters were fitted to the head of a ram car (Figure 7), which weighed 297,125 lb in Test 6 and 296,775 lb in Test 8. The measured impact speeds of the ram cars were 15.2 and 9.7 mph for Tests 6 and 8, respectively.

The tank cars were supported on two support skids, with four sections of I-beams welded to the underside of the tank car to facilitate sliding and minimize rollback (Figure 8). The tank cars were lifted into position by crane and positioned as close as possible to the rigid wall behind. They were instrumented with triaxial accelerometers, pressure transducers, speed sensors, and string potentiometers at various locations. High speed cameras were used to record the tests.

Figure 7. Photograph of a Ram Car and Head Fitted with 6 x 6-inch Indenter [30]

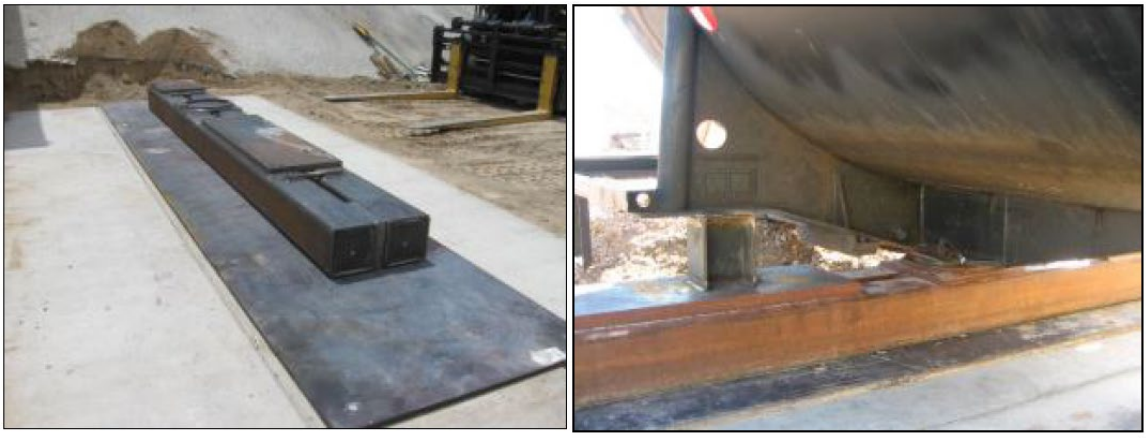

Figure 8. Tank Support Skid System [30]

In both tests (Figure 9 and Figure 10), the tank cars punctured, with the ram car rebounding after impact. The impact speeds were selected based on pre-test estimates from FE simulations; the occurrence of rebound indicates that the impact speed was close to the puncture speed in both cases. Post-test simulations that incorporated refined material models using samples extracted from the tank shell showed very good agreement with the physical test results. The detailed methodology developed in previous research ([30], [31]) for full-scale FE models in Tests 6 and 8 was followed in this research effort to establish a baseline full-scale model that was well understood and verified. This is discussed in Section 3.3.

Figure 9. Deformed Tank Just Prior to Puncture (12 x 12-inch Indenter) [30]

Figure 10. Deformed Tank Just Prior to Puncture (6 x 6-inch Indenter) [30]

2.3 Full-scale FE Model

An overview of the full-scale FE model is shown in Figure 11 and Figure 12. The team developed the model using the commercial FE software package Abaqus (2020), with the model geometry developed using the Abaqus/CAE preprocessor and dynamic analyses undertaken using the Abaqus/Explicit solver. A half-symmetry model was developed, using the same techniques used in [30] and [31].

The model comprises a 0.775-inch-thick tank shell predominantly modelled using shell elements, with a local region modelled using solid elements at the impact location. Internally, there is a fluid cavity modelled using membrane elements, with a separation between water and air cavities giving an outage of 10.6 percent. The air cavity is pressurized to 100 psi. External to the tank shell is a 4-inch-thick layer of foam modelled using solid elements, and outside of the foam is a 0.1196-inch-thick jacket modelled using shell elements. A single rigid skid is connected to a section of the tank shell near the head, and directly behind the tank assembly is a discrete rigid wall. Further detail of the model development is provided in the following sections.

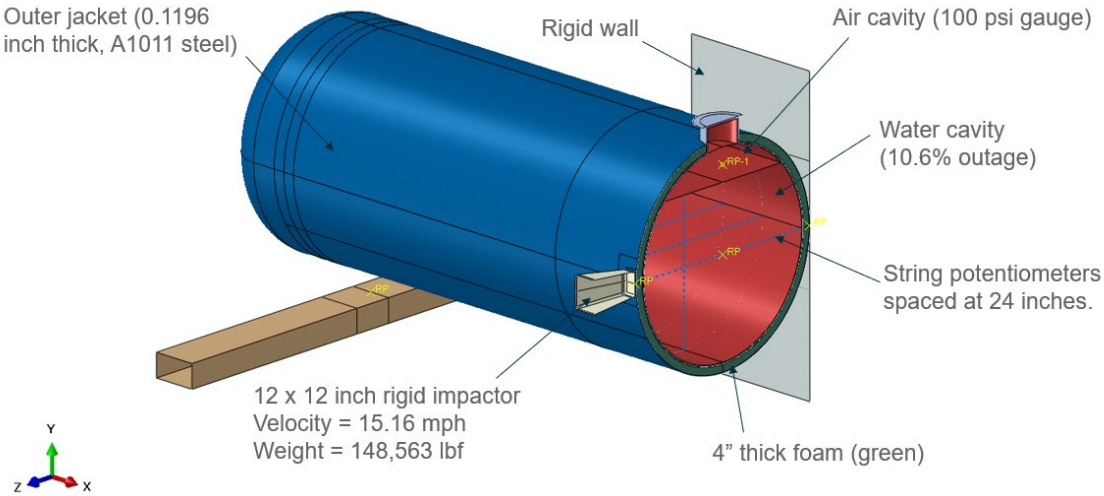

Figure 11. Overview of Full-scale FE Model, Test 6

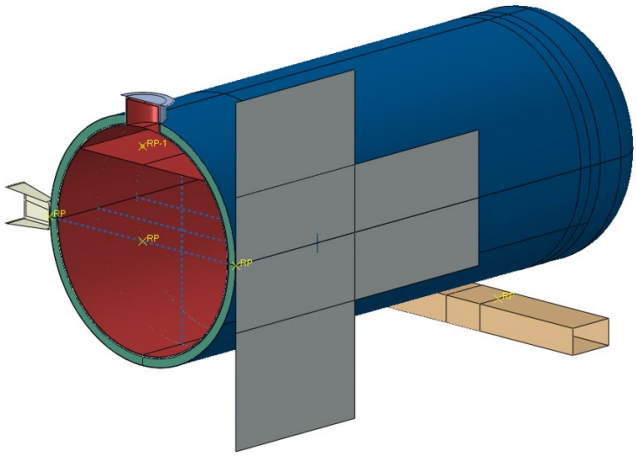

Figure 12. Overview of Full-scale FE Model from Behind, Test 6

2.3.1 Geometry

The geometry of the tank shell is shown in Figure 13. It was developed using mid-surface shells, with a local region behind the impactor replaced with a solid element region, as shown in Figure 14. The tank body (cylindrical portion) was modelled using a shell thickness of 0.775 inches, with the 2:1 elliptical head modelled using a shell thickness of 0.8125 inches. A 20-inch diameter manway was centered and extruded 11.5 inches from the top of the tank. The vertical, cylindrical portion of the manway had a plate thickness of 1 inch, as did the manway cover plate. Directly below the manway, within a circular region with a diameter of 39 inches, the shell thickness was doubled. The circular partition for this region can be seen in Figure 14. The tank shell geometry was used as the baseline from which to create offset geometries to define the 4-inch-thick foam layer, the 0.1196-inch-thick jacket, and the internal membrane.

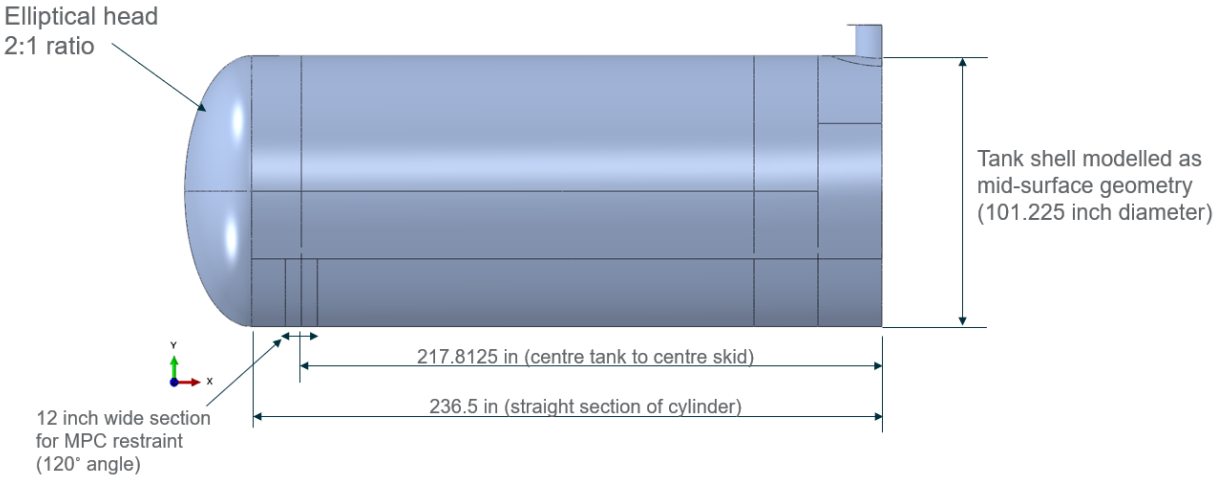

Figure 13. Elevation Showing Tank Shell Geometry

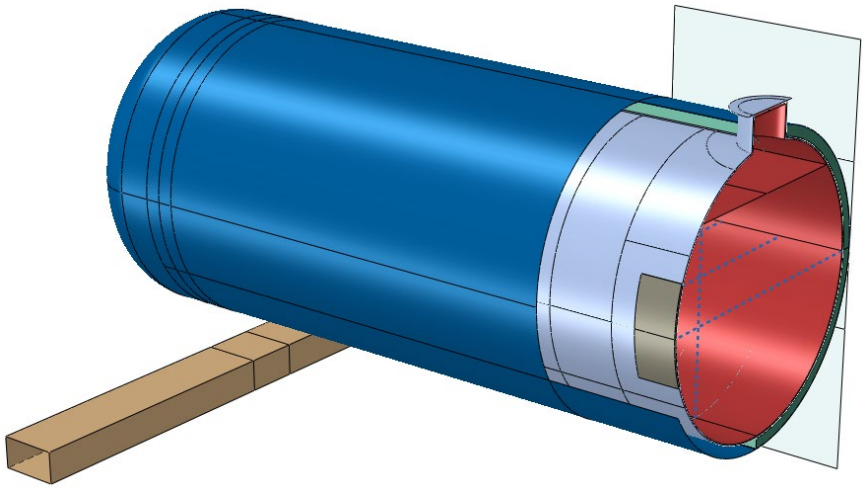

Figure 14. Isometric View of Tank Car Assembly, with Sections of Jacket (blue) And Foam (green) Removed to Show Tank Shell with a Local Solid Region

2.3.2 *Indenter*

The geometry and associated mesh used for the 12 x 12-inch indenter is shown in Figure 15. The indenter was modelled as a discrete rigid part and in Test 6 it was assigned a weight of 148,563 lbf (i.e., half of the total mass) due to the use of a symmetry plane. The 12-inch indenter features a 1-inch radius on the face so the dimension of the completely flat portion of the indenter (indicated by the double-headed arrow in Figure 15) is 10 inches. The mesh was locally refined to capture the rounded corners.

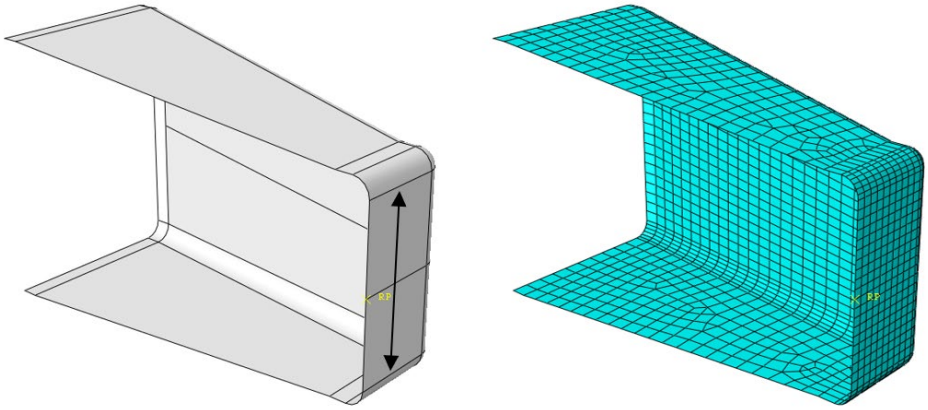

Figure 15. Indenter Part and Mesh

The team conducted the crash simulations in two steps, the initial velocity step and the crash step. The initial velocity step comprised a very short step, typically 1 ms, in which the indenter was assigned an initial velocity in the direction of travel (i.e., Z-direction), with movement in all other degrees of freedom fixed. In the crash step (typical duration 300 ms), the velocity boundary condition was released but movement in all other degrees of freedom remained fixed. The indenter was offset from the jacket by a small amount (approximately 0.6 inches) to ensure that it did not contact the jacket during the initial step (i.e., the indenter would travel 0.266 inches over the course of the 1 ms-long step for an assigned velocity of 15.16 mph). This arrangement is shown in Figure 16.

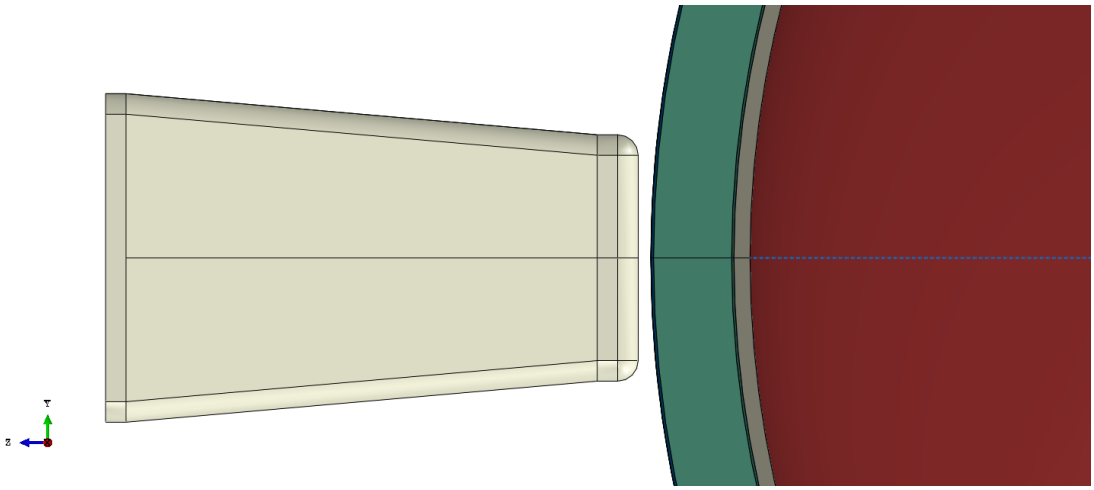

Figure 16. Cross-section Through Tank Car FE Model Showing Indenter ~0.6 inch Away

2.3.3 Foam Insulation

A 4-inch-thick layer of foam insulation is present between the tank shell and outer jacket (see Figure 17).

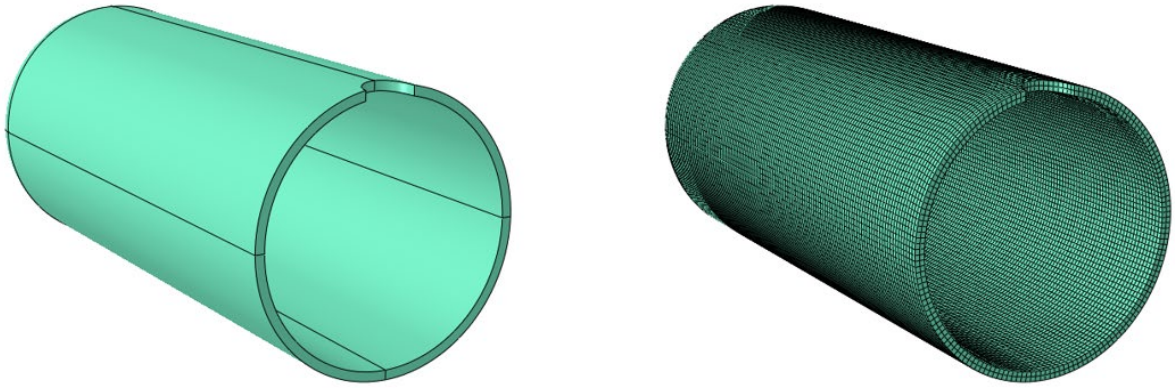

Figure 17. Overview of Foam Insulation (with and without mesh shown)

The foam part was modelled using solid (C3D8R) elements with a characteristic element length of 2 inches. This resulted in a total of 44,116 elements. A simple elastic-plastic material model was used based on that developed by Carolan et al [30], with the plastic response shown in Figure 18. The basic mechanical properties are shown in Table 3. A plastic strain-to-failure of 0.55 independent of stress triaxiality was implemented. Failure would therefore initiate at a plastic strain of 0.55, with a damage progression energy of 1.0 in-lbf/in^2 used to define subsequent element degradation to deletion phase.

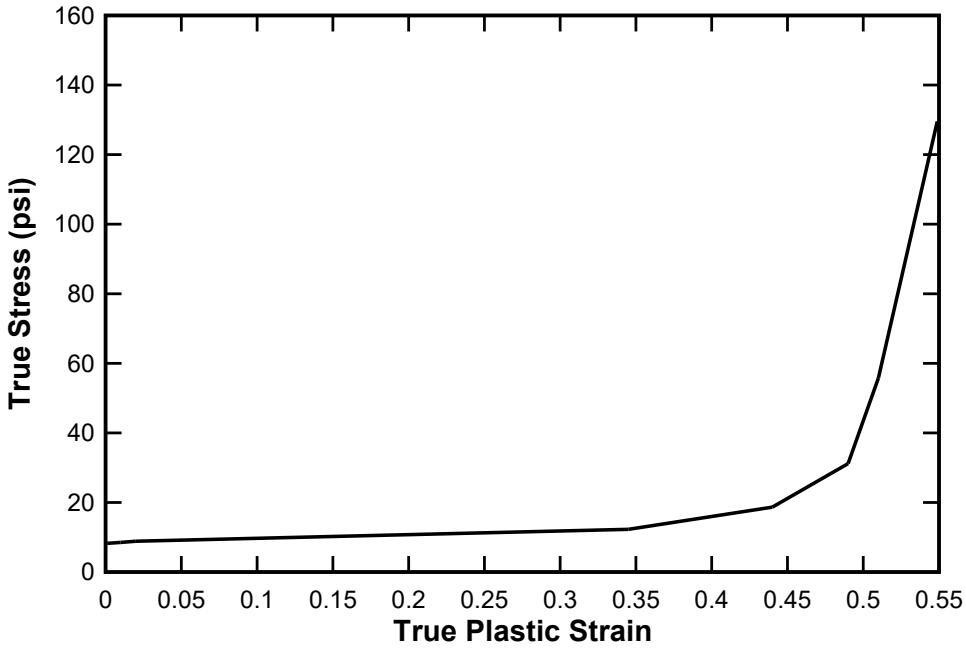

Figure 18. True Plastic Stress Strain Input Data for Foam Insulation [30]

Table 3. Mechanical Properties of Foam Insulation [30]

Parameter	Value	Units
Density	2.0	lbf/ft^3
Density	3×10^{-6}	$lbf*s^2/inch$
Modulus of Elasticity	941.5	psi
Collapse Stress	8.2	psi
Plastic Strain-to-Failure	0.55	-
Damage Progression Energy	1.0	$in\text{-}lbf/in^2$

2.3.4 Air and Water Phases

The air and water phases were modeled using a fluid cavity approach, in which a pneumatic cavity was defined for the pressurized air phase and a hydraulic cavity for the water phase. This is a simplified approach based on a calculation of average cavity pressure, but it showed satisfactory results while being much more computationally efficient than equivalent methods such as smooth particle hydrodynamics (SPH).

To define the respective cavities, a single part comprising a series of connected surfaces and referred to as the 'Membrane' was developed, as shown in Figure 19. The outer surface was offset from the tank shell mid-plane by half the shell thickness. A horizontal plane located 16.5 inches below the 12 o'clock position of the part was used to separate the water and air cavities and was positioned to give an outage of 10.6 percent.

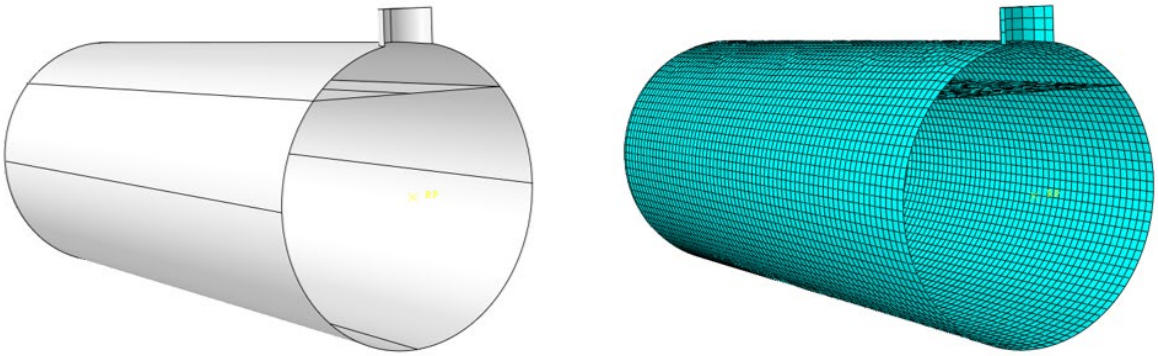

Figure 19. Membrane Part (with and without mesh)

The part was modelled using Membrane elements (M3D8R) with the characteristic element length of 3.5 inches. Membrane elements are those that can carry membrane forces but do not have any bending or transverse shear stiffness. As per the methodology described in [30], material properties were assigned to the membrane part that would minimize the stiffness introduced by the part while maximizing the efficiency. To ensure a reasonable stable time increment, the density of the membrane material model was set to that of steel; to minimize the stiffness increase, the modulus of elasticity was set to 0.1 percent of steel (shown in Table 4). The membrane thickness was set to 0.05 inches (i.e., thin).

Table 4. Material Properties of Membrane Material

Parameter	Value	Units
Density	7.35×10^{-4}	$lbf*s^2/in$
Modulus of Elasticity	30,000	psi

2.3.4.1 Hydraulic Cavity – Water

The water lading was modelled as a hydraulic cavity with the properties shown in Table 5. While the density of water was included, this was primarily for the purpose of calculating the bulk modulus. The bulk modulus of a liquid is related to its compressibility and defined as the pressure required to cause a unit change of volume of a liquid. Most liquids are practically incompressible, and therefore require very large pressures to cause any significant change in volume.

Since the membrane part was effectively modeled as a thin sheet (i.e., 0.05-inch-thick) with relatively little mass (1482.6 lbf), additional non-structural mass was assigned to the water boundary as shown in Figure 20 to account for the overall mass of water lading and associated inertial effects.

Table 5. Water Properties Used in FE Model

Parameter	Value	Units
Density	7.35×10^{-4}	$lbf*s^2/in$
Bulk Modulus	309,500	lbf/in^2
Part Mass	1482.6	lbf
Nonstructural Mass (Additional weight of water)	65,162.5	lbf
Temperature	55	˚F

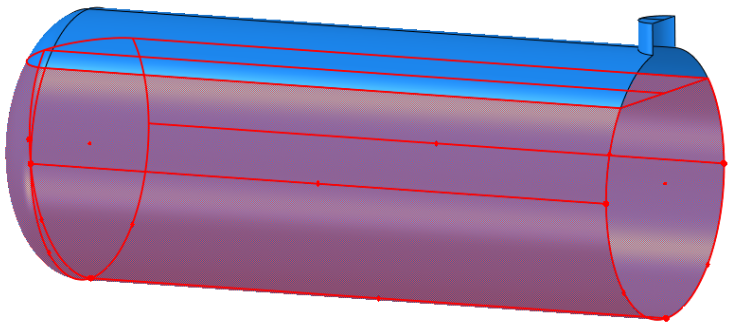

Figure 20. Water Boundary (red)

2.3.4.2 Pneumatic Cavity – Air

The gas phase of the lading was modelled as air at an initial gauge pressure of 100 psi. The average air pressure within the cavity would respond to changes in volume due to deformation of the tank and because the water lading would respond as a largely incompressible fluid. The inputs required to define the pneumatic cavity were obtained from [30], and are summarized in Table 37 and Table 38 of Appendix A.

2.3.5 Jacket

The 0.1196-inch-thick outer jacket was modelled using conventional shell elements with a characteristic global element length of 2 inches and the mesh refined locally in the region of impact (Figure 21 and Figure 22). The jacket was modelled using material properties for A1011 steel (summarized Table 6). The material model featured a Bai-Wierzbicki (B-W) failure envelope, further detail of which is provided in Appendix A. The B-W envelope defines the stress triaxially dependent plastic strain at which element failure initiates. A damage progression energy was used to define the subsequent damage evolution phase (i.e., the degradation to complete failure) and the resulting element deletion.

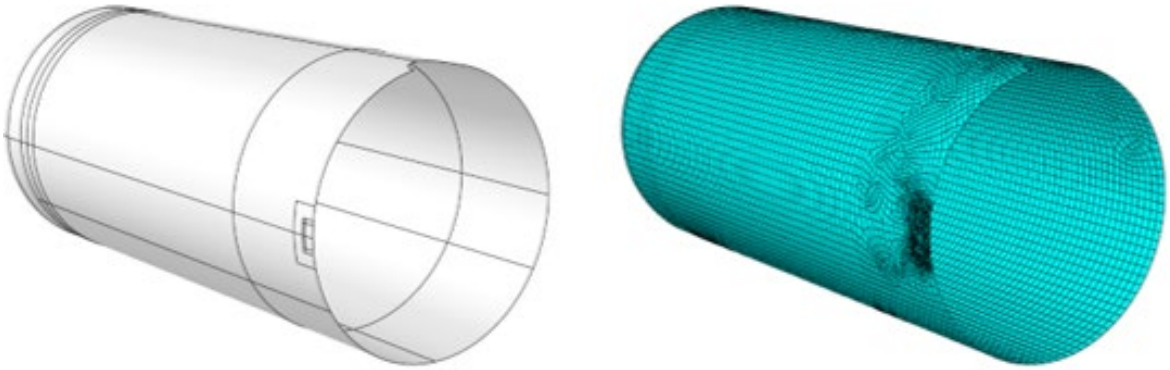

Figure 21. Jacket (with and without mesh)

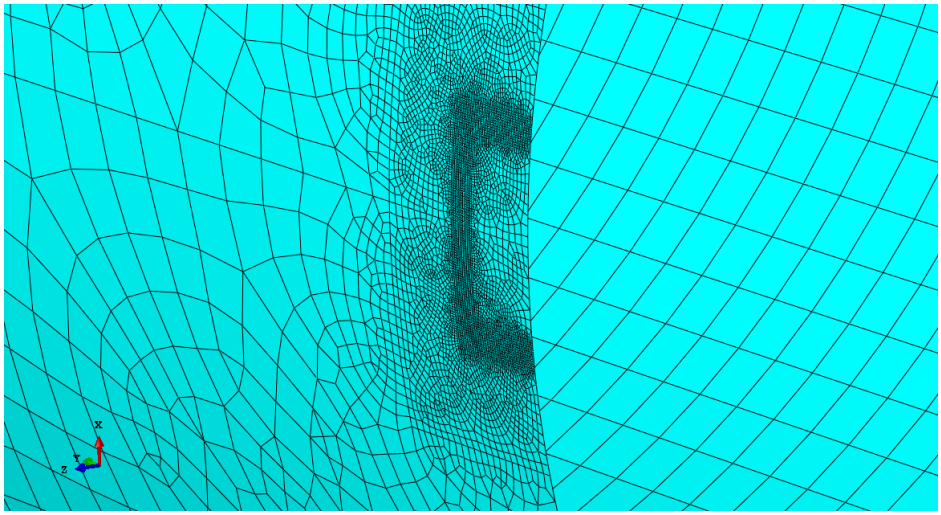

Figure 22. Locally Refined Mesh in Jacket at Impact Location

Table 6. Jacket A1011 Material Properties Used in FE Model

Parameter	Value	Units
Modulus of Elasticity	3 x 10^7	psi
Plasticity	Nonlinear - See Appendix A	Nonlinear - See Appendix A
Poisson's Ratio	0.3	-
Mass Density	7.35 x 10^{-4}	lbf*s^2/in
Damage Initiation	B-W Envelope – See Appendix A	B-W Envelope – Appendix A
Damage Progression	Linear, 1,500	in-lbf/in^2

2.3.6 TC128-B Tank Shell

The tank shell was modelled as two separate parts – a shell element part and a solid element part – connected at the interface using tie constraints. As shown in Figure 23, the shell element part comprised the 0.775-inch-thick cylindrical body, the 0.8125-inch-thick head, and the 1-inch-thick manhole extrusion as a single continuous part. At the impact location, a section of the shell was omitted to accommodate a solid element representation. The shell element part was developed using reduced integration shell elements (S3R and S4R) with a global characteristic element length of 2 inches. Locally, where the shell part was tied to the solid part, the mesh was refined to ensure reasonable enforcement of tie constraints. The solid region was meshed with a very fine mesh (0.085 inches), resulting in 9 elements through the thickness and 652,608 elements within the ~15 by 35-inch region. See Figure 24, Figure 25 and Figure 26.

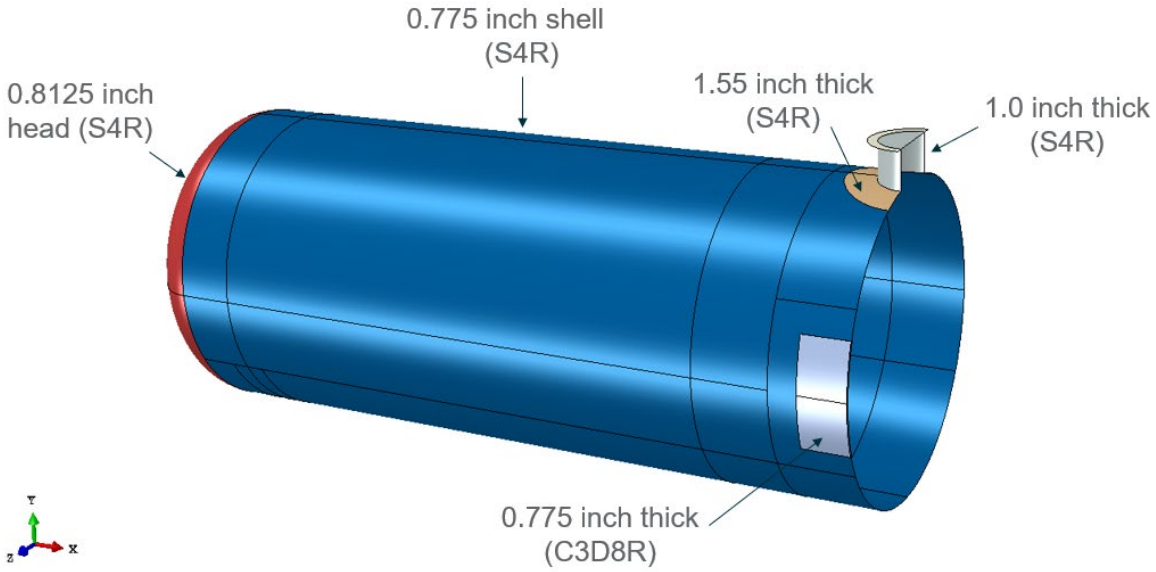

Figure 23. Overview of Tank Shell in FE Model

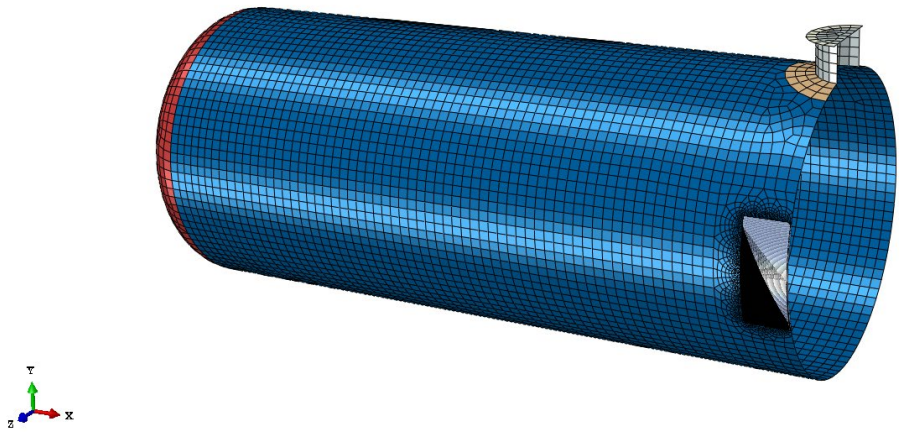

Figure 24. Overview of Tank Shell in FE model with Mesh Shown

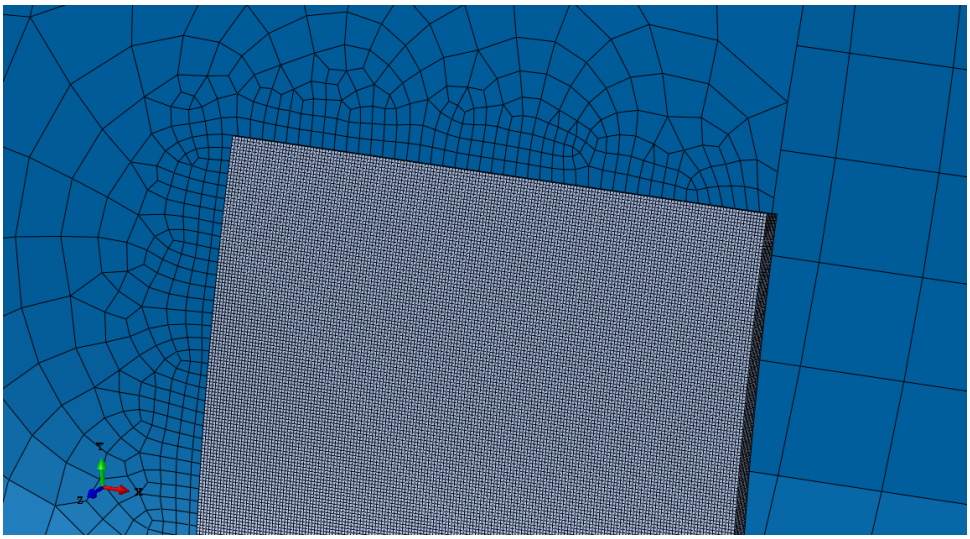

Figure 25. Image Showing Solid Region Mesh and Local Refinement of Shell Mesh at the Shell-to-solid Interface

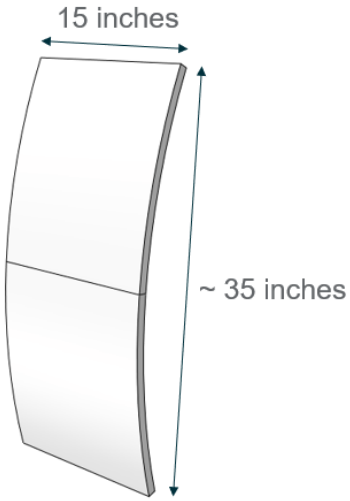

Figure 26. Image Showing Extent of Solid Region

The team developed two separate material models for the tank shell, one for the shell element region and one for the solid element region. The key difference was that the solid region material model featured a B-W failure envelope developed by Carolan following tensile testing of samples extracted from the tank shell [30], hence the 'Actual' term. This is discussed further below, with additional information found in Appendix B.

The baseline properties applicable to both material models are summarized in Table 7, with the hardening curve used to define plasticity behavior shown in Figure 27.

Table 7. TC128-B Baseline Material Properties Used in FE Model

Parameter	Value	Units
Modulus of Elasticity	3×10^7	psi
Plasticity	Nonlinear – See Figure 27 & Appendix B	-
Poisson's Ratio	0.3	-
Mass Density	7.35×10^{-4}	$lbf*s^2/in$

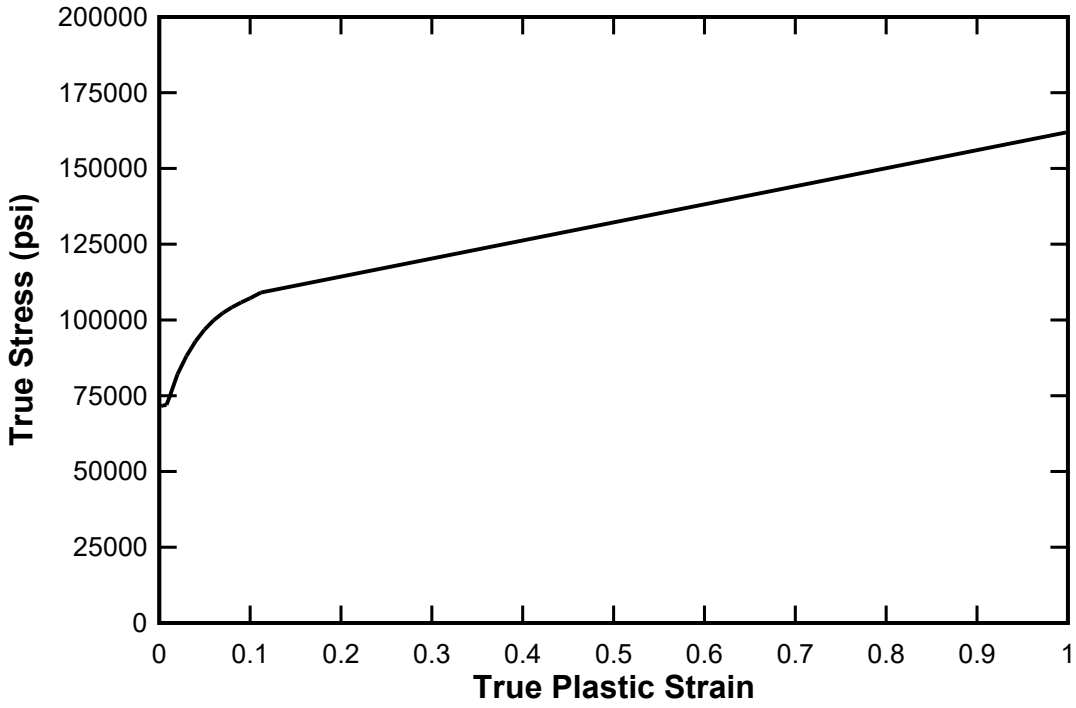

Figure 27. True Plastic Stress-Strain Input Data for 'Actual' TC128-B steel [30]

The B-W envelope used for the solid region material model is shown in Figure 28. It defines the plastic strain at which failure initiates for different stress triaxialities.

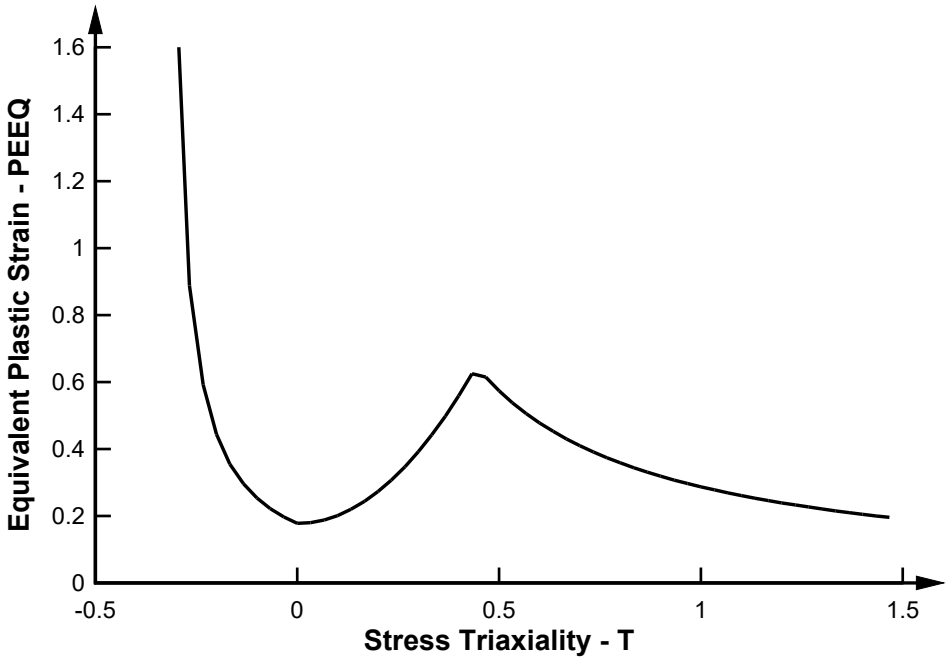

Figure 28. B-W Damage Model for 'Actual' TC128-B

The B-W curve and damage progression parameters are calibrated for a specific element type and size. There is a maximum element size that can be reasonably used in the round bar tensile tests to develop the damage model and this element size must be carried through to the full-scale model, hence the very fine mesh in the solid element region of the full-scale model. The accuracy of this region of the model is critical to capturing the correct behavior of the impact and defining when puncture occurs.

2.3.6.1 Mass Scaling

The element size also dictates the speed at which analyses can be performed in an explicit analysis, where a small element results in a low stable time increment and therefore long simulation time. This can and has been alleviated to an extent using mass scaling. Mass scaling works by increasing the mass of the smallest elements, which slows the wave propagation speed across the element and therefore increases the stable increment. A typical target stable time increment of 5E-07 s was set, resulting in the mass of the elements within the solid region being scaled by a factor of 4.35. The overall increase in mass of the model through mass scaling was low (~0.15 percent) and was observed to have no significant effect on the response of the model.

2.3.7 Skid Beam

The skid beam was modelled as a discrete rigid part, measuring 180 x 22 x 12 inches, and assigned a weight of 3,502 lbf. It was connected directly to the tank shell using a multi-point constraint (MPC) whereby the nodes across an area measuring 12-inches-wide and covering an arc 120 degrees across the bottom of the shell were rigidly connected to a discrete point on the skid beam, as shown in Figure 29. Boundary conditions were assigned to the skid to prevent movement in the vertical Y direction and rotation about the X-axis.

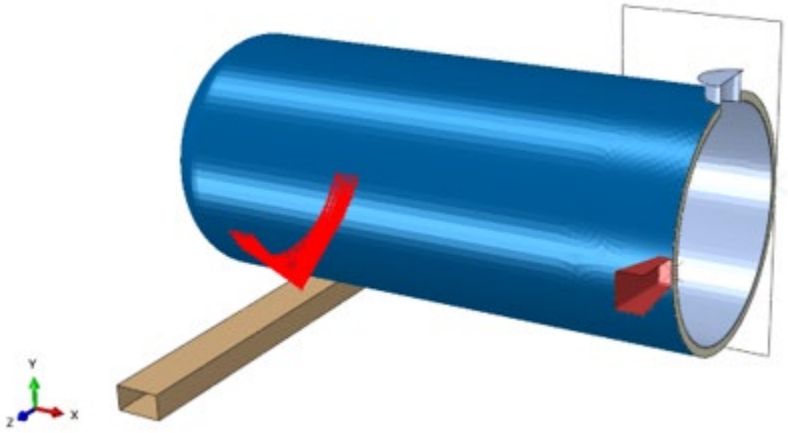

Figure 29. Image Showing MPC Connecting Skid Beam to Tank Shell

2.3.8 Friction

The team used the General Contact algorithm within Abaqus with 'Hard Contact' assigned in the normal direction and a coefficient of friction 0.3 assigned in the tangential direction. This contact relationship was applicable between all parts. The hard contact label defines the pressure-overclosure relationship, which minimizes penetration of one surface into another.

2.3.9 String Potentiometers

The physical test was instrumented with 10 string potentiometers, 9 recording translations in the horizontal plane (Z-plane in Figure 29) and 1 located at the center of the tank recording vertical deformation of the tank shell. Figure 30, from [30], shows an overview of the arrangement of the string potentiometers. In the Abaqus model these were implemented using connector elements, as shown in Figure 31. Specifically, four connectors were used to capture displacements at the center of the tank, three in the horizontal plane and one in the vertical. The displacements of the skid and tank end were recorded simply as history output.

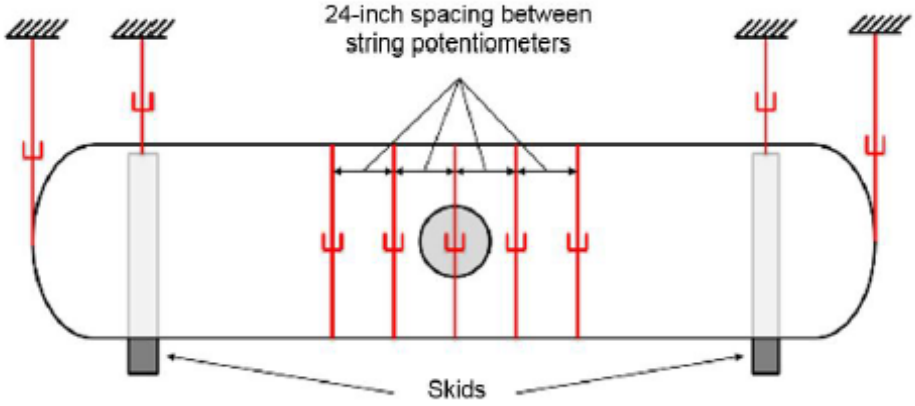

Figure 30. Tank car String Potentiometers (plan view) [30]

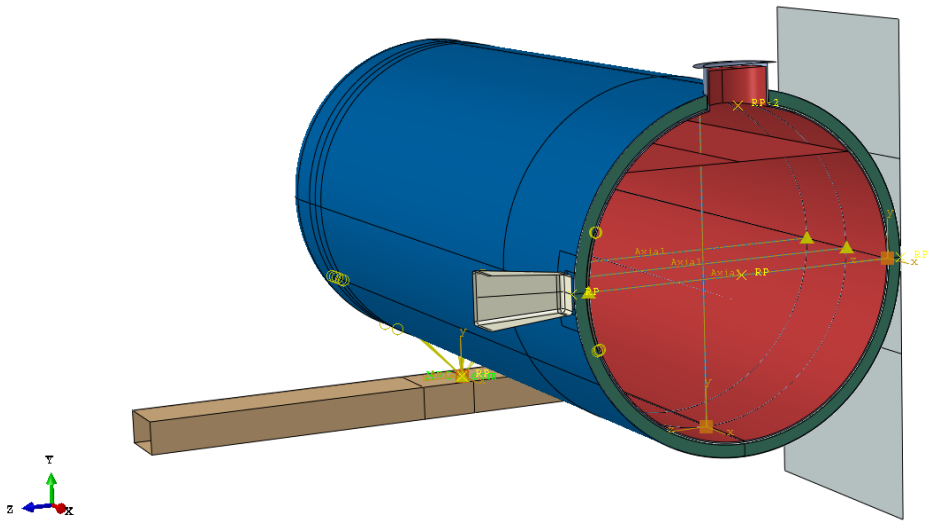

Figure 31. Image showing Arrangement of String Potentiometers in FE Model

2.3.10 Results – Test 6

An overview of the response of the FE model when the simulation was run at the test speed of 15.16 mph is shown in Figure 32. Between 0 to 50 ms the impactor penetrates the outer jacket, crushes the foam at the impact location, and begins to locally deform the tank shell. The tank then begins to displace backwards, impacting the wall and crushing the foam on the rear side, as shown at time 150 ms in Figure 32. Once the foam is crushed and the tank shell is essentially bearing directly onto the rigid wall, the indenter force increases, causing greater local deformation and eventual failure of the tank shell locally behind the indenter.

An overview of the local puncture behavior in the solid element region of the tank shell is shown in Figure 33. It shows that a section of material just larger than the indenter face fails and is pushed through into the tank. In the physical test a slightly different behavior was observed, with a relatively large section of the tank shell ejected outward after the impact. The ram car (i.e., indenter) also rebounded following impact, suggesting that failure and ejection of the section of tank car shell may have occurred due to internal pressure build-up (i.e., the impact fractured the shell, but gross failure occurred during rebound, when the weakened section of tank was forced out by the water pressure). While the FE model did not capture this exact and quite complex behavior it did correlate very well against the physical test across a range of measured parameters.

Figure 34 and Figure 35 compare the displacement and speed of the indenter obtained from the FE model with that recorded from Test 6. Both plots show very close agreement up to the point at which failure initiates in the tank shell, which occurs around 220 ms into the event. Figure 36 compares the force-displacement response, which also shows good agreement. Peak force in the FE model was predicted to occur at a displacement of 37.4 inches, versus 38.0 inches recorded from the test, a difference of 1.6 percent. The peak force in the FE model was calculated to be approximately 14.6 percent lower than that recorded during the test, however the total energy absorbed, which is the integral of the force-displacement curve, was calculated to be very similar at 2.16 versus 2.27 million foot-pounds for the FE model and Test 6 respectively (a difference of 4.8 percent). The average air pressure in the outage showed an approximate 8 percent difference between measured and predicted values (Figure 37). The displacements measured in the string

potentiometers also showed good general agreement, as summarized in Table 8. Comparative plots for the string potentiometers can be found in Appendix C.

Overall, good agreement was obtained between the FE model and the physical test.

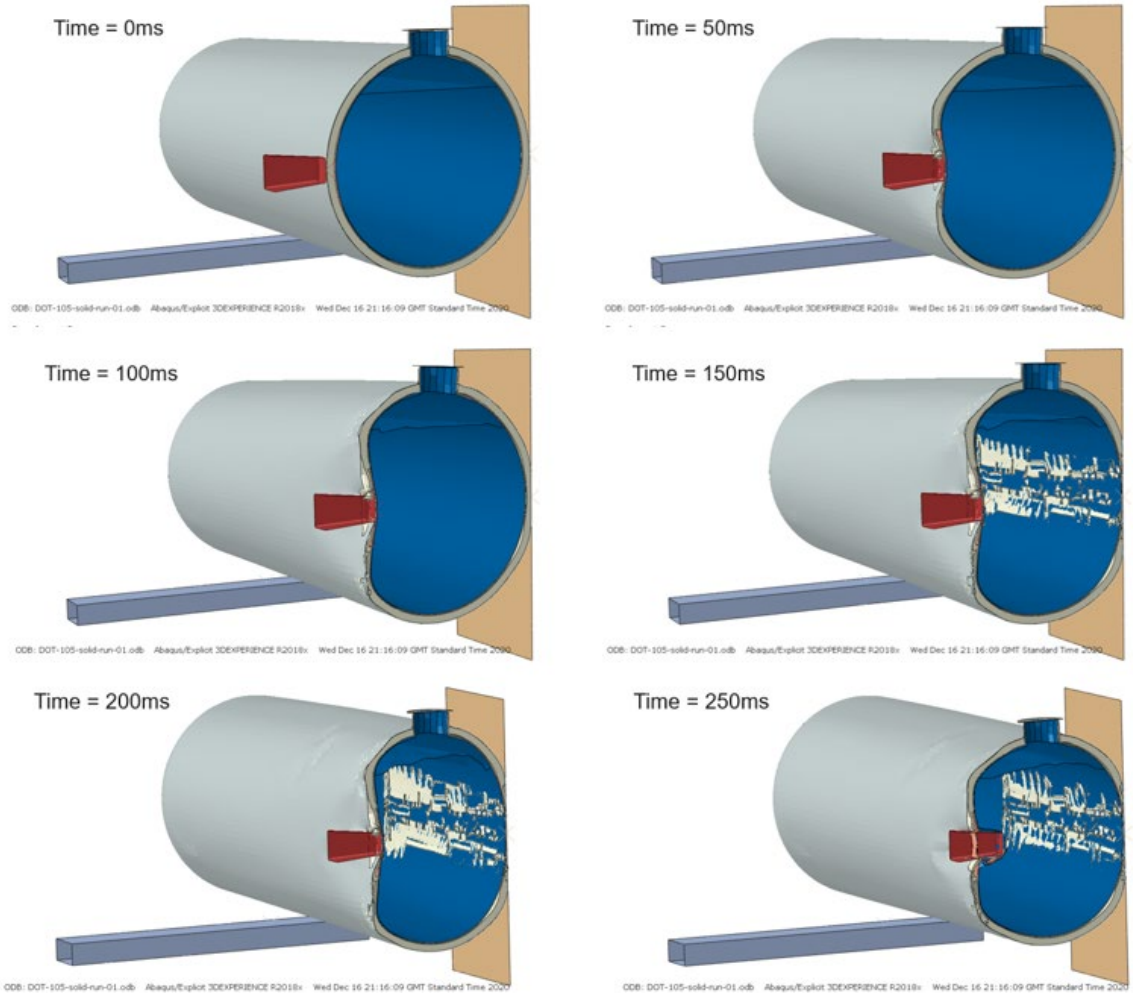

Figure 32. Overview of Test 6 Simulation

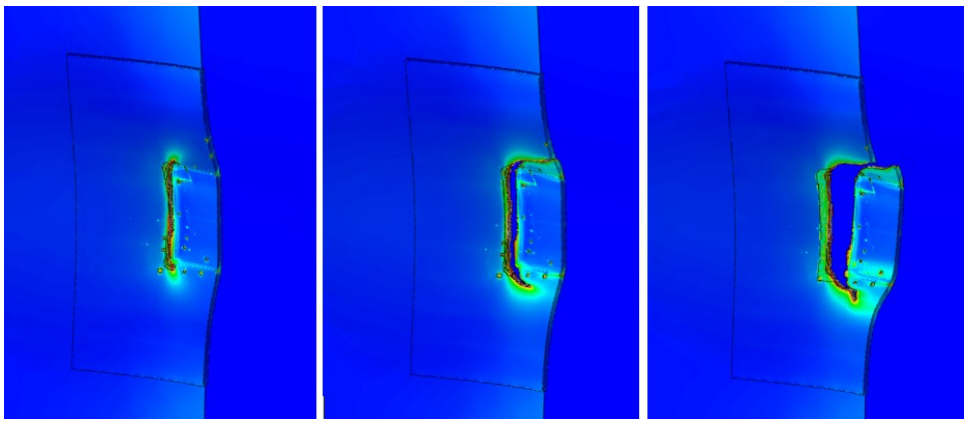

Figure 33. Local Puncture in Solid Region of Tank Car Shell

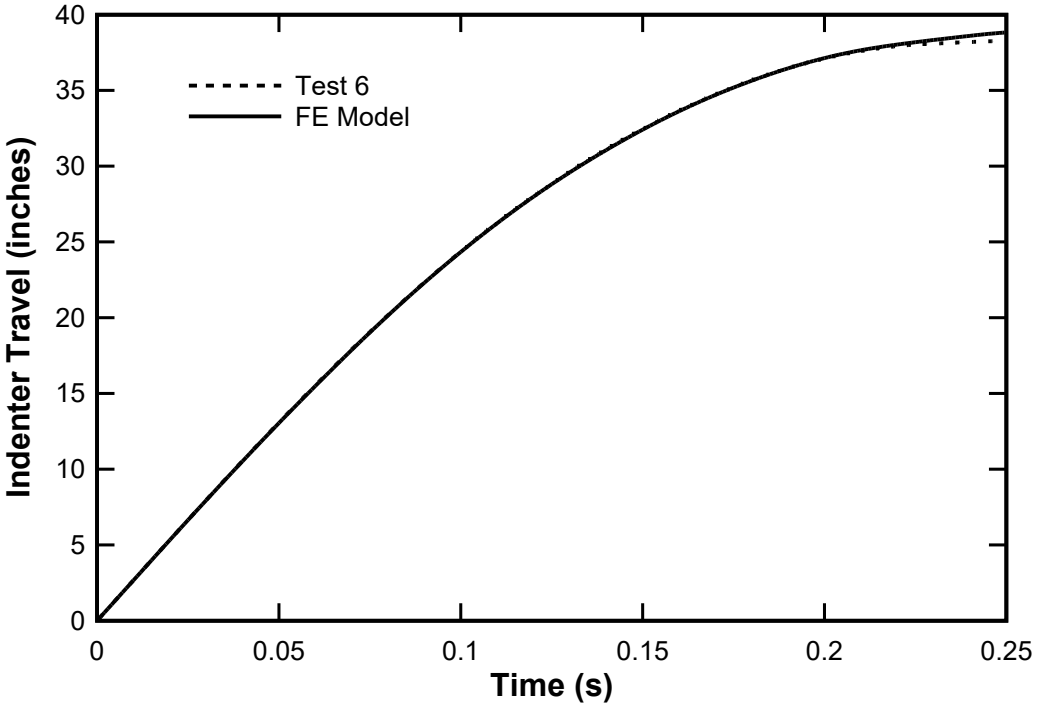

Figure 34. Indenter Travel vs Time, FE Model vs Test 6

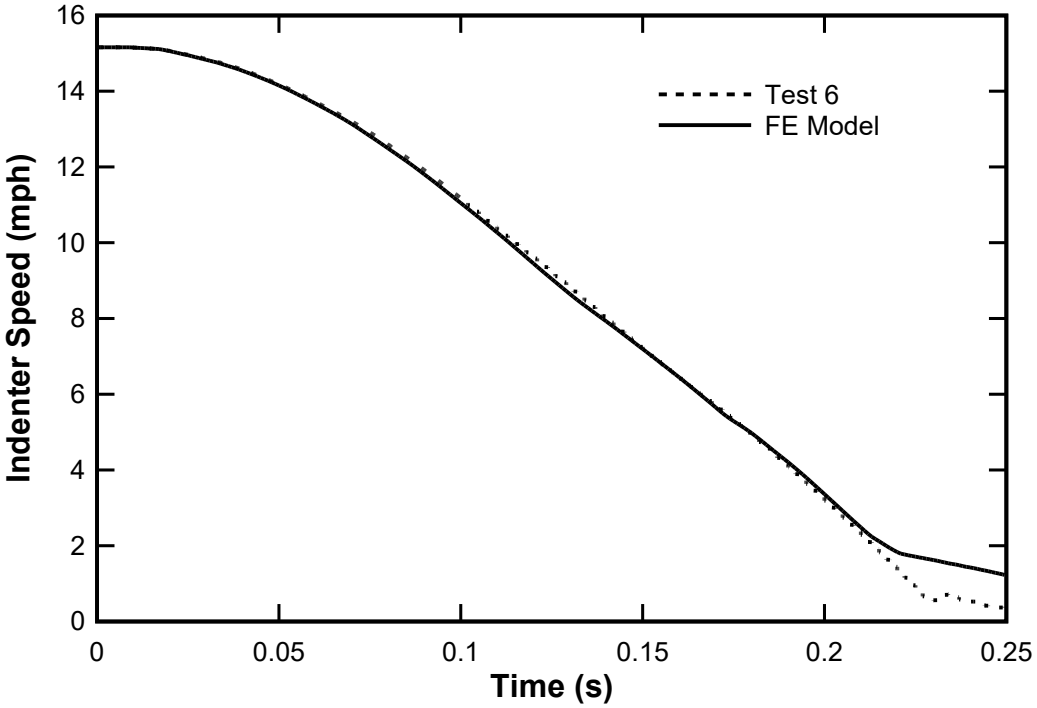

Figure 35. Indenter Speed vs Time, FE Model vs Test 6

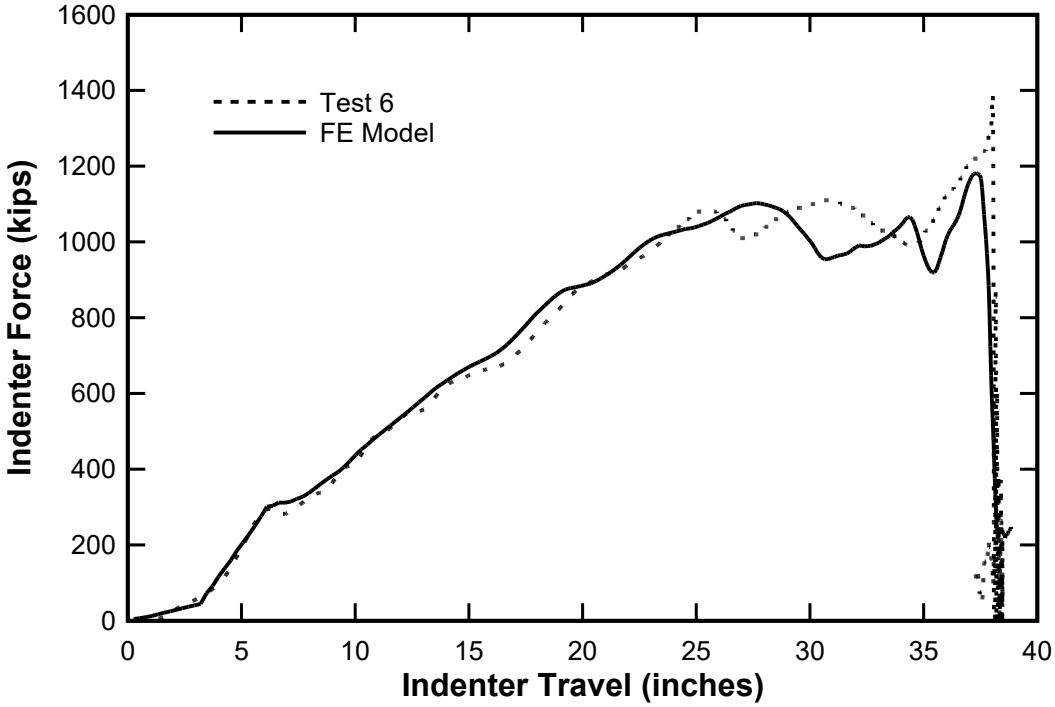

Figure 36. Indenter Force vs Displacement, FE Model vs Test 6

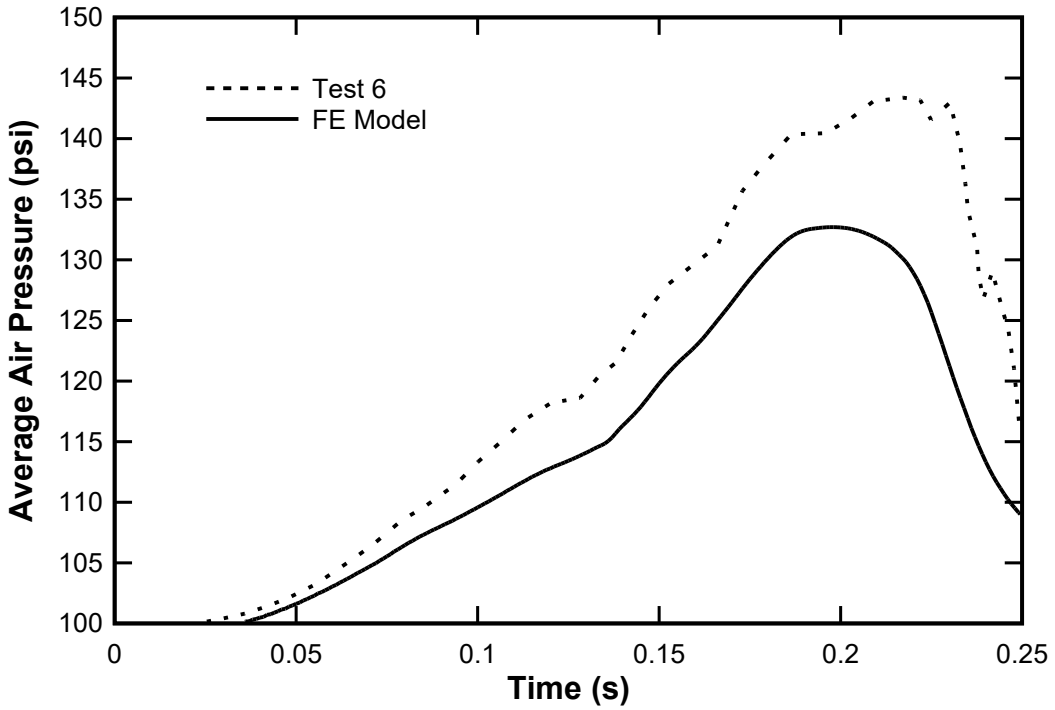

Figure 37. Average Air Pressure vs Time, FE Model vs Test 6

Table 8. String Potentiometers, FE Model vs Test 6

Location	FE Model* Peak Displacement (in)	Test 6 Peak Displacement (in)	% Difference
Center	30.6	30.6	0.0
24-in offset	23.2	24.5	5.3
24-in offset	23.2	23.6	1.7
48-in offset	17.5	15.8	-10.8
48-in offset	17.5	18.2	3.8
Vertical	11.3	17.2	34.3
Skid	11.8	10.4	-13.5
Skid	11.8	9.9	-19.2
Head	11.5	10.3	-11.7
Head	11.5	9.8	-17.3

*Half-symmetry FE model, therefore only one value obtained for certain locations

2.3.11 Puncture Speed

Having validated the response of the full-scale model, the team conducted additional simulations at 13.0 and 14.0 mph to calculate the survival speed of the tank car when subjected to side-impact with a 12 x 12-inch indenter. The results, summarized in Table 9, showed that the tank car survived the 13-mph case but failed at 14 mph.

Table 9. Test 6 – Puncture Speed

Speed (mph)	Initial Kinetic Energy (m-ft-lb)	Result	Notes
15.16	2.283	Fail	Test 6 case
14.00	1.947	Fail	Tank shell fails during rebound phase
13.00	1.679	Pass	Survival speed

The force-displacement response for each case is shown in Figure 38. The peak force is similar in each case at approximately 1300 kips. The curves show that in the 13- and 14-mph cases the indenter rebounds after reaching peak force, whereas in the 15.16-mph case it continues to travel forward. In subsequent simulations where the effectiveness of different mitigation solutions have been considered, the results are compared to these baseline simulations, where 13 mph is the calculated survival speed.

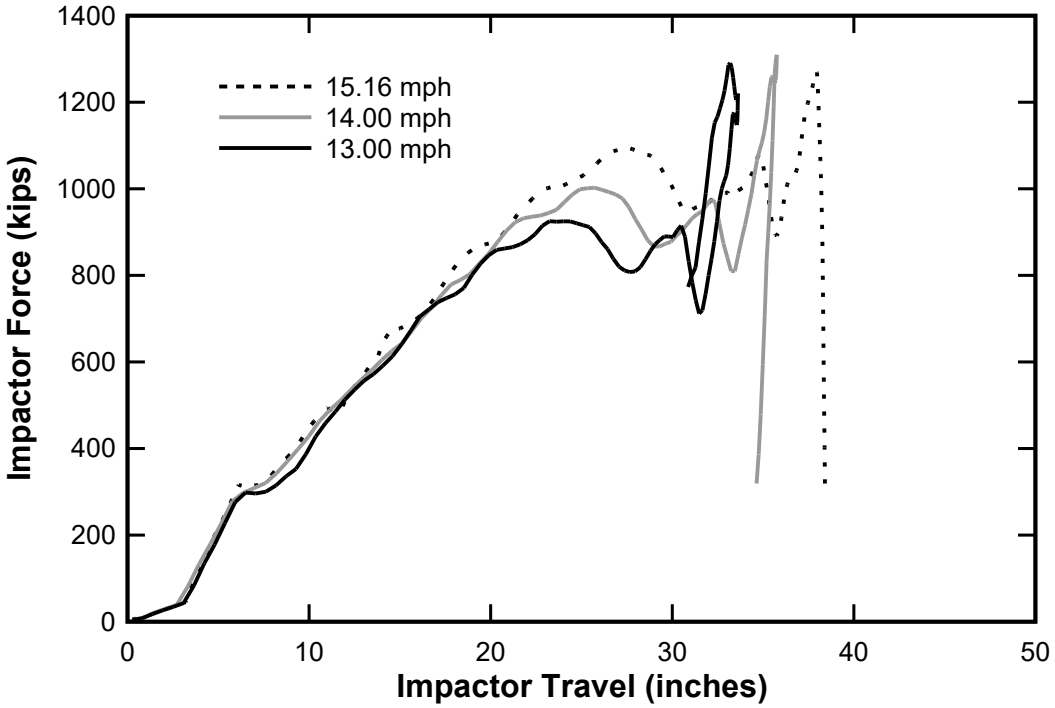

Figure 38. Indenter Force vs Displacement, FE Model: 13.0, 14.0, and 15.16 mph

3. Sub-Model

The overall objective of the research effort was to investigate various tank car mitigation options using numerical simulation. While the validated full-scale model discussed in the previous section could be used to assess the effectiveness of different solutions, it could not be used to rapidly assess different mitigation options due to its size and complexity. For example, the full-scale model took approximately 77 hours to complete the Test 6 simulation using a conventional desktop analysis machine running on 12 processors. This was reduced to less than 24 hours when using a high-powered cluster using 23 processors. However, while a 24-hour turnaround was potentially workable, the output files were large, and the model would only increase in complexity when different mitigations were considered. Therefore, the research team sought to develop more efficient sub-models.

Ultimately, the team developed a scaled-down, defeatured version of the full-scale model and used it for most of the mitigation simulations. More simplified sub-models were also developed and used in some cases to investigate specific local behavior. These models are described in detail in the relevant sections of the report. The focus of this section of the report however is on describing the development of the 'baseline' quarter-symmetry sub-model.

3.1 Quarter Symmetry Model

The objective of using the sub-model was to capture most of the key behaviors exhibited by the full-scale model while increasing its efficiency. The key features known to influence the response include the shape of the tank, the incompressibility of the liquid phase and the compressibility of the gas phase, the inertia of the fluid, the inertia of the tank structure, the response of the jacket, and crushing of the foam. Crucially, the sub-model should also be capable of reliably predicting failure of the tank shell. The full-scale model captures these features with varying degrees of sophistication, so the team developed and investigated a simplified version of that model.

The half-symmetry full-scale model was reduced to a quarter-symmetry model as shown in Figure 39. The skid and manhole features were removed and the horizontal plane separating the water and air phases was repositioned to give an outage of 10.6 percent. This required that the outage at the top of the model be decreased (the horizontal plane moved up approximately 6.0 inches), as the use of quarter-symmetry would give rise to an equivalent outage at the bottom of the tank. The non-structural mass assigned to represent the water lading was halved, as was the mass of the indenter. The final change was made to the TC128-B solid element puncture region, with the full-integration incompatible mode brick elements (C3D8I) replaced by the more computationally efficient reduced-integration elements (C3D8R). The transition to C3D8R elements was first verified by repeating the round bar tensile test. The model otherwise remained the same.

To verify the response of the model, two simulations were undertaken:

- Test 6: 12 x 12-inch impactor at 15.16 mph
- Test 8: 6 x 6-inch impactor at 9.7 mph [33]

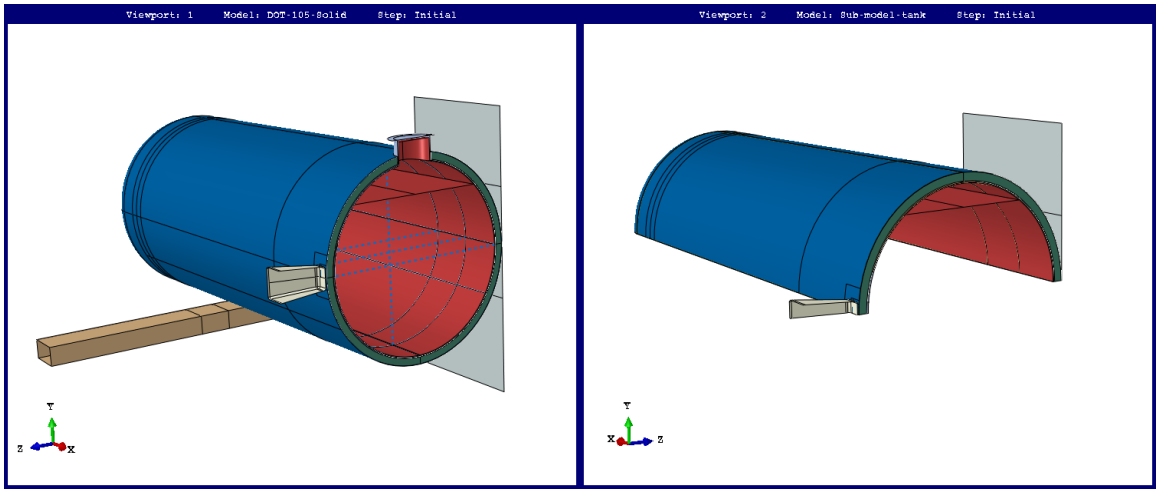

Figure 39. Full-Scale Model (left) and Quarter-Symmetry Model (right)

3.2 Test 6 Response

The results obtained from the quarter-symmetry model for Test 6 were very similar to those produced by the full-scale model and showed good agreement with the physical test. Figure 40 shows a comparison of the force-displacement response of the quarter-symmetry model with the physical test. The displacement at failure was a close match (~38 inches) while the peak force obtained from the quarter-symmetry model (1432 kips) was closer to the Test 6 force (1391 kips) than the full-scale model (1188 kips), a difference of ~3 percent versus ~14.6 percent. The increase in peak force is largely attributed to the shift from C3D8I to C3D8R elements within the puncture zone.

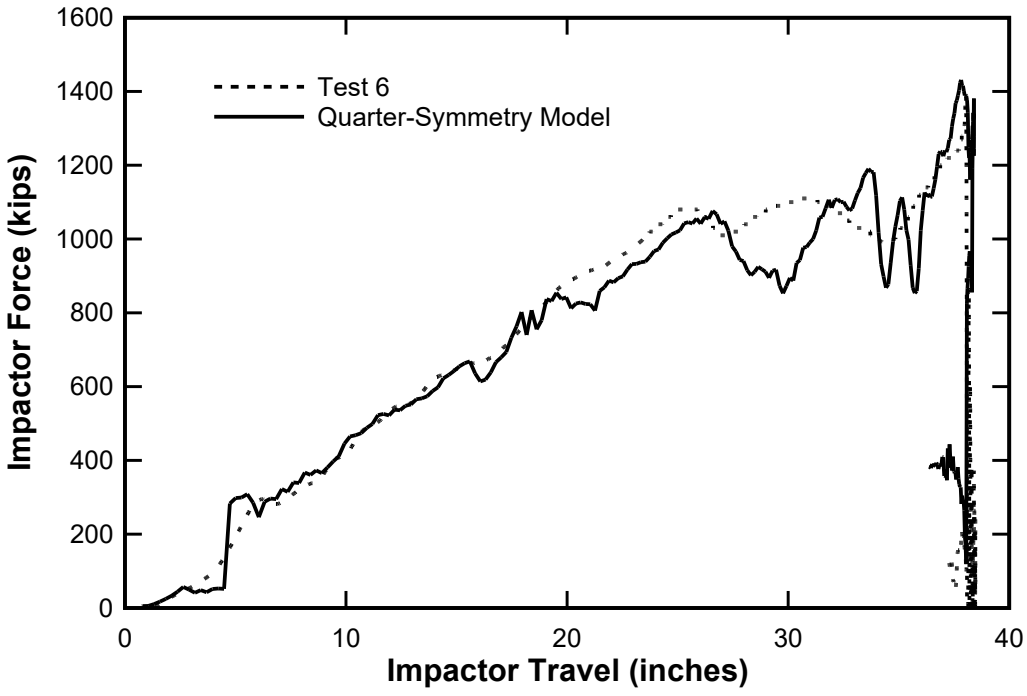

Figure 40. Indenter Force vs Travel, FE Quarter-Symmetry Model vs Test 6

Figure 41 shows the average cavity air pressure calculated using the quarter-symmetry model compared to the Test 6 data. The FE results are like those obtained using the full-scale model and are approximately 8 percent below the Test 6 recorded pressure at the peak.

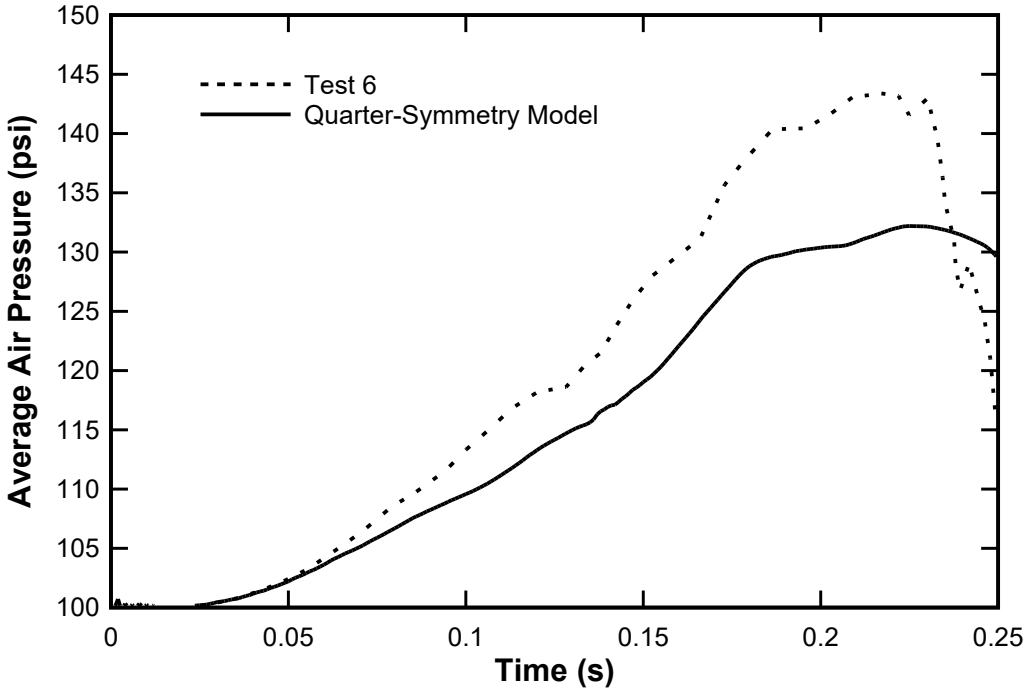

Figure 41. Average Cavity Pressure vs Time, FE Quarter-Symmetry Model vs Test 6

An overview of the deformed shape of the model following puncture is shown in Figure 42. Note that a 'mirror plane' has been used to illustrate the model as if it were half-symmetric.

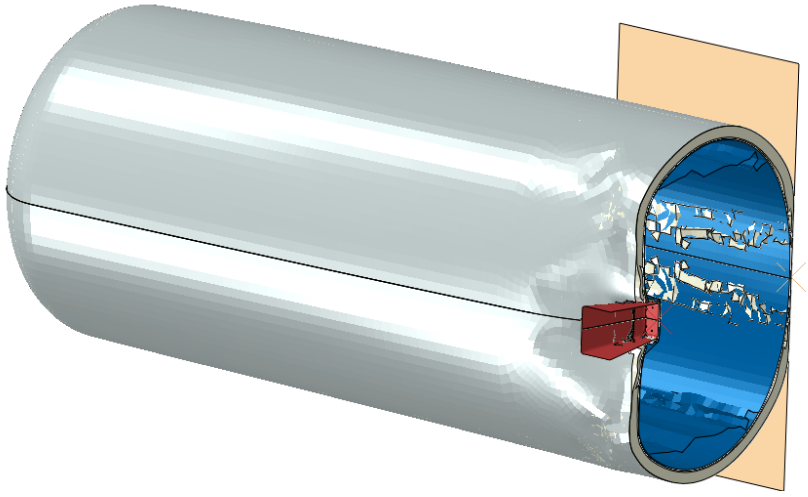

Figure 42. Overview of Quarter-Symmetry Model Following Puncture (time = 250 ms)

In summary, across various key metrics the quarter-symmetry model compared well against the physical test. Moreover, the simulation time was significantly reduced, with the Test 6 simulation shown here taking approximately 4.5 hours using 23 processors on a high-powered cluster.

3.3 Test 8 Response

Test 8 [33] was undertaken in 2018 using a 6 x 6-inch indenter at a speed of 9.7 mph, with the test setup otherwise intended to replicate Test 6. Test 8 was replicated with the objective of further assessing and validating the quarter-symmetry model. The 6 x 6-inch indenter was implemented, as shown in Figure 43, with the indenter mass changed to match one quarter of that used in the physical test. The indenter features a 1/2 inch radius such that the flat portion of the indenter face measures 5 x 5 inches.

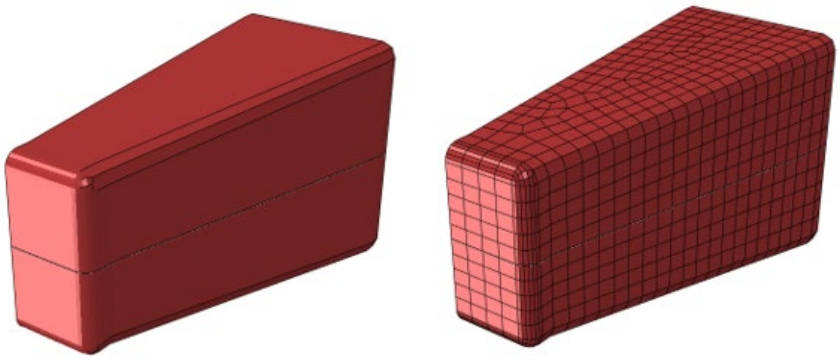

Figure 43. Overview of 6 by 6-inch Indenter

The resulting force-displacement curve obtained from the quarter-symmetry model is compared to the physical test results in Figure 44 with the curves showing good agreement. Figure 45 illustrates the response of the model just prior to failure and Table 10 compares some of the key parameters. The greatest difference is in the peak force, but as shown in Figure 44, this occurs for only a very short period in the physical test.

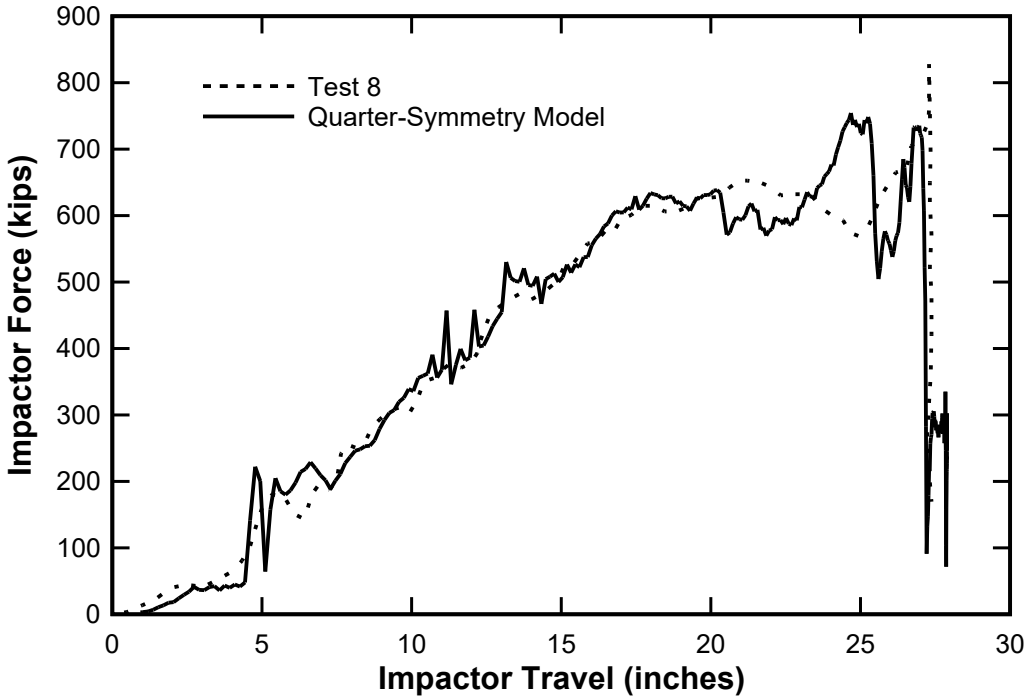

Figure 44. Indenter Force vs Travel, FE Quarter-Symmetry Model vs Test 8

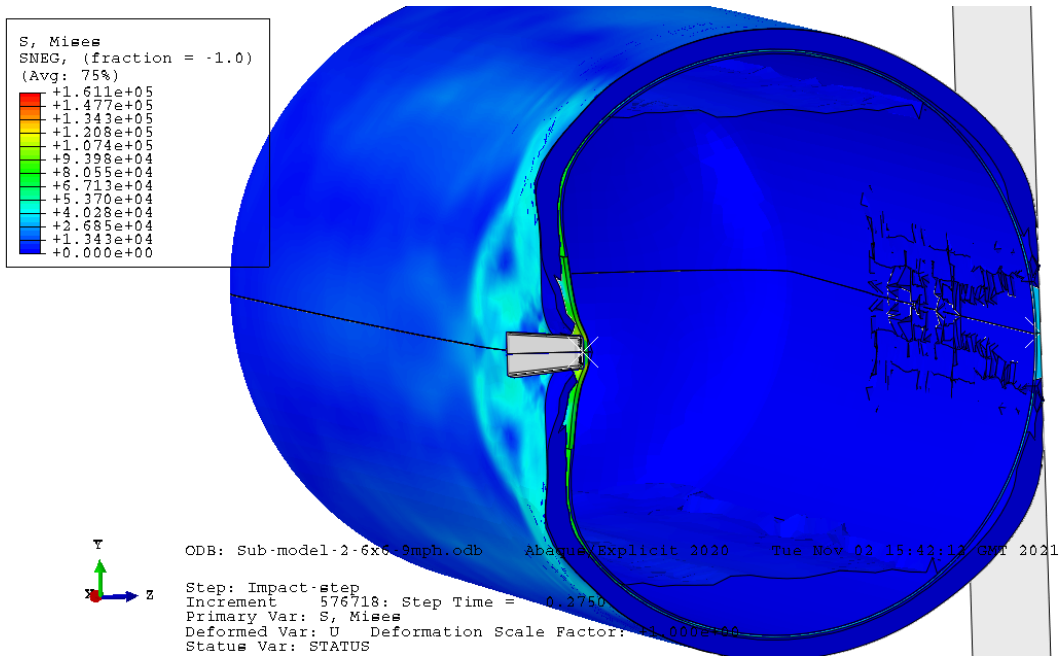

Figure 45. Overview of Test 8 Simulation (Quarter-Symmetry Model with Mirror Plane Used in X-Z Plane)

Table 10. Test 8 Comparison, FE Quarter-Symmetry Model vs Physical Test

Parameter	FE Model	Test 8	% Difference
Peak Force (kip)	754.4	842.7	11.7
Indenter displacement at failure (in)	27.1	27.9	3.0
Energy absorbed at peak force (ft-kip)	921.5	929.9	0.9
Peak Outage Pressure (psi)	108.0	112.9	4.3

In general, the quarter-symmetry model demonstrated good agreement with the physical test data for both Tests 6 and 8, and in some metrics, particularly the peak force and displacement to failure, the model showed slightly improved behavior when compared to the results obtained using a larger half-symmetry model while using a fraction of the computational cost of the half-symmetry model. This finding suggests that capturing the puncture behavior of the shell is one of the most important parameters in determining puncture resistance, with features such as the manhole and skid of secondary importance.

In conclusion, the quarter-symmetry model provided an efficient and reliable means to investigate different mitigation methods, and the team was confident that findings from its use would transfer to the overall behavior and puncture resistance of the tank.

4. Mitigation

This section discusses the various mitigation methods the team investigated as part of this research. Section 4.1 first outlines some of the key constraints affecting the implementation of potential mitigation solutions and Section 4.2 through Section 4.7 detail the different mitigation solutions considered.

4.1 Key Constraints

4.1.1 Clearance Envelope

The AAR Plate B Clearance Standards determine the maximum height, width, and truck center spacing for tank cars. As illustrated in Figure 46, the height from the top of rail is set to 15 ft-1 in, the width to 10 ft-8 in, and truck centers not to exceed 41 ft-3 in. Swingout at the center of a car on a 13-degree curve results in a maximum overall car length of 57 ft-2 in [34]. A baseline DOT-105 tank car has a steel shell outer diameter of 8 ft-6 3/10 in (102.3 in). This provides a lateral spacing from the outer surface of the shell to the maximum width of approximately 1 ft-7/8 in. This is essentially the minimum gap in which external mitigation measures could be implemented assuming the foam insulation (4-inch-thick) and jacket are either removed as part of the mitigation solution or implemented within it.

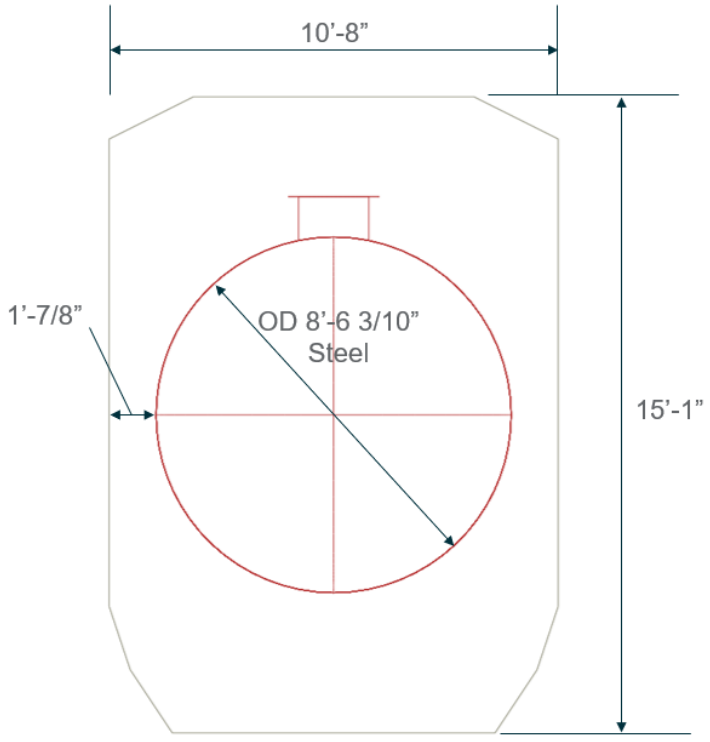

Figure 46. Schematic Cross-section Through DOT-105 Tank Car Within Outer Envelope

In terms of overall car length, the DOT-105 is a somewhat shorter car with truck centers in the region of 35 ft. The possibility therefore exists to decrease the diameter and increase the overall car length. This would provide more space around the tank in which to install mitigation solutions. For example, Tyrell [34] shows that reducing the tank car internal diameter to 7 ft-11

3/4 in can be accommodated within the overall length constraints. The new tank would be approximately 4 ft-4 in longer, but the lateral space available would increase by approximately 3 1/4 in. The lateral spacing available for different configurations of DOT-105 tank cars are summarized in Table 11. The table shows that the minimum lateral space available is ~8.79 inches (retrofit condition) increasing to a maximum of 16.125 inches (new reduced diameter tank). This is important, as more space provides greater opportunity for energy absorption.

Table 11. DOT-105 Potential Configurations and Space Available for Side Impact Mitigation

#	Type	Description	Outer Diameter (in)	Lateral Space Available (in)
1	Retro-fit	Install new mitigation on top of existing foam & jacket	110.42	8.79
2	Retro-fit	Replace foam & jacket with new mitigation	102.30	12.85
3	New – reduced diameter	Install new mitigation on top of existing foam & jacket	103.87	12.065
4	New – reduced diameter	Replace foam & jacket with new mitigation	95.75	16.125

4.1.2 CFR § 179.13 – Tank Car Capacity and Gross Weight Limitation

The maximum gross weight of a tank car is 286,000 lbf (129.7 te). The weight of a standard DOT-105 chlorine-filled tank car is 247,000 lbf (112.0 te), leaving approximately 39,000 lbf (17.7 te) available for new mitigation structure. This equates to approximately 29.4 lbf/ft^2 (~144 kg/m^2) based on the calculated surface area of the jacket (see Case #1 in Table 11). The allowable weight per area would clearly increase if the foam and jacket were removed or replaced as part of the new mitigation solution.

4.1.3 CFR § 179.18 – Thermal Protection Systems

Tank cars requiring thermal protection must have sufficient thermal resistance so there will be no release of any lading within the tank car, except through the pressure relief device, when subjected to:

(1) A pool fire for 100 minutes

(2) A torch fire for 30 minutes

For the DOT-105 specification, thermal protection is provided by way of the 4-inch-thick foam insulation, enclosed by the outer A1011 steel jacket.

4.2 Mitigation – Enhanced TC128-B

In the first mitigation solution the team considered the mechanical properties of tank car steel.

In 2008 the Southwest Research Institute (SwRI) undertook a study to investigate the properties of tank car steels retired from the fleet [35]. The study found that most samples tested (97 percent) met the current AAR TC128-B specification for elemental composition whereas 82 percent of the samples met the tensile property requirements. While tank car specifications allow

for several different grades of steel, most of the pressure car fleet are manufactured from TC128-B (>93 percent in 2006).

In response to a mandate by AAR to develop tougher steels to improve puncture resistance, ArcelorMittal (AM) undertook research and development of a new low-carbon tank car steel [36]. The new steel showed improved toughness properties in normalized and post weld heat treated condition while meeting the required tensile properties.

AM conducted a series of round and notched bar tensile tests to characterize the stress-strain relationship and develop a B-W fracture model for both the current steel and new steel. A FE model of a tank car was developed and subjected to side-impact loading by a spherical object. The material in the puncture zone was modelled using both current and new steel, with AM reporting an increase in energy absorbed by the new steel to be in the region of 12 – 14 percent.

The experimental engineering stress-strain curves obtained by AM are shown in Figure 47 below. The tensile strength of the new steel is lower than the current steel, but meets the minimum tensile strength specified for TC128-B material (81 ksi, or 558.5 MPa). However, the failure strain for the new steel is higher, indicating greater ductility.

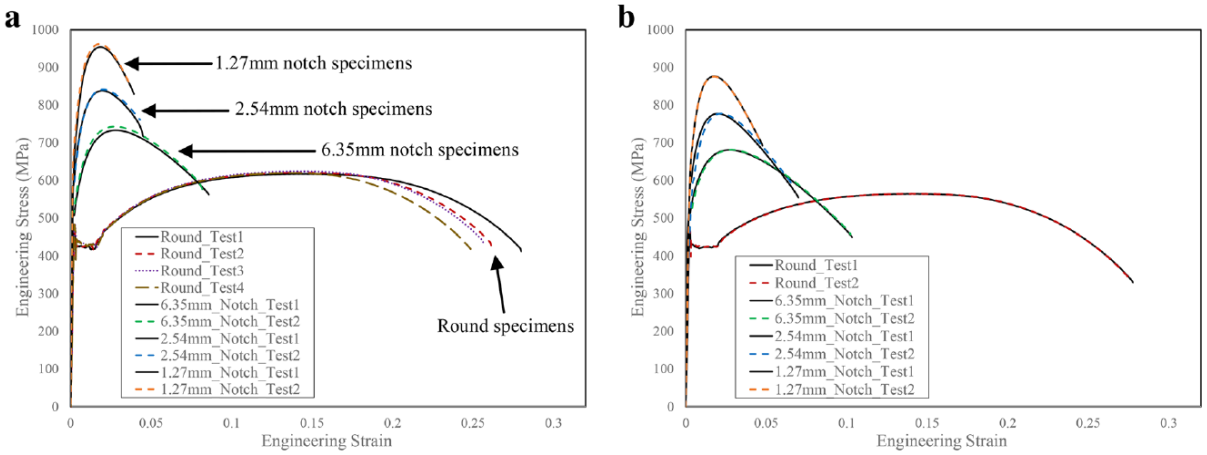

Figure 47. Experimental Engineering Stress-Strain Curves for Round and Notched Tensile Specimens: a) Current Steel, b) New Steel [36]

AM published the true stress-strain curves developed for use in FE analysis (Figure 48), along with the damage initiation criteria for both current and new steel (Figure 49). The damage model assumes that the failure initiates at the maximum load carrying capacity of the material (i.e., damage initiation) and then shows a subsequent degradation of stiffness progressing to complete failure (i.e., damage evolution). Figure 49 shows that damage initiation, which is defined in terms of equivalent plastic strain, is dependent on stress triaxiality, and that this is higher for the new steel than the current steel. Figure 49 also shows that the round bar and the notched tensile tests enabled AM to characterize the damage initiation criteria for tensile failure modes, but not for shear or mixed failure modes (i.e., stress triaxialities less than 0.33). Damage evolution, which defines the material behavior after damage initiation, is represented by its fracture energy dissipated per unit area during the damage process. AM calculated the fracture energy dissipated for both steels and found those for the new steel to be higher (Table 12).

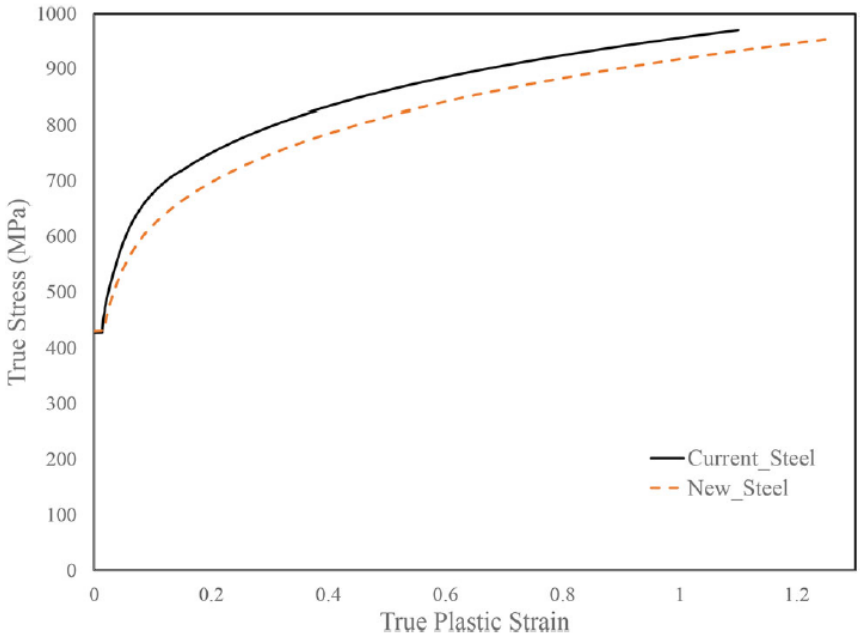

Figure 48. ArcelorMittal True Stress-strain Curves Derived for Use in FE Analyses [36]

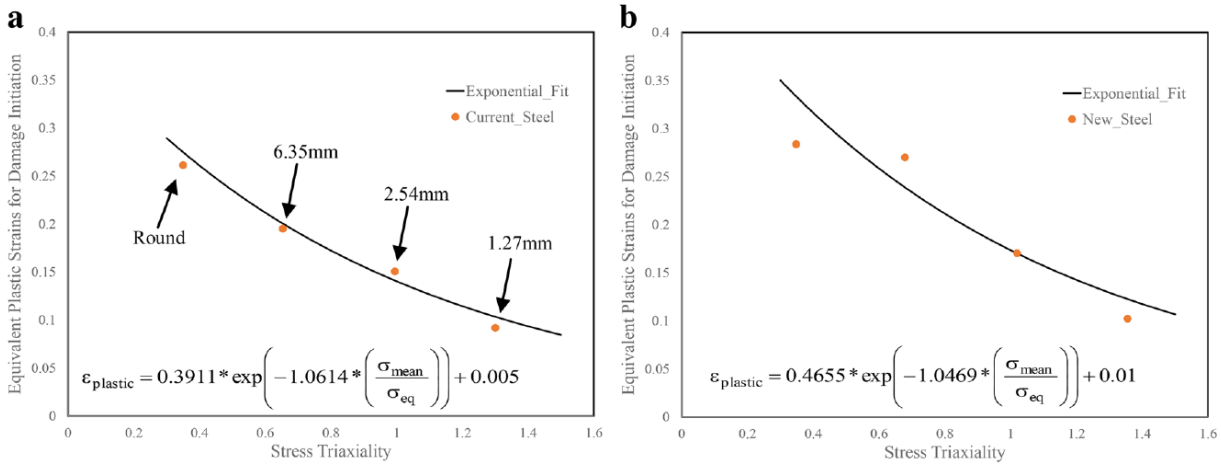

Figure 49. Damage Initiation Criteria for Current and New Steel Grades: a) Current Steel, b) New Steel [36]

Table 12. Fracture Energies for Current and New Steel Grades

Specimen	Current Steel (J/mm^2)	New Steel (J/mm^2)	% Difference
Round	3.15	3.25	+4.1
6.35 mm notch	0.96	1.15	+19.8
2.54 mm notch	0.57	0.86	+50.9
1.27 mm notch	0.46	0.64	+39.1

To assess the potential effectiveness of the new steel to improve puncture resistance, the full-scale model described in Section 2 was exercised using a modified version of the Actual TC128-B material referred to as 'Enhanced TC128-B.' Properties for the new virtual Enhanced TC128-B material were obtained by comparing AM current steel to new steel and scaling the Actual TC128-B by a similar amount:

- Current Steel x Scaling Factor(s) = New Steel
- Actual TC128-B x Scaling Factor(s) = Enhanced TC128-B

The AM true stress-strain curves and damage initiation criteria curves were digitized and overlaid to obtain scaling factors that could be applied to the Actual TC128-B material. As shown in Figure 50, it was calculated that factoring the current steel true-stress strain curve by 0.94 gave a reasonable approximation of the new steel. Similarly, as shown in Figure 51, factoring the current steel damage initiation criteria by 1.23 gave a good approximation of the new steel. Finally, the average percentage increase in fracture energy, obtained from Table 12, was calculated to be +28.5 percent. These scaling factors are summarized in Table 13.

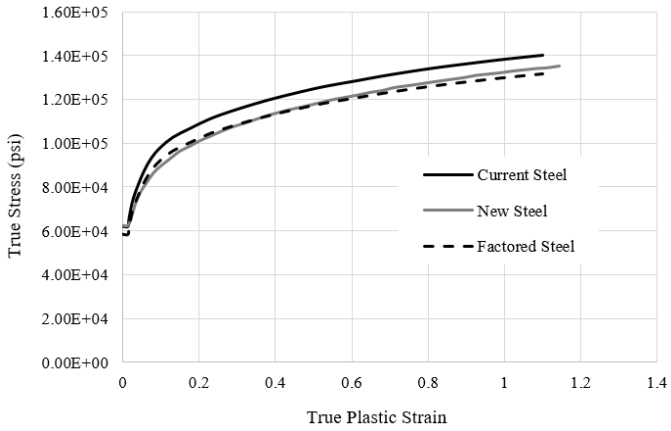

Figure 50. True Stress-strain Curves: Current and New Steel from ArcelorMittal, Factored Steel is Current Steel x 0.94

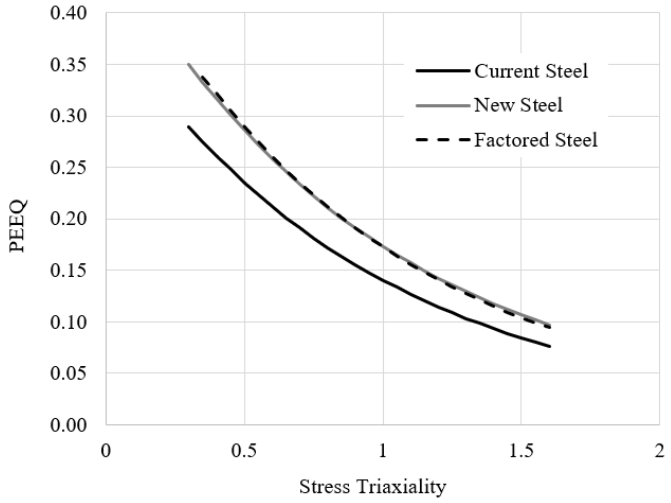

Figure 51. Damage Initiation Criteria: Current and New Steel from ArcelorMittal, Factored Steel is Current Steel x 1.23

Table 13. Scaling Factors Obtained by Comparing ArcelorMittal Current and New Steels

Material Parameter	Scaling Factor (Current to New)
True stress-strain	0.94
Damage initiation	1.23
Damage Evolution (Damage progression energy)	1.285

The Enhanced TC128-B material model properties obtained when the scaling factors in Table 13 were applied to the Actual TC128-B are shown in Figure 52 and Figure 53. The damage progression energy was initially 1400 in-lbf/in^2 and was increased to 1799 in-lbf/in^2.

The FE model developed to replicate the ASTM-E8 round bar tensile test and used to verify the original Actual TC128-B material model (Appendix B) was modified to include the new material properties developed for Enhanced TC128-B. The simulation was repeated and a new engineering stress-strain curve for Enhanced TC128-B obtained. This was compared to the Actual TC128-B material in Figure 54. The overall characteristics match those of the AM current and new steels (i.e., the Enhanced TC128-B material has lower strength and greater ductility).

To assess how these changes translate to improved puncture resistance, the full-scale model was used with Enhanced TC128-B in the puncture zone. Test 6 was repeated (indenter speed 15.16 mph) and the tank found to fail in a similar manner as before. The force-displacement response was compared to the baseline response using Actual TC128-B in Figure 55. The peak force exhibited by the Enhanced TC128-B version was ~6 percent lower, which aligns with the 0.94 scaling factor applied to the true stress-strain curve. The displacement to failure was otherwise very similar, indicating that the improved ductility of the Enhanced TC128-B did not offer significant benefit in this case.

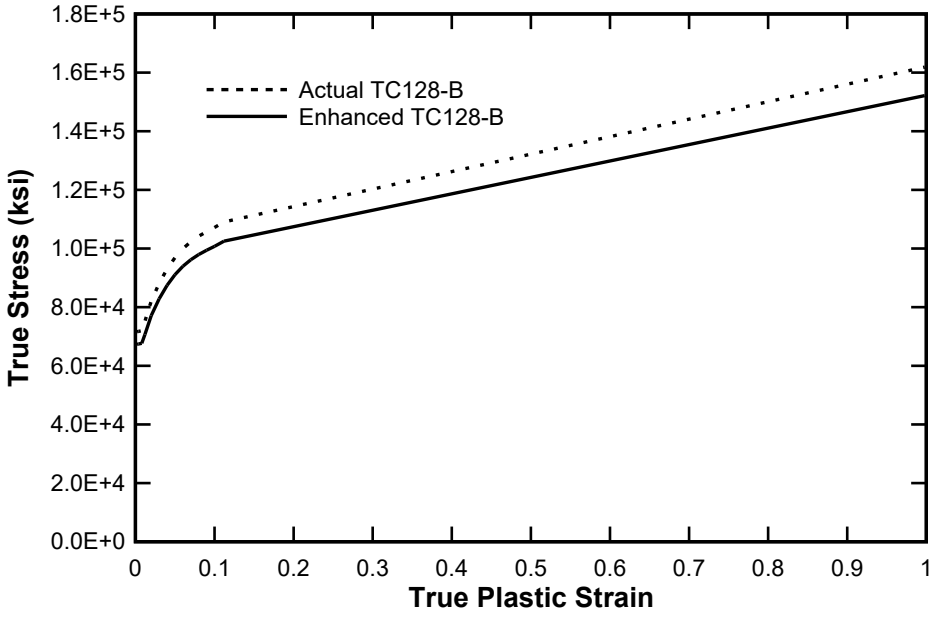

Figure 52. True Stress-strain Curves: Actual TC128-B and Enhanced TC128-B

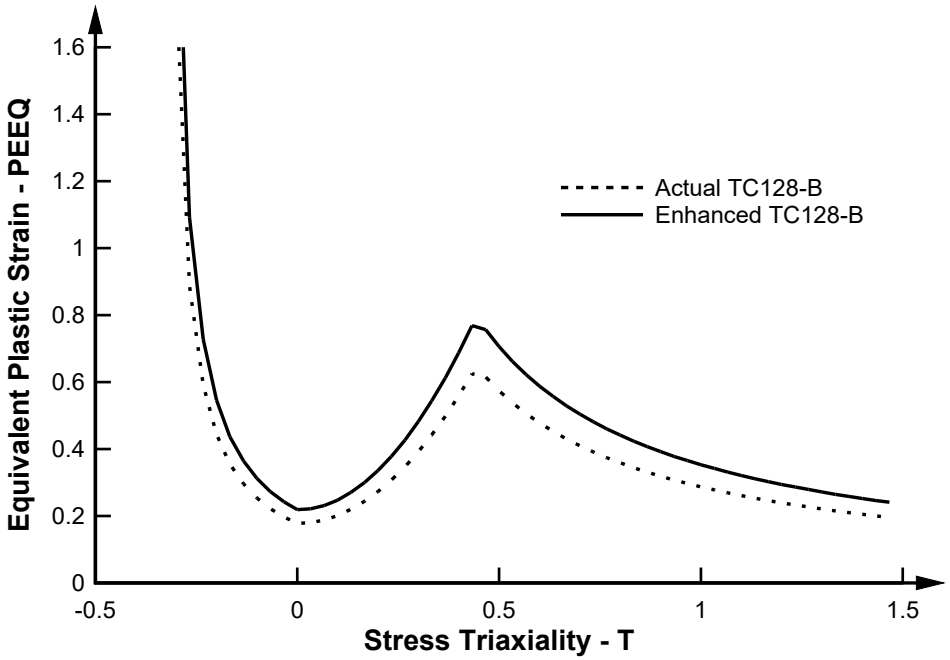

Figure 53. Damage Initiation Criteria: Actual TC128-B and Enhanced TC128-B

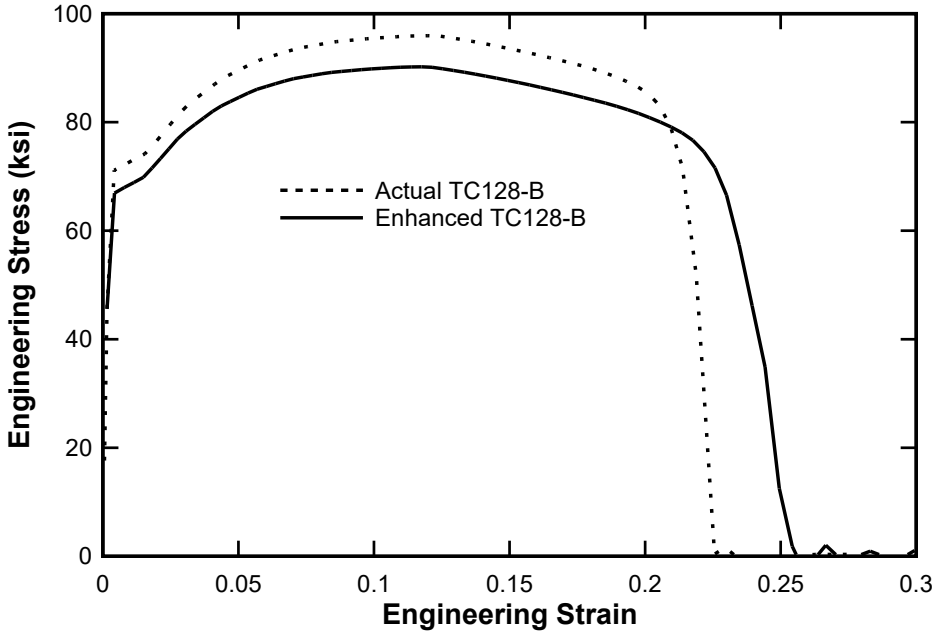

Figure 54. Engineering Stress-strain Curves: Actual TC128-B and Enhanced TC128-B

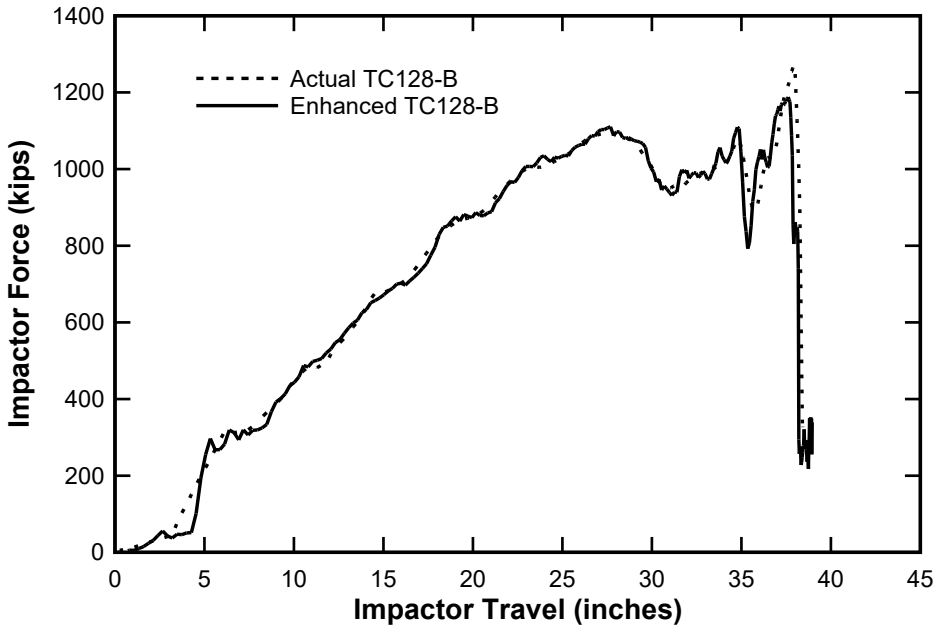

Figure 55. Force-displacement Response, Full-Scale Model 15.16 mph; Actual and Enhanced TC128-B Materials

4.2.1 Summary

AM developed a new low-carbon version of TC128-B that was shown to have lower strength but greater ductility, with a projected improvement in puncture energy in the range of 12 – 14 percent. Since the damage models developed for FEA are mesh dependent it was not feasible to simply implement the AM material model for new steel into the validated full-scale model. However, it was feasible to compare the differences observed between the properties of the AM current steel and new steel and apply these to the full-scale model. This was achieved by scaling the properties of the validated Actual TC128-B material by the same scaling factors observed between the current and new steel, to create a new virtual Enhanced TC128-B material.

Enhanced TC128-B was not shown to significantly improve puncture resistance. The full-scale model punctured at 15.16 mph with the new material model. The survival speed of the full-scale model using Actual TC128-B was calculated to be 13 mph. As shown in Table 14, the KE of the indenter increased by 16 percent from 13 to 14 mph, and by 36 percent from 13 to 15.16 mph. Therefore, consistent with AM findings, the change in material properties may result in an increase in puncture speed in the region of 1 mph. Therefore, while beneficial, the improved ductility of the steel is not sufficient to result in a step-change improvement in puncture resistance. It is potentially part of the solution, but not the solution itself.

Table 14. Summary of Kinetic Energies

Speed (mph)	KE (million-ft-lb)	% KE Increase from 13 mph	Comment
13.00	1.679	-	Baseline survival speed (Actual TC128-B)
14.00	1.947	16	Potential survival speed (Enhanced TC128-B)
15.16	2.283	36	Test Speed & Failure of Enhanced TC128-B

4.3 Mitigation – Shell Thickness

One clear solution for improving puncture resistance is to increase the thickness of the tank shell. There is already variation in thickness across different tank car specifications, with shell thicknesses as low as 0.562 inch (DOT 105J300W) and as high as 0.954 inch (DOT 105J600I) within the TIH tank car category [37]. To investigate the relationship between thickness and puncture resistance, the full-scale model was modified to consider shell thicknesses of 1.25 and 1.50 inches. This was achieved by keeping the mid-plane diameter of the tank shell constant and increasing the thickness of the mid-plane shells and solid element region. This meant that the diameter of the membrane part, representing the fluid boundary, reduced slightly as did the thickness of the foam insulation (i.e., by 0.2375 inches in the 1.25-inch configuration, and 0.3625 inches in the 1.50-inch configuration). The diameter of the jacket remained the same.

The resulting overall weight increase is shown in Table 15. Based on a standard DOT 105 chlorine-filled tank car having a weight of approximately 247,000 lbf, there is an approximate 39,000 lbf weight increase available to remain within the 286,000 lbf limit. The percentage weight increases shown in Table 15 were compared against the notional 39,000 lbf available. It shows that increasing the shell thickness to 1.50 in consumes approximately 90 percent of the available weight and therefore represents a reasonable, practical upper limit for shell thickness.

Table 15. Tank Shell Weights (Approximate)

Shell Thickness (in)	Shell Weight, Full (lbf)	Weight Increase (lbf)	% of Available Weight Increase
0.775	38,900	-	-
1.250	61,700	22,800	58
1.500	73,900	35,000	90

The team conducted a series of puncture analyses at varying speeds to establish the maximum survival speeds using a 12 x 12-inch indenter for 1.25- and 1.50-inch-thick shells. The results are summarized in Table 16. They show that increasing the shell thickness to 1.25 inches increases the puncture resistance by 6.0 mph and approximately doubles the amount of kinetic energy dissipated. Increasing the shell thickness to 1.50 inches gives a 9.0 mph increase in survival speed, which equates to approximately 3 times the kinetic energy.

Table 16. Results – Tank Shell Thickness Study

Shell Thickness (in)	Indenter Speed (mph)	Indenter KE (million-ft-lb)	Response of Tank Shell	Speed Increase (mph)	KE Increase (%)
0.775	13.0	1.679	Survives	-	-
0.775	14.0	1.947	Punctures	-	-
1.250	19.0	3.586	Survives	6.0	113.6
1.250	20.0	3.973	Punctures	-	-
1.500	22.0	4.808	Survives	9.0	186.4
1.500	23.0	5.255	Punctures	-	-

The force-displacement curves for the three survival speeds are shown in Figure 56. They show that the thicker shells can accommodate both higher peak forces and greater tank deformations. Figure 57 shows cross-sections through both cases at the time of peak force application.

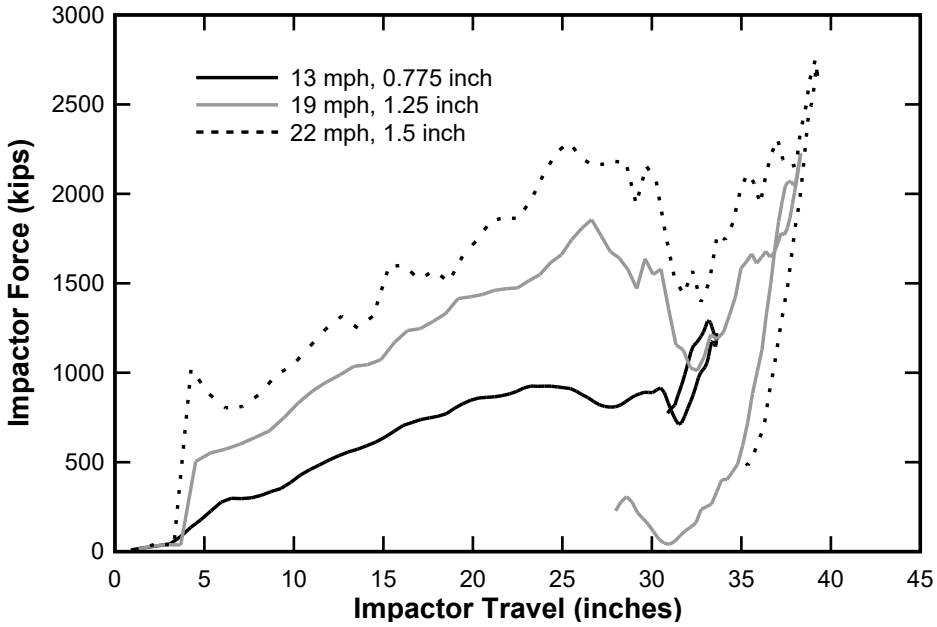

Figure 56. Force-displacement Response, Full-Scale Model: 0.775, 1.250- and 1.500-inch-thick shells – Survival Speeds

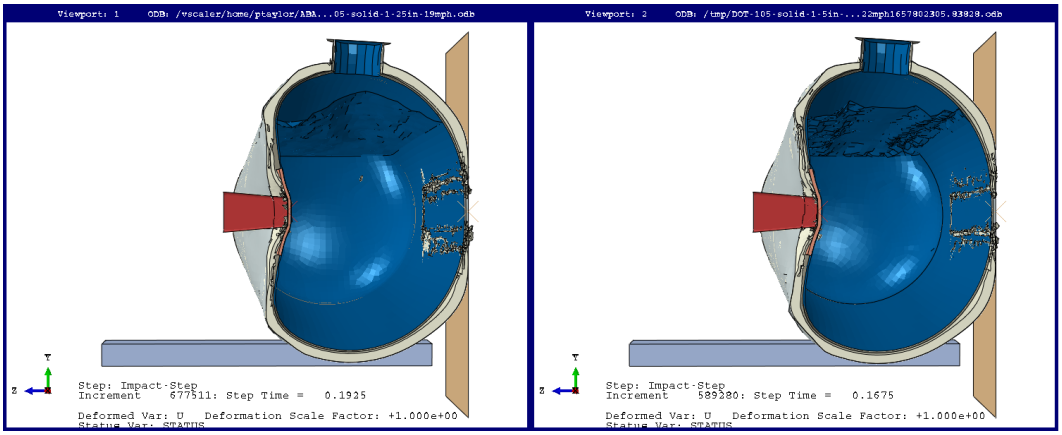

Figure 57. Cross-section through Tanks at Peak Force (left: 1.25 inch, right: 1.50 inch)

Increasing the shell thickness shows significant benefit. It increases the bending strength and stiffness of the tank, requiring more energy to deform it, and it improves the local puncture resistance.

4.3.1 Increased Shell Thickness with Enhanced TC128-B Material

Increasing the shell thickness to 1.5 inches increased the puncture resistance of the tank from 13.0 to 22.0 mph when using the Actual TC128-B material. To ascertain if using the more ductile material (i.e., Enhanced TC128-B) would improve the response further, the team repeated the full-scale simulations with 1.5-inch-thick shell. Researchers determined that the survival speed would increase to 23.5 mph using Enhanced TC128-B. This is a +1.5-mph improvement, and an increase in kinetic energy of 14 percent, which is consistent with the 12 – 14 percent predicted energy absorption calculated by AM [36]. The results are summarized in Table 17 and illustrated in the puncture chart in Figure 58. In this figure, the speeds shown are the calculated

survival speeds, where an increase in speed of +1 mph beyond these values would result in failure.

Table 17 and Figure 58 also show the results of an additional set of sensitivities undertaken in which the theoretical maximum shell thickness was used with Enhanced TC128-B material. The maximum shell thickness to stay within the 286,000 lbf weight limit was calculated to be 1.575 inches. This utilized approximately 99 percent of the available 39,000 lbf and resulted in a calculated survival speed of 24.5 mph. A sensitivity at double the baseline speed (i.e., 26 mph) resulted in failure of the tank. The general behavior of the tank at the 24.5 mph survival speed is shown in Figure 59, where (a) shows the tank before impact, (b) shows tank deformation before the entire tank assembly mobilizes, (c) shows tank compressed between indenter and wall, and (d) shows both the impactor rebounding away from the tank shell and the tank rebounding away from the wall. Figure 60 shows a plastic strain contour plot of the inside surface of the tank shell after the impact event. It shows that the material remains intact, with locally high plastic strains at the impactor corners.

Table 17. Enhanced TC128-B, 1.50 Inch Shell

Shell Thickness (in)	Indenter Speed (mph)	Indenter KE (million-ft-lb)	Response of Tank Shell	Speed Increase (mph)	KE Increase (%)
0.775*	13.0	1.679	Survives	-	-
0.775*	14.0	1.947	Punctures	-	-
1.500	23.5	5.255	Survives	10.5	213.0
1.500	24.5	5.962	Punctures	-	-
1.575	24.5	5.962	Survives	11.5	255.1
1.575	26.0	6.715	Punctures	-	-

*Indicates tank shell material is Actual TC128-B.

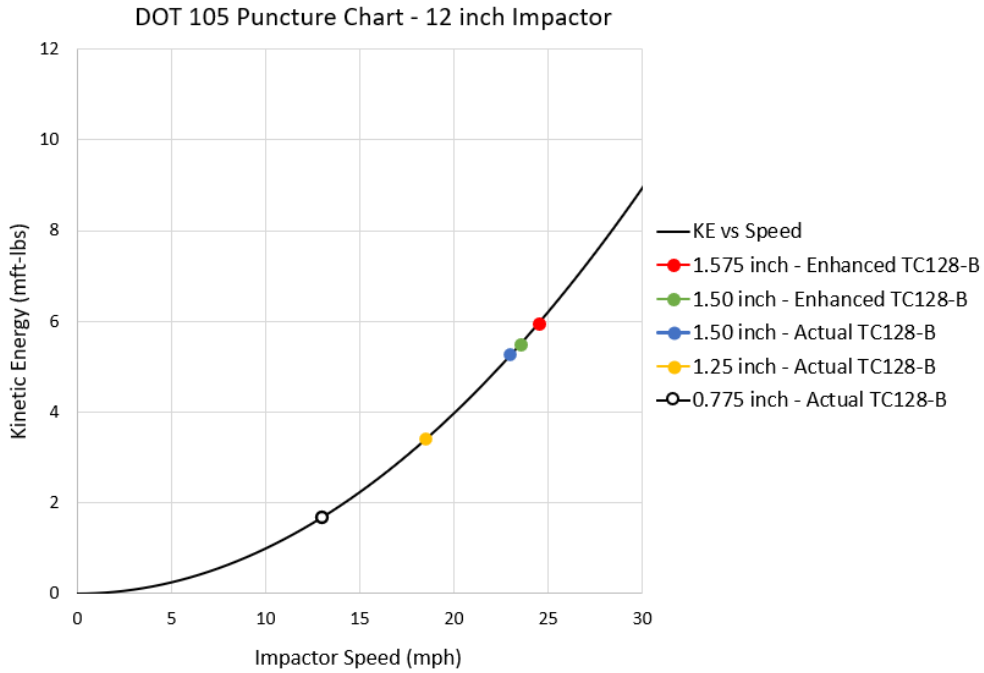

Figure 58. DOT-105 Puncture Chart Showing Calculated Survival Speeds (12-inch Indenter, Side Impact Scenario)

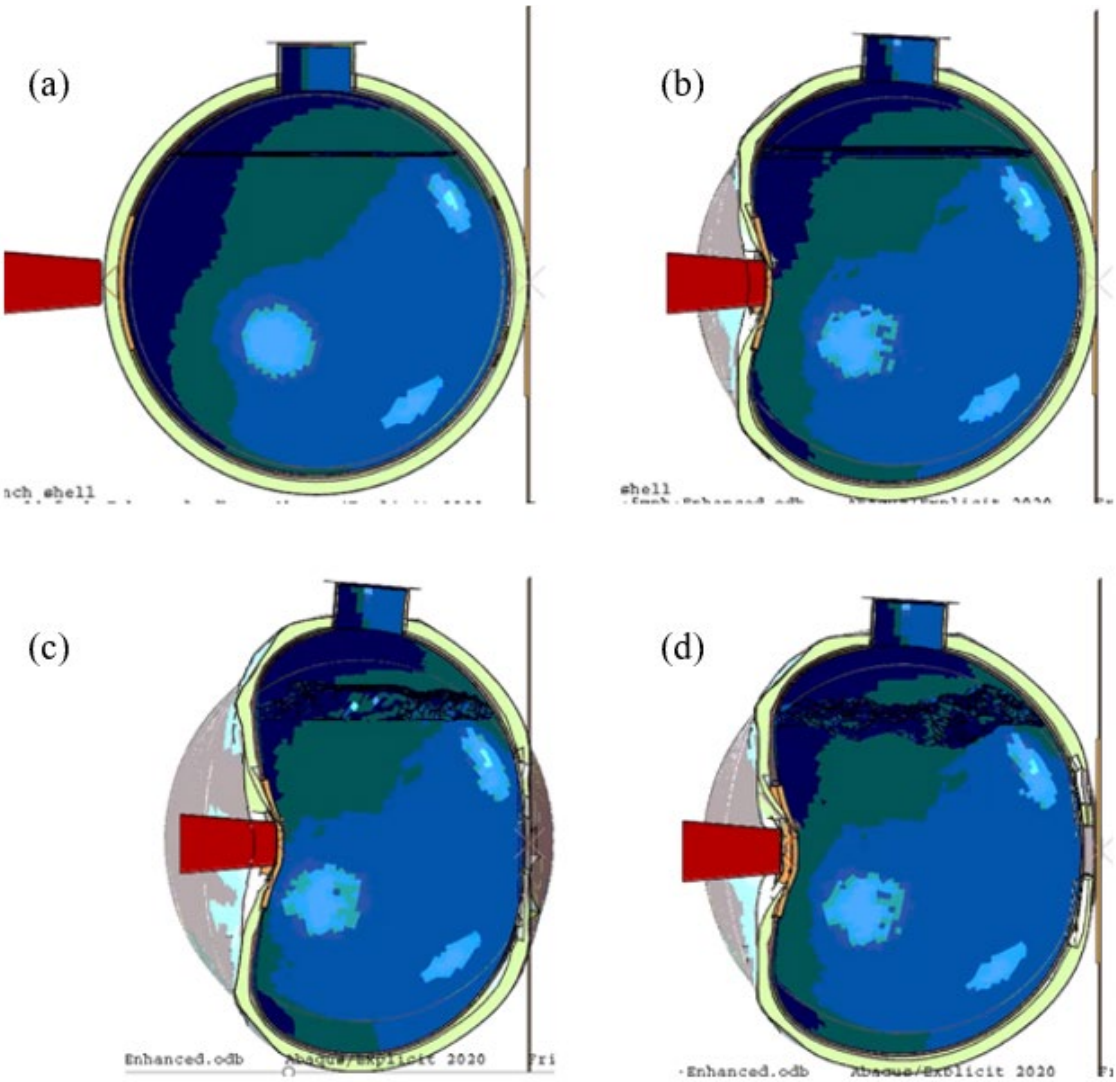

Figure 59. Overview of Response: 1.575-inch-thick Shell & Enhanced TC128-B at 24.5 mph

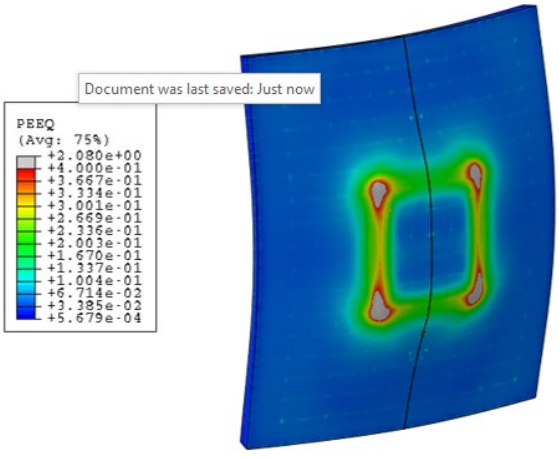

Figure 60. Plastic Strain Contour Plot (Upper Limit set to 0.4) Showing Inside Face of Tank Shell

4.3.2 Summary

In summary, the more ductile but slightly lower strength material further improved puncture resistance when considering thicker shells. At 1.5-inch-thick, the indenter displacement-to-failure increased from ~39.2 to 42.2 inches when using the Enhanced TC128-B material and in doing so facilitated greater energy dissipation. The calculated survival speed of 23.5 mph is 1.8 times greater than the baseline of 13.0 mph.

At the calculated theoretical maximum shell thickness of 1.575 inches, the survival speed increased to 24.5 mph when implemented with the Enhanced TC128-B material. This indicates that using thicker, 'better' steel could almost double survival speed and provide a resistance that is close to the average mainline derailment speed of 26 mph [37].

These results also indicated that improving ductility was of more benefit than increasing strength. This has been explored further in subsequent sensitivities.

Finally, the thickness sensitivities discussed in this section were undertaken using the full-scale FE model. Increasing the shell thickness increased the simulation times, primarily due to the large number of solid elements required in the thicker puncture zones. For example, in the case of the 1.5-inch-thick shell, the number of solid elements approximately doubled to ~1.32 million, which significantly increased the computational demand. This partly motivated the need to develop the more efficient quarter-symmetry sub-model described previously in Section 2 and used in subsequent sensitivities.

4.4 Mitigation – Material Properties

The thicker shells and the enhanced steel showed varying degrees of benefit in improving puncture resistance. To investigate some of the key factors for these improvements, different steel properties were considered separately in a parametric study. The features considered were mass, strength, and ductility.

4.4.1 Mass

Increasing the plate thickness of the tank shell from 0.775 to 1.5 inches resulted in a weight increase of approximately 35,000 lbf. This equates to approximately 12.4 percent of the overall tank car weight when using a 1.5-inch-thick shell. To determine the influence of the additional mass, a sensitivity was undertaken using the baseline full-scale model with 0.775-inch-thick shell and Actual TC128-B material and artificially increasing the additional mass gained in the thickness increase (35,000 lbf added). Accounting for the half-symmetric modelling approach, 17,500 lbf of non-structural mass[2] was assigned to the tank shell and the baseline simulation at a speed of 15.16 mph repeated. The results showed no significant change, with the tank again puncturing at an impactor travel distance of approximately 38 inches (Figure 61).

[2] Non-structural mass is akin to scaling the density of the target elements. The mass-inertia is increased, but the element otherwise performs the same.

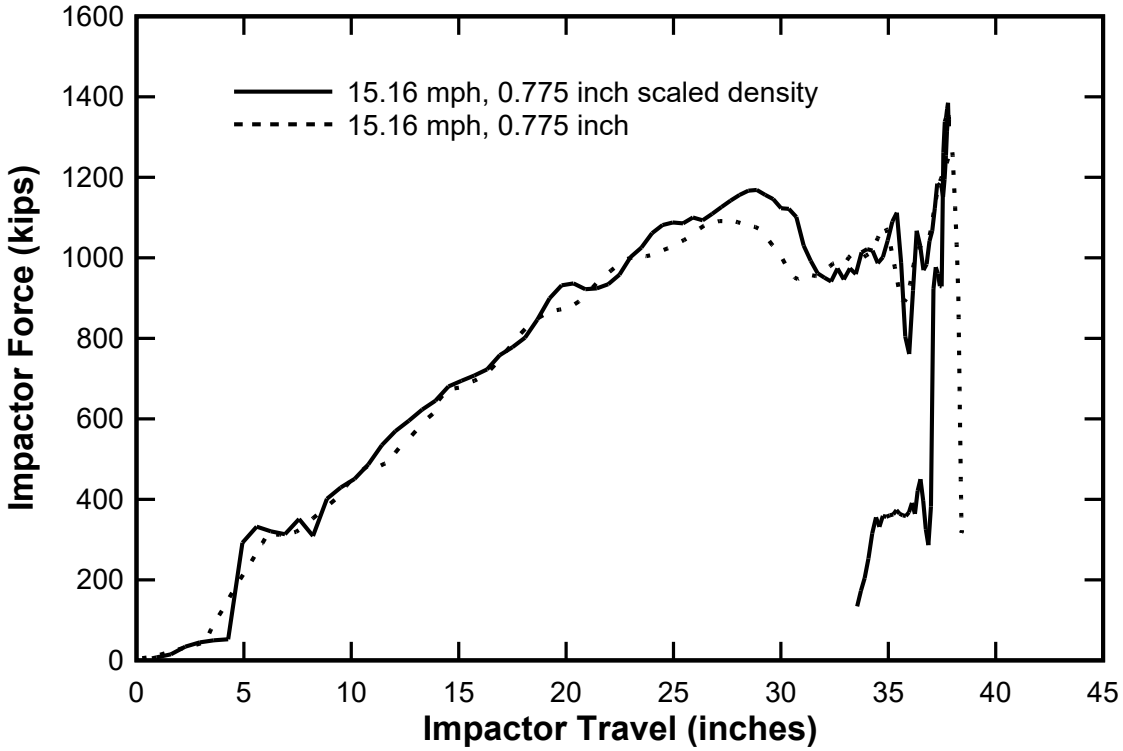

Figure 61. Force-displacement Response, Test 6 Baseline Results and Sensitivity with 35,000 lbf Added Mass

The results indicate that added mass of the magnitudes considered here has little consequence on the puncture resistance and therefore, improved performance of the 1.5-inch-thick tank car must be achieved elsewhere.

4.4.2 Material Strength

To investigate the relationship between steel strength and puncture resistance and provide insight into the key factors for the improvement offered by thicker steels, the team conducted a series of analyses using the quarter-symmetry tank car sub-model.

First, however, a high strength steel material model was developed and tested. Simple flat bar tensile test models were developed in accordance with ASTM E8 (8-inch gauge). The test, illustrated in Figure 62, was set-up to compare the characteristics of 0.775-inch-thick plate against 1.5-inch-thick plate, and therefore facilitate development of a new virtual material model that would replicate the strength of the thicker plate on the thinner specimen.

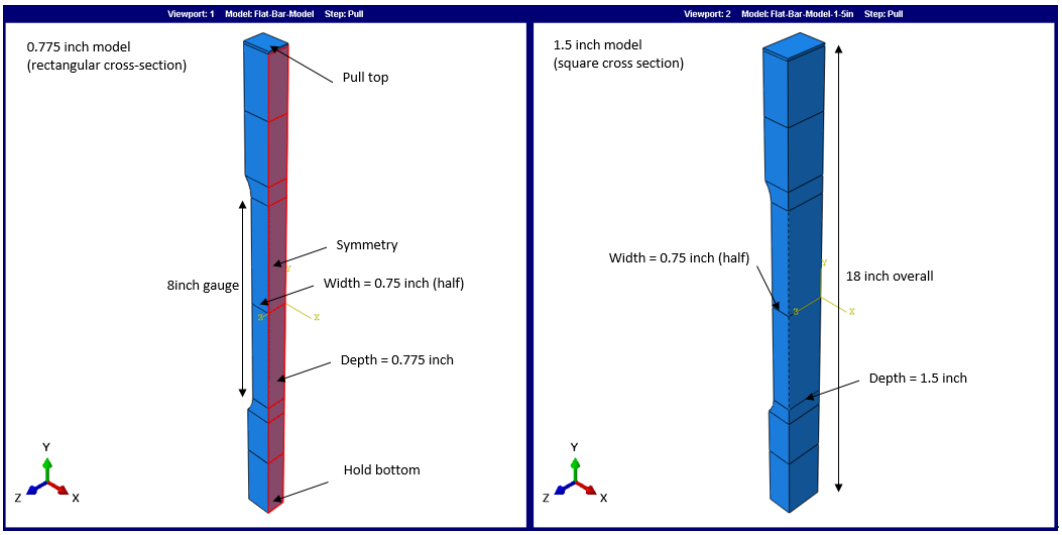

Figure 62. Flat Bar Tensile Test Setup: left: 0.775-inch Model, right: 1.5-inch Model

The force-displacement curves extracted from the analyses are shown in Figure 63. For the 1.5-inch-thick specimen, the peak force increased by ~94 percent (the same as the thickness ratio) and the energy dissipated at failure increased by 112 percent when compared to the 0.775-inch-thick specimen.

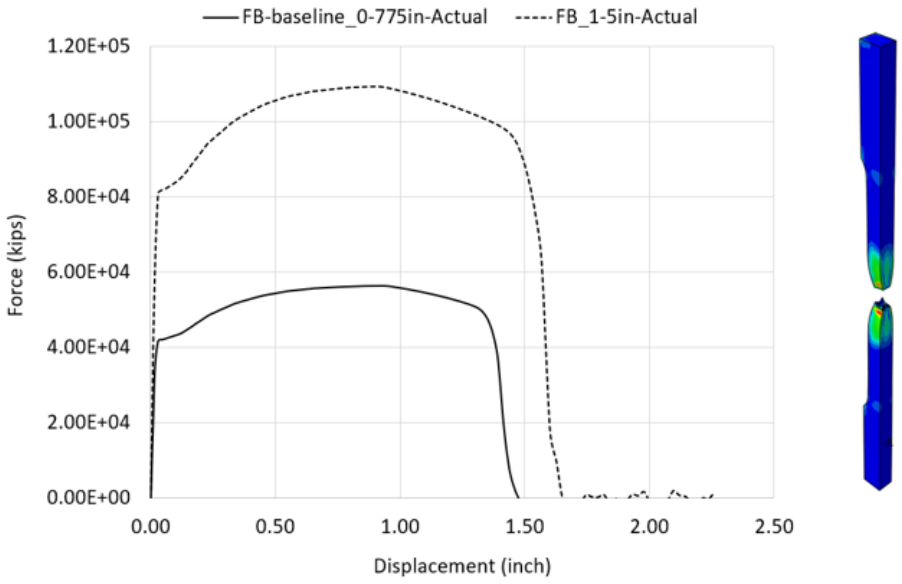

Figure 63. Force-displacement Response, 0.775- & 1.5-inch-thick Specimens Using Actual TC128-B Material Model

A new material model was then developed in which the strength of the Actual TC128-B steel was factored up by 1.935 (i.e., the thickness ratio of the 1.5-inch shell vs. 0.775-inch shell). This was achieved by factoring up the true stress-plastic strain curve as shown in Figure 64 with all other material parameters remaining the same. The new High Strength Actual TC128-B material model was assigned to the 0.775-inch-thick flat bar specimen and the tensile test was repeated. The engineering stress-strain curves and force-displacement curves obtained are shown in Figure 65. The results show that the yield stress and ultimate tensile stress were factored up by ~94

percent, and that the peak force obtained using the High Strength Actual TC128-B matches that obtained from the 1.5-inch-thick specimen. The overall energy absorbed at failure is somewhat less for the 0.775-inch high strength specimen. This difference is attributed to failure occurring at different stress triaxialities, manifesting because of the different geometries. Nevertheless, the High Strength TC128-B material model developed was considered sufficient to investigate the role of material strength in relation to puncture resistance.

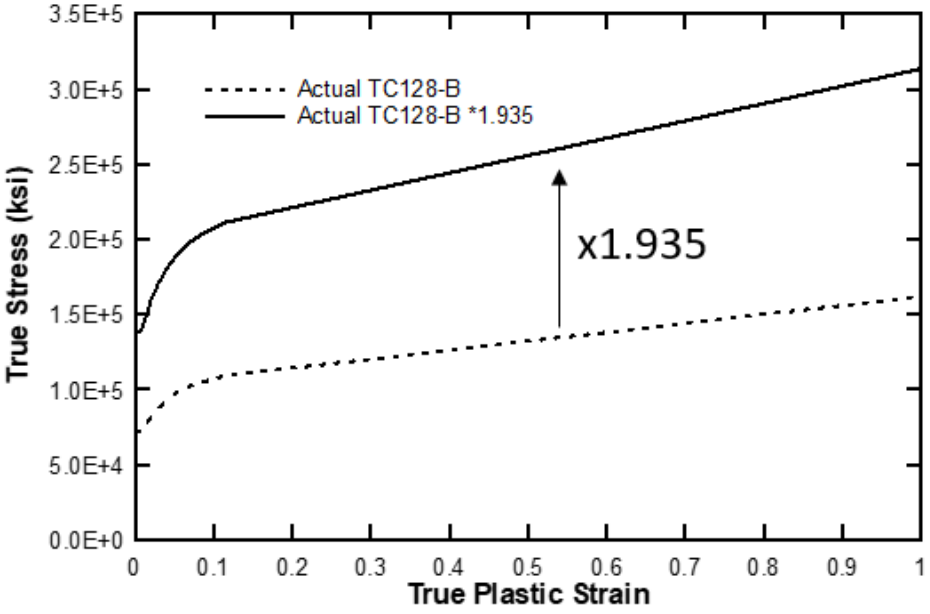

Figure 64. True Plastic Stress-strain Curves for Actual TC128-B & High Strength TC128-B

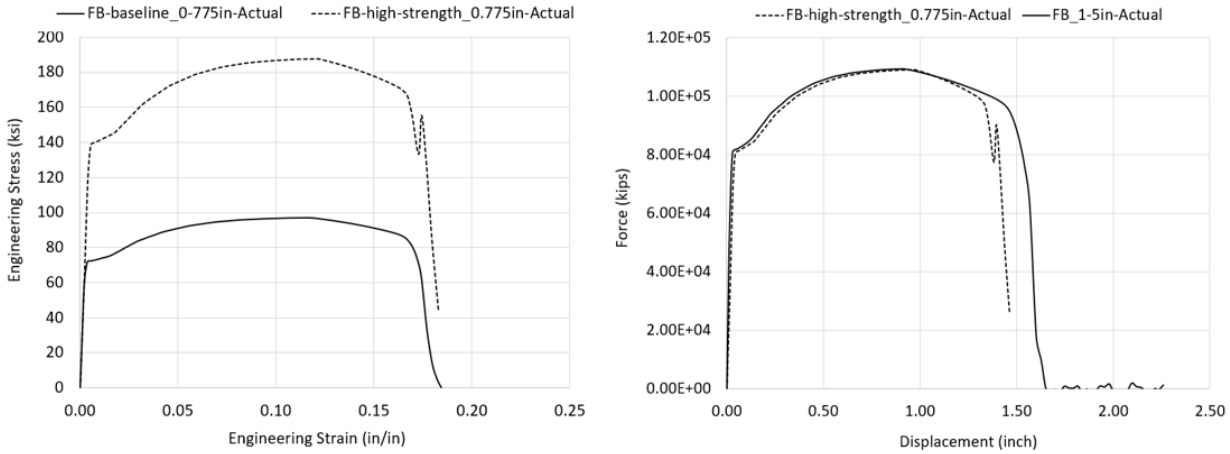

Figure 65. Left: Engineering Stress-strain Curves, Actual vs High Strength TC128-B, and right: Force-displacement response, 0.775-inch specimen with High Strength Actual TC128-B vs 1.5-inch Specimen with Actual TC128-B

The High Strength TC128-B material model was implemented into the tank car quarter-symmetry sub-model and the puncture speed varied in 1 mph increments until the survival speed was determined. This has been compared against the survival speed obtained from both the full-scale model and quarter-symmetry sub-model when a shell thickness of 1.5 inches was

implemented (Table 18). Note that the survival speed for the quarter-symmetry model at 1.5 inches is 1 mph higher than the equivalent full-scale model. This is considered a reasonable agreement, with the two models comparing well at the validation speed of 15.16 mph (Section 4.2). Furthermore, the quarter-symmetry model at 1.5-inches-thick failed at 23.5 mph (i.e., a small increase in speed).

Table 18. Survival Speed Summary, High Strength vs. Steel Thickness

Model	Shell Thickness (in)	Material	Indenter Speed (mph)	Response of Tank Shell	Speed Increase (mph)
Full-Scale	0.775	Actual TC128-B	13.0	Survives	-
Full-Scale	1.5	Actual TC128-B	22.0	Survives	9.0
Q. Sym.	1.5	Actual TC128-B	23.0	Survives	10.0
Q. Sym.	0.775	High Strength Actual TC128-B	20.0	Survives	7.0

The results show that the high strength steel improved the puncture resistance by 7.0 mph, which is approximately double the puncture energy (+137 percent). This is broadly consistent with the findings of Anderson et al. [38], who previously investigated puncture resistance in tank cars and concluded that '*roughly a 2-fold increase in puncture energy is possible with improved steels.*' Anderson et al. considered three different high strength-low alloy (HSLA) steels in comparison to grade TC128-B material, with the highest strength steel grade (HPS 100) having measured yield strengths in the region of 115 – 125 ksi, depending on strain rate. The yield strength of the Actual TC128-B considered in this study is 71.5 ksi, with the High Strength Actual TC128-B having a yield strength of 138 ksi, as summarized in Table 19.

Table 19. Comparison of Steel Strengths

Material	Yield (ksi)	Strength (MPa)
TC128-B (minimum)	50	345
Actual TC128-B	71.5	493
HPS 100 [38]	115	793
High Strength Actual TC128-B	138	951

The yield strength of the High Strength Actual TC128-B steel is therefore very much at the upper end of the scale and lies outside of the current TC128-B specification, which requires that the UTS is in the range of 81 – 101 ksi. The calculations also assume that ductility remains the same, whereas it is normal for higher strength steels to have reduced ductility. Nevertheless, the results show significant benefit in using higher strength steel grades and indicate that a significant proportion of the energy required to cause puncture of thicker steel can be translated to using steel with higher strength, provided ductility can be retained.

4.4.2.1 Material Strength vs. Structural Strength

The strength component considered above is the material strength (i.e., the resistance of the material to yielding and plastic deformation). However, there is also a structural strength and a

global resistance to bending provided by the 1.5-inch-thick shell that is not captured by simply increasing the strength of the material. This is illustrated in Figure 66, which shows a relatively flat response of the tank shell in front of the indenter in the 0.775-inch-thick high strength case. The 1.5-inch-thick shell by contrast resists the flattening behavior, which increases the local punching effect. This behavior is further apparent when comparing the indenter force-displacement curves (Figure 67) which shows that the global stiffness of the 1.5-inch-thick shell is significantly greater than the 0.775-inch-thick shell with high strength material. Therefore, more energy is absorbed by the thicker shell over shorter deformation.

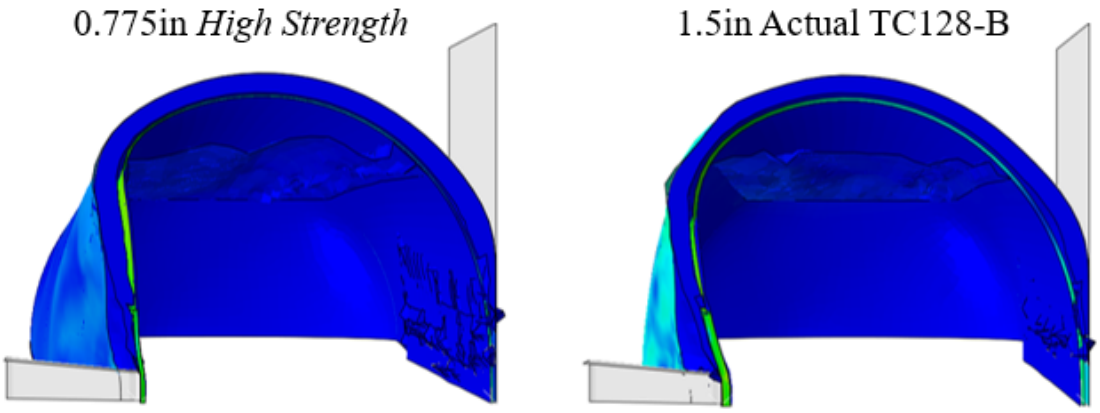

Figure 66. Comparison of Global Deformation at 22 mph; 0.775-inch-thick High Strength vs. 1.5-inch-thick Actual TC128-B

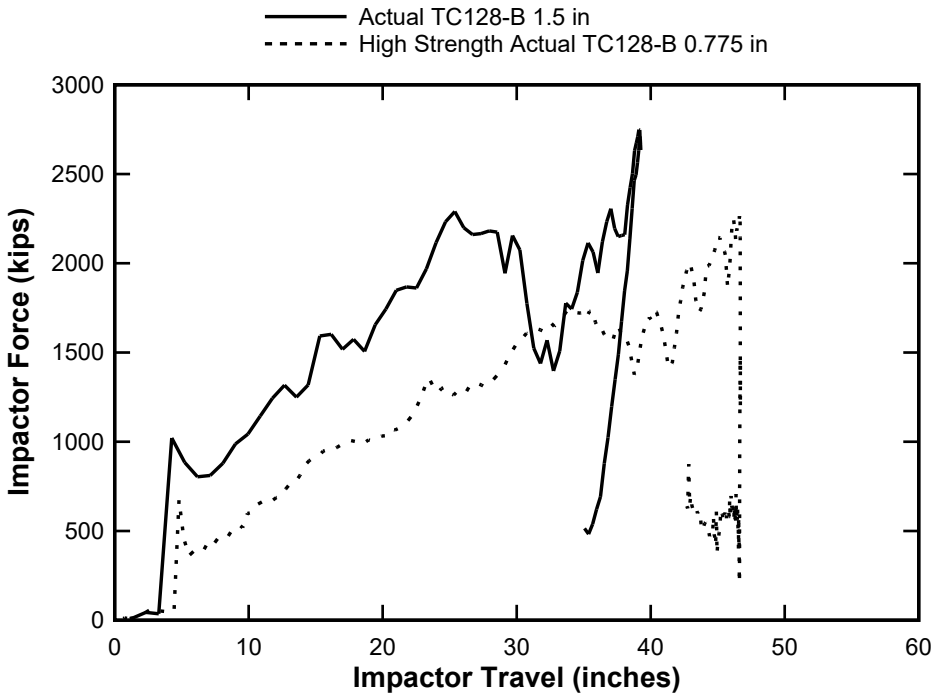

Figure 67. Force-displacement Response at 22 mph, Actual TC128-B 1.5-inch vs High Strength TC128-B 0.775-inch

4.4.3 Ductility

The results obtained from simulations using the Enhanced TC128-B material (Section 4.2 and Section 4.3.1) indicated that improved puncture resistance could be obtained by increasing ductility while reducing the strength of the steel. An approximate 6 percent reduction in steel strength, coupled with a 23 percent increase in elongation to failure resulted in approximately 12 – 14 percent improvement in puncture energy. This suggests that puncture resistance is strongly dependent on ductility.

To further investigate this, a new virtual High Ductility version of the Actual TC128-B material model was developed. Recall the Actual TC128-B material model was developed using a B-W fracture locus in which the plastic strain at failure is dependent on stress triaxiality. In the High Ductility version, the single change made to the material model was to factor the B-W curve up by 4, as shown in Figure 68.

The Round Bar model previously developed to verify the Actual TC128-B material model (Appendix B) was utilized with the new High Ductility Actual TC128-B material. The resulting engineering stress-strain curves are shown in Figure 69, where the High Ductility results are compared against the baseline Actual TC128-B results. The increase in ductility is clear, although it should be noted that the baseline Actual TC128-B only just meets the minimum ductility requirements (22 percent elongation for 2-inch gauge). It is also noted that while the elongation of the High Ductility model is more than 40 percent, it is not significantly higher than some other tank car steels previously tested. For example, Kirkpatrick [39] compared the engineering stress-strain curves of three tank car steels, with 'Test 2' material showing a failure strain in the region of 30 – 35 percent.

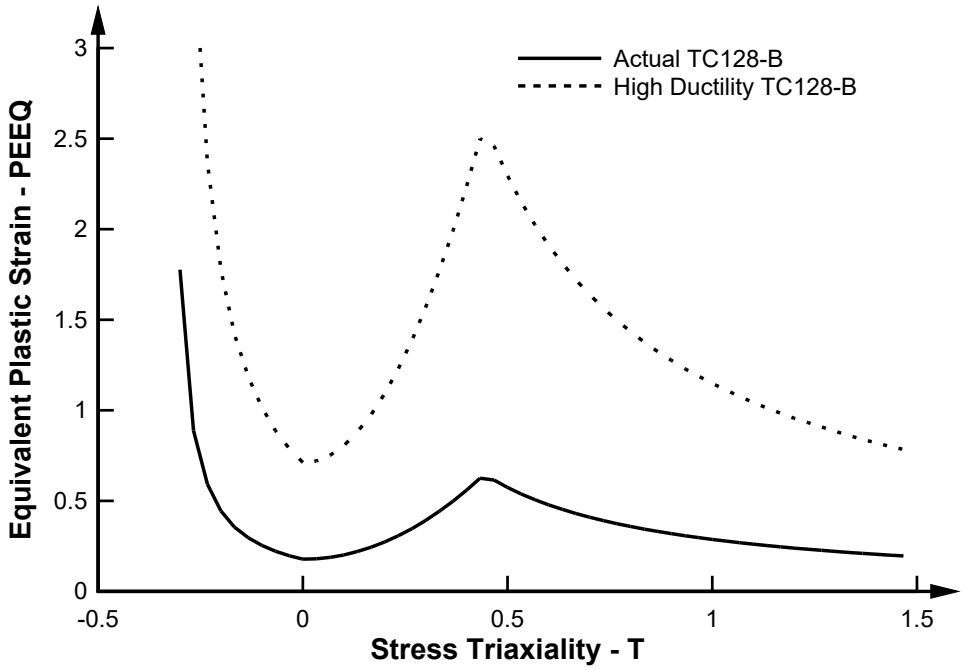

Figure 68. B-W Damage Model for Actual TC128-B & High Ductility Actual TC128-B

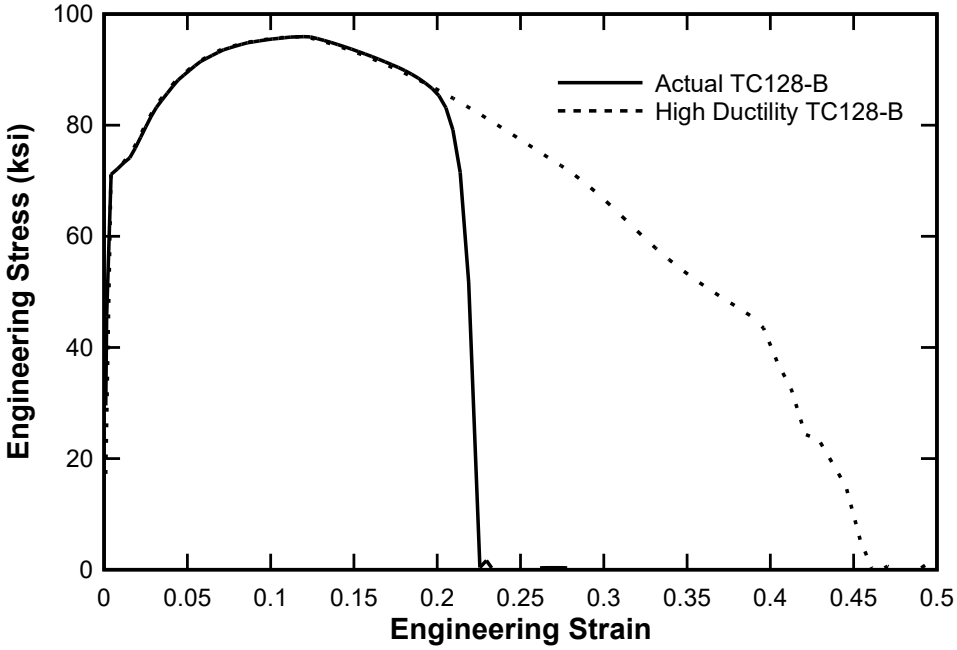

Figure 69. Engineering Stress-strain Curves Produced from Round Bar (2-inch Gauge) Model Using Actual TC128-B & High Ductility Actual TC128-B

The High Ductility material model was then implemented in the quarter-symmetry tank car model and a series of simulations undertaken in which the indenter speed was increased in 1 mph increments until failure was observed. The results are summarized in Table 20, where in each case a 1 mph increase in speed resulted in puncture of the tank shell.

Table 20. Survival Speed Summary, High Ductility vs. Steel Thickness

Model	Shell Thickness (in)	Material	Indenter Speed (mph)	Response of Tank Shell	Speed Increase (mph)
Full-Scale	0.775	Actual TC128-B	13.0	Survives	-
Q. Sym.	0.775	*High Ductility* Actual TC128-B	19.0	Survives	6.0

The results show that the survival speed increased by 6.0 mph, which is a 114 percent increase in kinetic energy, again supporting the view that improved steels could approximately double the puncture energy of tank cars. Figure 70 compares the force-displacement response obtained from the quarter-symmetry model when the baseline tank car using Actual TC128-B material fails at an indenter speed of 14 mph, versus that of the High Ductility model where failure occurs at a speed of 20 mph. The impactor travel increases from ~36 to 48 inches, and the peak forces increase by 40 percent, from 1309 to 1833 kips. An overview of the High Ductility model at the time of peak displacement in the 19-mph survival case is shown in Figure 71. Local deformation of the shell behind the indenter is notably higher than in previous cases due to the increased ductility (Figure 72).

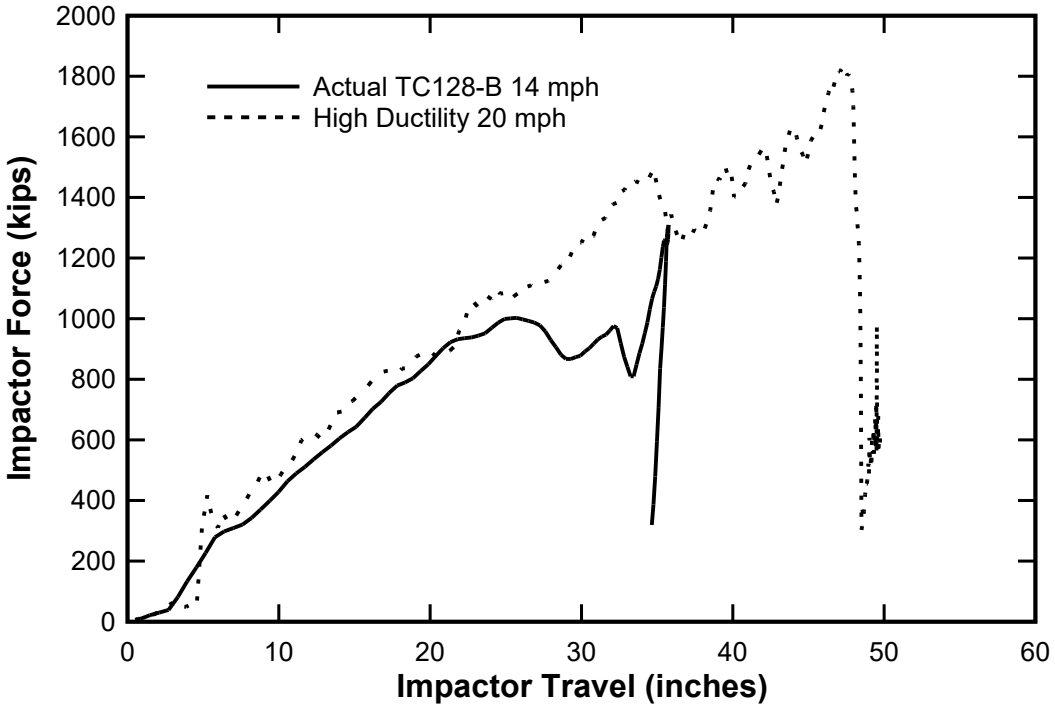

Figure 70. Force-displacement Response, Actual TC128-B vs High Ductility TC128-B at 14 & 20 mph

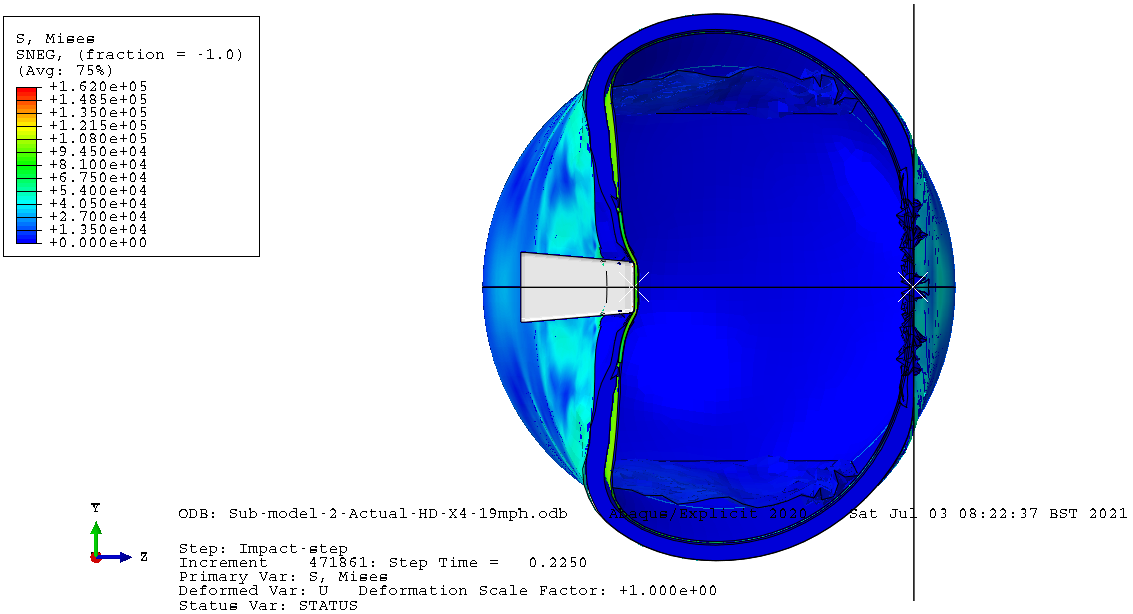

Figure 71. Section through High Ductility Model, 19 mph, at Time of Peak Indenter Displacement

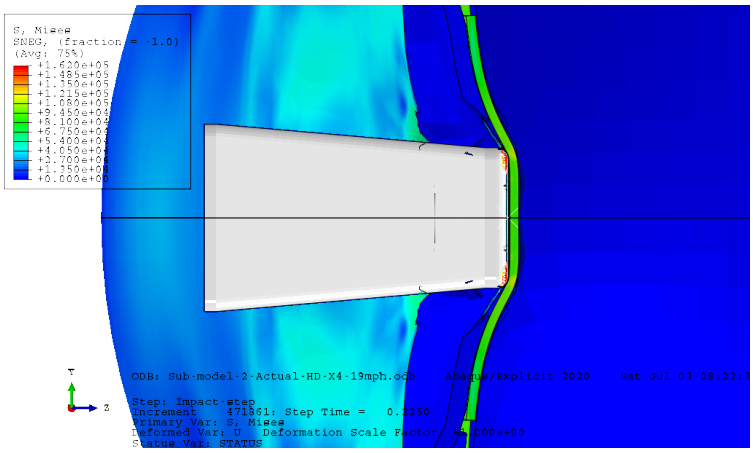

Figure 72. Local Section View through High Ductility Model, 19 mph, at Time of Peak Indenter Displacement

4.4.4 Summary

The parameters of mass, strength, and ductility were investigated in isolation. The influence of mass was investigated by artificially scaling up the density of the tank shell steel. The mass increase was equivalent to increasing the shell thickness from 0.775 to 1.5 inches. It was found to have little influence on the overall puncture resistance primarily because the relative overall increase in the tank car mass was small (12.4 percent).

The material parameters strength and ductility were investigated by developing virtual high strength and high ductility material models, and in both cases significant improvements in puncture resistance were observed. There is a clear benefit to improving steel ductility that has been recognized by the tank car industry for some time. The Actual TC128-B material used as the baseline in these analyses and validated against physical tests of tank cars performed in the late 1980s lies very much at the lower end of the ductility scale, only just meeting the minimum requirement of 22 percent elongation for a 2-inch gauge. AAR have petitioned for the timely removal of such legacy TIH/PIH tank cars from service [40], specifically the non-normalized[3] cars. The benefit of increasing steel ductility was also demonstrated in the assessment of AM's low-carbon Enhanced TC128-B steel, where puncture resistance improved when ductility was increased and strength reduced.

Increasing steel strength was shown to provide similar benefit, but higher strength steels would typically be characterized by having reduced ductility. This feature of increasing strength while reducing ductility was not captured in this assessment. Furthermore, fabricating the tank shell from high strength steel would add complexity to the manufacturing process, particularly where heat treatments are used, since this could affect the strength of the steel. One method of implementing a high strength steel as part of a mitigation solution would be to use it in a double-tank arrangement, where the high strength steel would be used as an external protection mechanism and therefore not subject to the same manufacturing requirements as the tank shell. This is discussed further in the next section of the report.

[3] Normalizing is a heat treatment process used to improve metal ductility and toughness after it has been subjected to thermal or mechanical hardening processes.

4.5 Mitigation – Multi-Plate Solutions

4.5.1 Background

In the ATCCRP (see Section 1.1) researchers investigated various protection strategies over the course of a decade and arrived at the following key conclusions [41]:

1. 'No new high technology design or material that produced significant new protection levels (e.g., composites, crushable foams, advanced engineered energy absorbing sandwich panels) has been identified. Traditional tank car designs with monolithic layers of good quality steel are relatively efficient structures for resisting the impact threats in the railroad safety environment.'
2. 'The only option identified for possible improvements in puncture protection over the HM-246 interim specification car designs are potential optimized sandwich designs, requiring alternative steels in the jacket (outer tank) for enhanced puncture protection. This conclusion is based on puncture analyses performed for various tank design configurations. Functional tank car designs for these sandwich cars were not developed in the research and the protection levels have not been proven by testing.'

The researchers found that adopting a double tank design, or "tank-within-a-tank" concept, yielded somewhere in the region 45 – 100 percent improvement in puncture energy over the HM-246 interim designs depending on the original tank car specification. Further improvement was demonstrated by changing the jacket material to a high strength (HY-130) or high ductility (304L stainless) steel.

4.5.2 Layered Plate Solution

The double tank concept assessed by ATCCRP involved increasing the plate thickness of the outer jacket to create a structural barrier offset from the tank shell. In some cases, material was moved from the tank shell to the jacket, although this was shown to be of little benefit. In the current research, investigation of the relationship between shell thickness and puncture resistance indicated similar, if not slightly improved, puncture resistance, albeit with a single impact scenario considered and an overall much smaller data set. However, previous tank car puncture research had not considered if there was any merit in splitting a thick plate into multiple layers of thinner plates. This differs from the double tank concept in that the tank shell itself would be split into multiple layers and layered on top of one another, as opposed to being offset like the jacket. This layered plate concept was therefore evaluated using a series of FE models.

4.5.2.1 Punch Plate Model

During research conducted by ARA [39] a series of experimental punch tests were conducted in which 0.488-inch-thick TC128-B plates were tested to failure. The tests were used by ARA to validate a TC128-B material model, characterized using a B-W failure surface, for use in subsequent full-scale FE simulations. The material characterized was 'Test 2' TC128-B, details of which can be found in Appendix B. Punch tests were carried out on three configurations, as summarized in Table 21, with force-displacement curves extracted each time. Numerical simulations of the punch tests were performed by ARA using LS-Dyna, with generally good agreement achieved (shown in Figure 73). The experimental punch tests were performed at a rate of 1-inch/minute and the punch and manhole radii were set to 0.3 and 1.0 inches, respectively.

Table 21. ARA Punch Plate Tests

Test	Punch Diameter (in)	Manhole Diameter (in)
Test-50-1	1.0	2.5
Test-50-2	1.5	3.0
Test-50-3	2.0	3.5

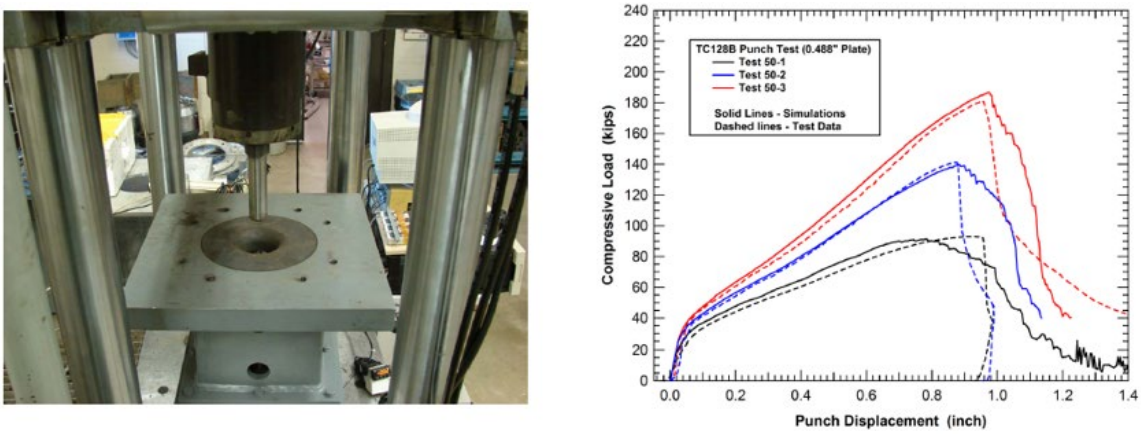

Figure 73. Punch Test and Comparison of Experimental and Numerical Results

In this research effort the team first replicated the three ARA punch tests by numerical simulation before investigating the effects of varying plate thickness and plate layering. A quarter-symmetry FE model was developed in Abaqus with the Explicit solver used to simulate the tests. Material properties for 'Test 2' TC128-B were developed (see Appendix B) and assigned to the plate. The punch and manhole were modelled as rigid bodies with the plate modelled using deformable solid elements with an element size of 0.085 inches and a coefficient of friction of magnitude 0.3 was assigned globally[4]. A cross-section through the model is shown in Figure 74; a mirror plane has been used to give the impression of the full model.

Figure 75 shows an overview of Test-50-3 at the point just prior to the onset of failure (left image) as well as the progressive failure of the plate (right image), where failure initiates on the underside of the plate. A plug approximately the same diameter as the punch was ejected in each case, which is consistent with the experimental results. Force-displacement curves for each of the tests were extracted and compared to the experimentally obtained values. The results (Figure 76) showed that generally good agreement was achieved. The calculated displacement at failure in 2 out of 3 cases was within 1 percent of the experimental values, while the peak force in each case was within 10 percent. On average the simulated peak force was 8.6 percent lower than the experimental force. The greatest error observed was the displacement to failure in Test-50-1, although notably the ARA simulation showed a similar response and magnitude of error.

[4] Sensitivities were conducted on CoF using 0.3, 0.4, and 0.5, with little observable difference in the results.

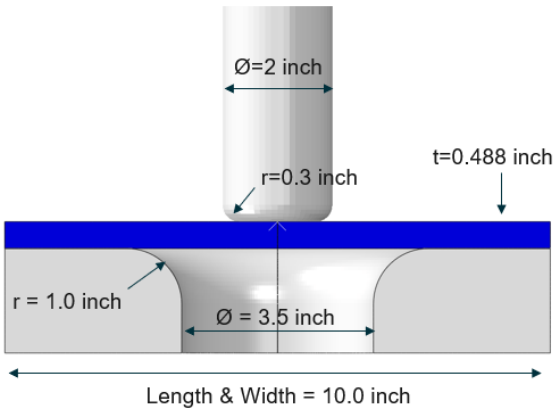

Figure 74. Punch Test Setup, Abaqus

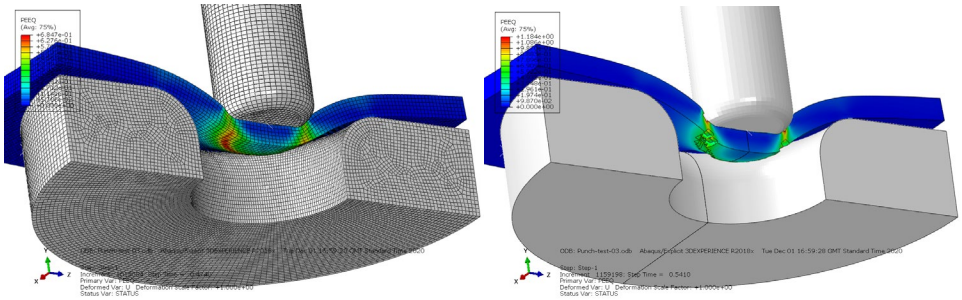

Figure 75. Punch Test-50-3: Left, Mesh Shown; Right, Failure Progression

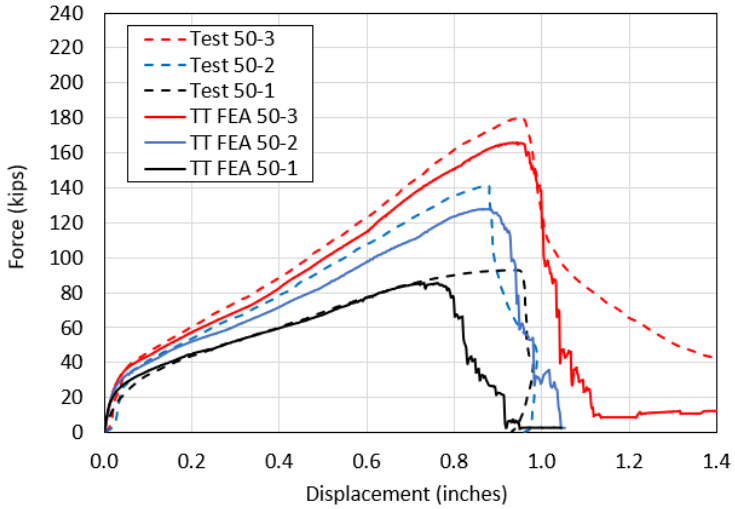

Figure 76. Punch Test: Force-displacement Response, Experimental vs. TT FEA

To initially compare the puncture resistance of a single monolithic steel plate against multiple layered plates of equivalent overall thickness, the team conducted a series of simulations in which a single 1-inch-thick plate was compared against two 0.5-inch-thick plates. The simulations considered are summarized in Table 22. First, the original Test-50-3 setup was adopted, but with the revised plate configurations (Figure 77) before further sensitivities were carried out in which manhole diameter was increased to 6.0 and 7.0 inches. The diameter of the manhole was increased to impose more bending and less shear.

Table 22. New Punch Plate Simulations

Test	Plate Configuration	Punch Diameter (in)	Manhole Diameter (in)
Test-50-3	Original (0.488 in)	2.0	3.5
Test-50-3 (single)	Single 1 in	2.0	3.5
Test-50-3 (double)	Two ½ in	2.0	3.5
New 6-in single	Single 1 in	2.0	6.0
New 6-in double	Two ½ in	2.0	6.0
New 7-in single	Single 1 in	2.0	7.0
New 7-in double	Two ½ in	2.0	7.0

Results from the initial set of simulations are shown in Figure 77, where in the two-plate configuration plate separation occurs after failure. The force-displacement plot shows that the single plate outperforms the double plate across the three key metrics: peak force, displacement to failure, and energy absorbed. When the manhole diameter was increased this trend continued, albeit the difference between the single and double plate response was less pronounced. The results from the 6.0- and 7.0-inch manhole studies are shown in Figure 78. In both cases the peak force was approximately equal between the single and double plates, but the puncture energy was on average 16.5 percent less for the double plate configuration owing to the reduced stiffness.

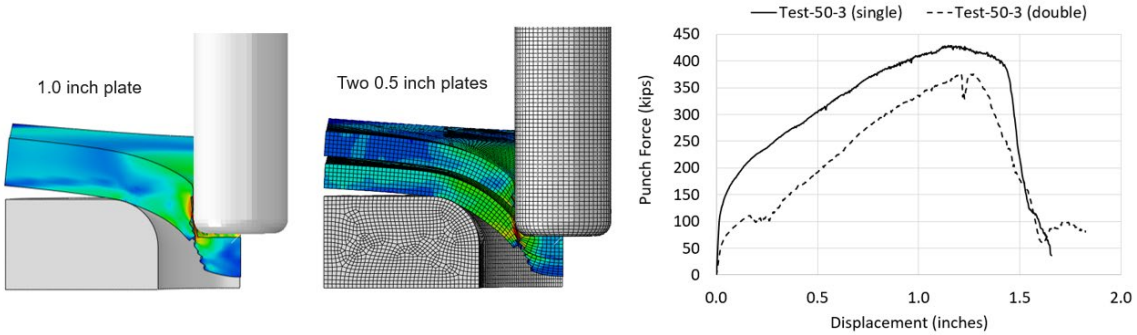

Figure 77. Test-50-3 Comparing Results with New (Double) Plate Configurations

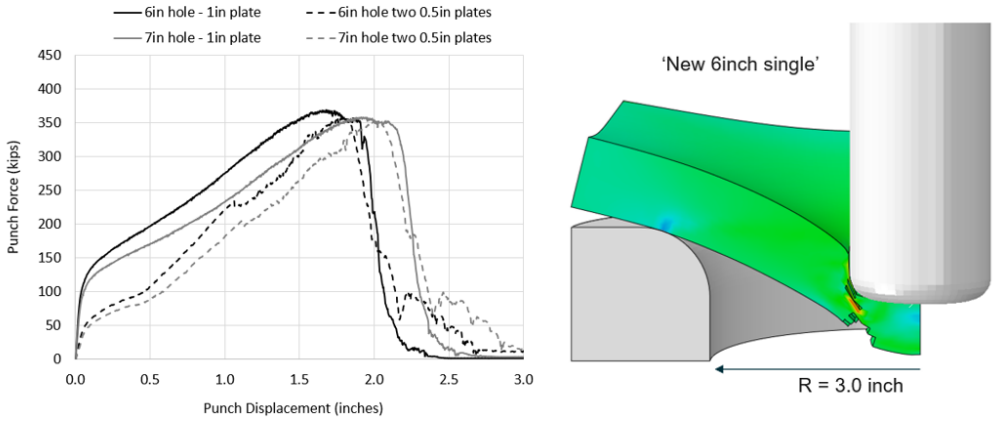

Figure 78. Results from 6.0- and 7.0-inch Plate Tests

While the results from the Punch Plate Model indicated that it was detrimental to split the plates, the puncture mode was strongly influenced by local shear and did not consider the wider influence of boundary conditions and constraints. An alternative flat plate test was therefore devised in which some of those factors could be considered.

4.5.2.2 Flat Plate Model

The Flat Plate Model is shown in Figure 79. It is a quarter-symmetric model featuring a solid element puncture region at the center, connected to a shell element region using tie constraints. The plate was assigned the material properties developed for Actual TC128-B and the element size in the solid element region was set to 0.085 inches (i.e., that for which the B-W failure model had been calibrated). The outer edges of the plate were fixed and a rigid 12 x 12-inch indenter was assigned a constant velocity of 15 mph to penetrate the plate. In an initial set of sensitivities three different plate thicknesses were considered (0.775, 1.25 & 1.50 inch) and the force-displacement response of the indenter was recorded (Figure 80). The results, summarized in Table 23, show that the percentage increases in peak force and puncture energy are broadly consistent with the magnitude of increased plate thickness.

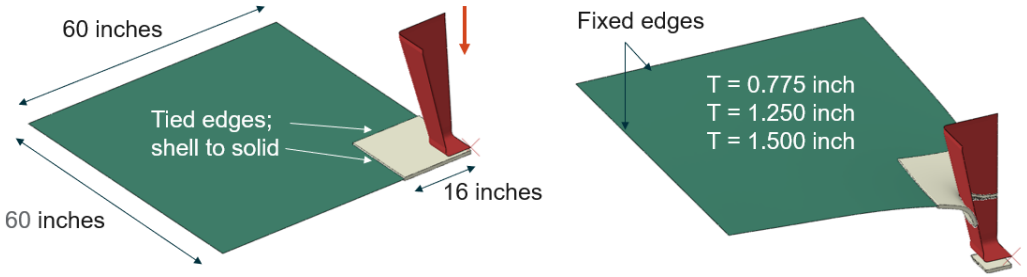

Figure 79. Overview of the Flat Plate Model

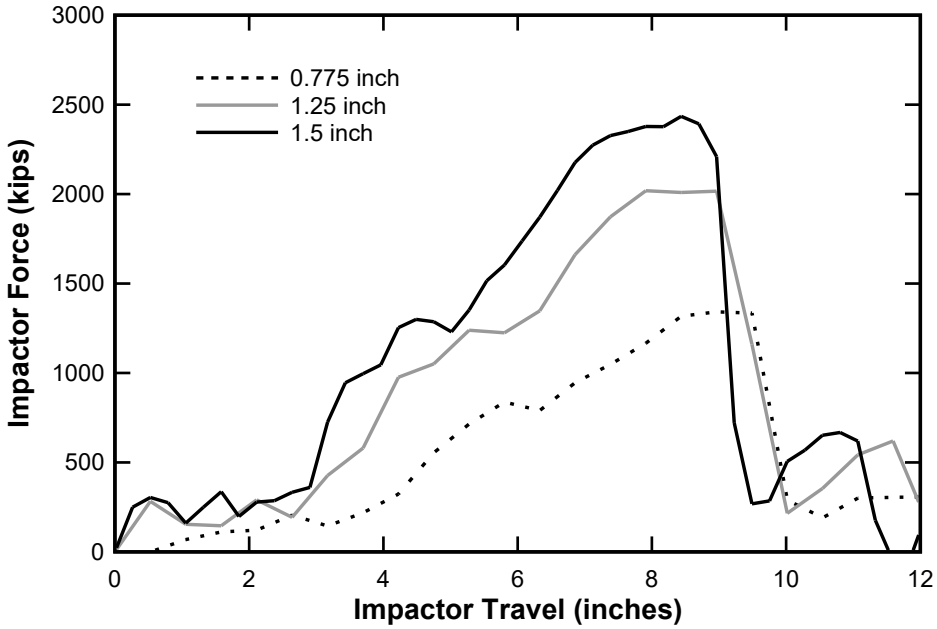

Figure 80. Force-displacement Curves, Single Flat Plates of Different Thickness

Table 23. Single Flat Plat Results Summary

Thickness	Displacement at Failure (in)	Energy Increase (%)	Force Increase (%)	Thickness Increase (%)
0.775	9.5	-	-	-
1.25	9.0	56	50	61
1.50	8.7	86	81	94

In a subsequent parametric study, the influence of splitting a monolithic steel plate into different layers was investigated by splitting the 1.5-inch-thick plate into the following three different configurations:

1. Two 0.75-inch-thick plates
2. One 1-inch-thick plate + one 0.5-inch-thick plate
3. Three 0.5-inch-thick plates

Researchers consider two different boundary condition configurations. In the first, the outer edges of all the plate layers were assigned fixed edge restraint, while in the second only the lowest plate was assigned fixed edge restraint, with the layered plates simply set loosely on top. An illustration of the three 0.5-inch-thick plate configuration with all fixed edge restraint is shown in Figure 81. For comparison, Figure 82 shows a cross-section through each configuration in the cases where only the bottom plate is fixed. In Figure 82, the indenter displacement is the same in all cases, with three of the four cases having punctured. The free movement of the upper layers is also visible.

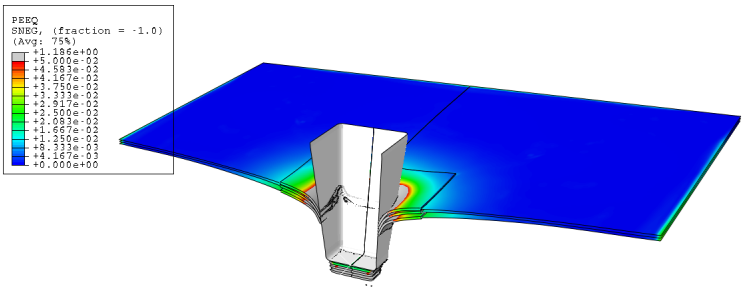

Figure 81. Plastic Strain Contour Plot of 3 0.5-inch-thick Plates with All Fixed Outer Edges

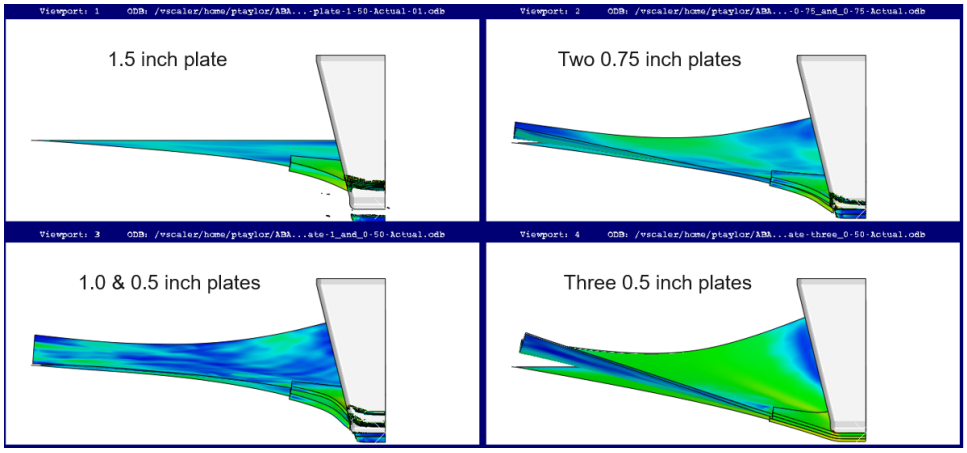

Figure 82. Overview of Free Edge Configurations vs. Monolithic 1.5-inch-thick Plate

The results are summarized in Table 24, where the displacement at peak force, peak force, and puncture energies have been compared against the baseline 1.5-inch-thick plate with fixed edge restraint. There is a clear distinction between the two boundary condition configurations, with the loose top plates improving the puncture resistance and the fixed layered plate configurations reducing it. The improvement in puncture energy resulting from splitting the plate in two is relatively modest (26 – 30 percent), while there appears to be significant benefit obtained by splitting the plate into three separate layers (231 percent improvement). The force-displacement curves for the loose upper plate configurations are shown in Figure 83, where the energy absorbed is a function of the area under the curves. There is relatively little change in peak force for the different configurations, but the three 0.5-inch-thick plate solution can accommodate a much greater displacement to failure, more than double that of the single 1.5-inch-thick plate.

Further investigation of multiple thinner layers using the Flat Plate Model was not undertaken for several reasons. First, the 0.5-inch-thick plate represents a reasonable minimum thickness for the tank shell. The calibrated element size of 0.085 inches also shows 6 elements through the thickness of a 0.5-inch-thick layer, which is sufficient to capture bending behavior correctly, although reducing the number of elements through-thickness further would begin to compromise accuracy. Finally, the performance gain of multiple layers was unproven on a more realistic tank car model.

Table 24. Layered Plate Results Summary

Configuration	Boundary Conditions	Displacement at Peak Force (in)	Peak Force (kips)	Force Change (%)	Energy Change (%)
Single 1.5 in	Fixed	8.44	2435	-	-
Two ¾ in	Loose upper plates	11.33	2444	+ 0.4	+30
1 & ½ in	Loose upper plates	10.28	2452	+ 0.7	+26
Three ½ in	Loose upper plates	17.40	2634	+ 8.2	+231
Two ¾ in	All plates fixed edges	7.91	2353	-3.3	-27
1 & ½ in	All plates fixed edges	7.65	2224	-8.7	-32
Three ½ in	All plates fixed edges	7.91	2270	-6.8	-29

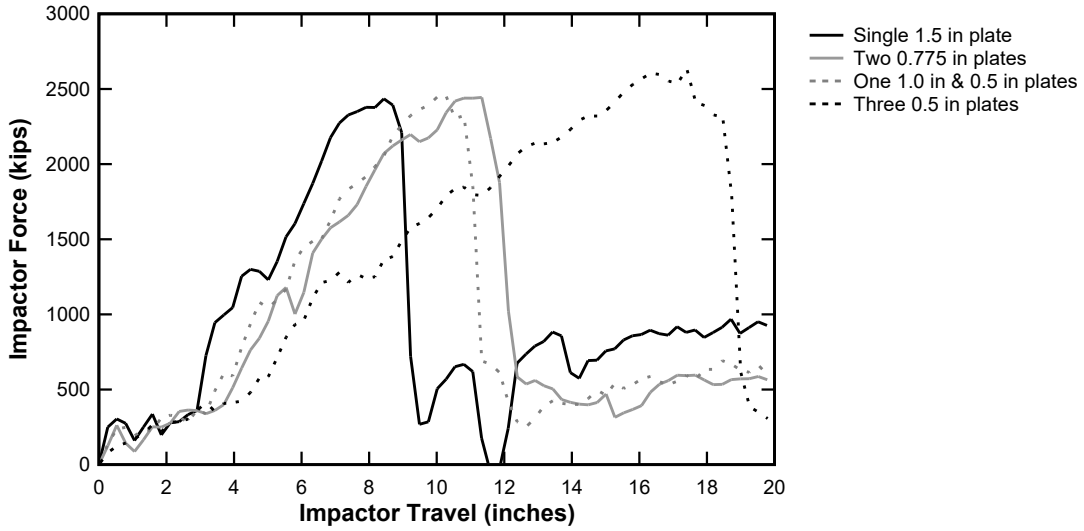

Figure 83. Force-displacement Curves, Loose Upper Plate Configurations vs. Single 1.5-inch-thick Plate

4.5.2.3 Layered Plate Quarter-Symmetry Tank Car Model

The results from the Punch Plate Model indicated a reduction in puncture performance by splitting plates into multiple layers, whereas results from the Flat Plate Model indicated a potentially significant benefit depending on the plate constraint conditions. Given this uncertainty, the layered plate solution was further investigated using the previously developed and validated quarter-symmetry tank car model. In this investigation, the 1.5-inch-thick shell model was used as a baseline against which various layered plate solutions were compared. In the first sensitivity, the most promising *layered* solution from the flat plate model (3 x 0.5-inch-thick plates) was assessed assuming all three plate layers were continuous (i.e., a-tank-within-a-tank-within-a-tank, Figure 84). This is most analogous to the flat plate model with fixed end restraints applied to all three layers and therefore the puncture performance of the tank was expected to reduce in this configuration.

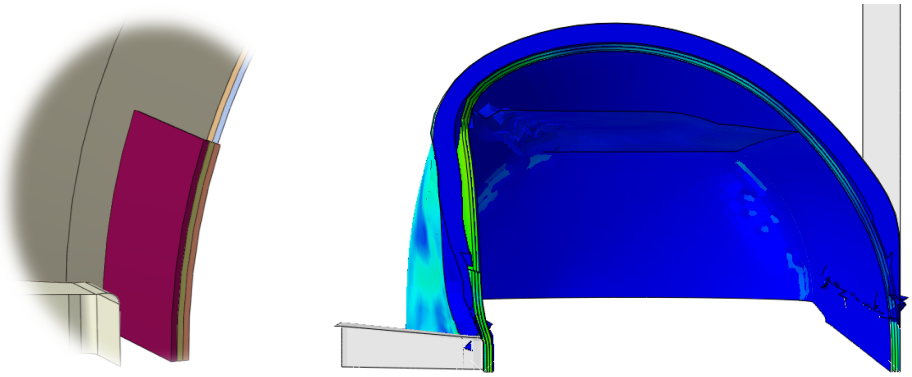

Figure 84. Illustration of Tank Shell Separated into Three Continuous but Separate Layers 0.5-inch-thick

The model was subjected to impact by a 12 x 12-inch indenter at a speed of 23.5 mph, the speed at which the monolithic 1.5-inch-thick shell was calculated to just fail. A comparison of the force-displacement response between the two models is shown in Figure 85. The overall response was largely as expected, with the layered shell exhibiting lower stiffness and undergoing a larger displacement to failure (48.4 vs 42.5 inches). The peak force of the layered shell reduced by 19.3 percent, as did the overall energy absorbed (i.e., 6 percent lower). These results supported the findings from the Flat Plate Model, where layering the plates and constraining the outer edges reduced the overall puncture resistance.

The team then conducted a parametric study in which the outer layers were split circumferentially to provide free edge restraint to assess if the benefit of providing free edge restraint observed in the Flat Plate Model would be carried through to the tank car model. The study considered three different plate thickness configurations, as shown in Table 25. In each case circumferential splits were implemented in the outer layers at different intervals (i.e., the outer layers we considered to be continuous rings with varying plate widths). In the FE model these rings were created by imposing physical breaks at distances 25, 50 and 75 inches from the centerline (Figure 86). Accounting for the quarter-symmetry modelling technique, this resulted in central rings with widths of 50, 100, and 150 inches. The 12 x 12-inch indenter was used in all cases and the speed adjusted in 1 mph increments until the survival speed of the tank was determined. The results are summarized in Table 25.

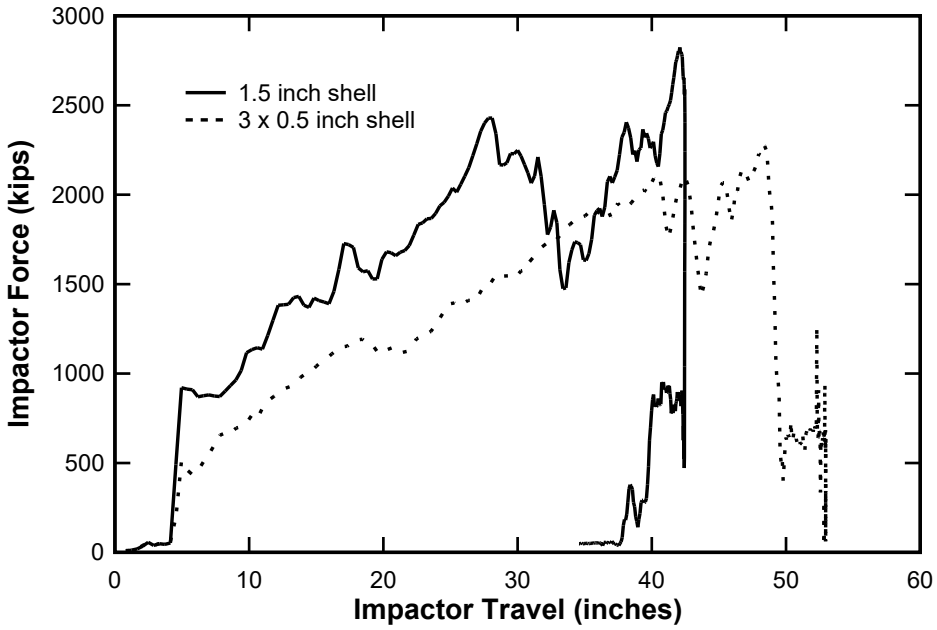

Figure 85. Force-displacement Curves 23.5mph, 3 x 0.5-inch Continuous Shells vs. Single 1.5-inch-thick Shell

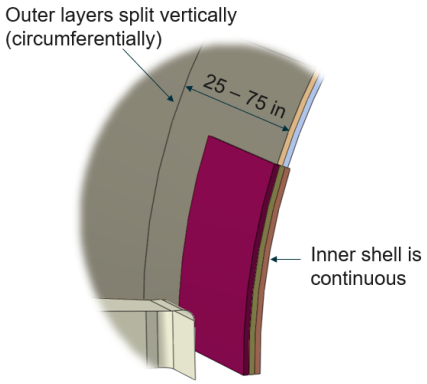

Figure 86. Overview of Implementation of Vertical Splits

Table 25. Layered-Split Plate Results Summary

#	Shell Thickness (in)	Additional Steel Layers	Outer Plate(s) Width (in)	Survival Speed (mph)
1	1.50	-	-	23
2	0.50	2 x 0.5 in	50	23
3	0.50	2 x 0.5 in	100	21
4	0.50	2 x 0.5 in	150	21
5	0.775	0.725 in	50	23
6	0.775	0.725 in	100	< 23
7	0.775	0.725 in	150	< 23
8	1.0	0.5 in	50	21
9	1.0	0.5 in	100	21
10	1.0	0.5 in	150	21

The results in Table 25 show that the calculated survival speed of two configurations (Cases 2 and 5) matched the survival speed of the single 1.5-inch-thick shell but none of the configurations resulted in improved puncture resistance.

The results also show a clear correlation between vertical split plate width and puncture resistance, with wider plates having reduced resistance. Figure 87 shows an overview of the 3-plate solution (Cases 2, 3, and 4) at time 200ms, approximately the time of peak indenter travel when subjected to a 21-mph impact. In Figure 87, the outer jacket and foam layers have been removed from the images to show the response of the outer plate layers when different split widths have been implemented. The difference in response of the 50-inch-wide plate between the others is apparent. At 50-inches-wide, the longitudinal constraint is low and because of this the outer plate can accommodate greater deformation and withstand puncture for longer. This in turn delays puncture of the tank shell, enabling more energy to be absorbed over the course of the impact.

In each of the layered-split plate cases examined, failure of the outer plate preceded failure of the tank shell. This is illustrated in Figure 88, where failure of the outer 0.5-inch-thick plate precedes failure of the 1.0-inch-thick shell. Therefore, implementing measures that would improve the resistance of the outer layer to puncture, such as using stronger or more ductile steel, would result in improved puncture resistance.

In summary, splitting the tank shell into multiple layers of thinner plates of equivalent overall thickness did not show an improved puncture resistance as predicted by the Flat Plate Model. Nevertheless, the results showed that similar or equal puncture resistance could be obtained with multiple different plate combinations. Finally, these findings assume that ductility and strength remain constant across the different plate thicknesses. This assumption has been investigated in detail in Section 5 of this report.

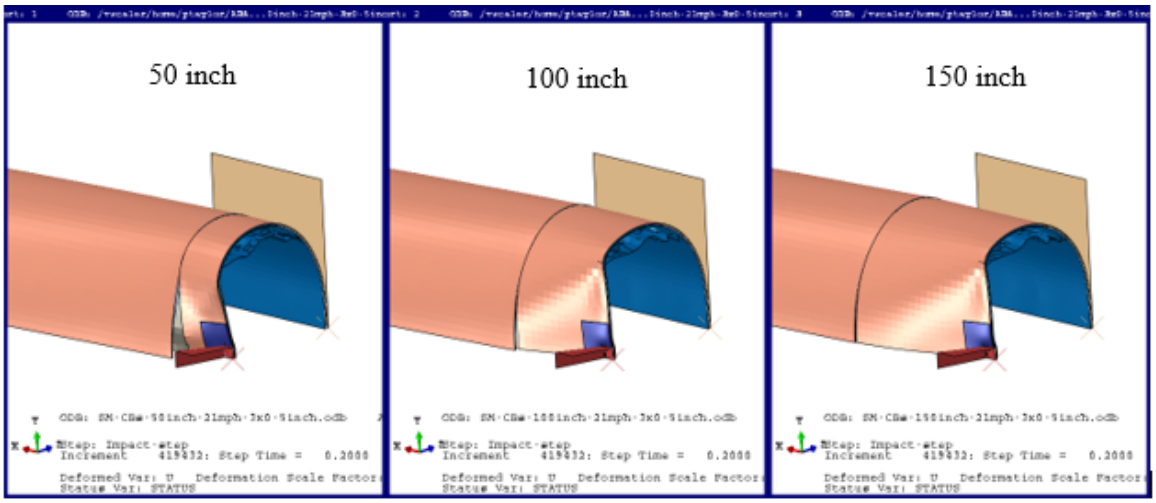

Figure 87. Response of Layered-split Plate Case #2 at Time 200ms (Jacket and Foam Removed for Clarity)

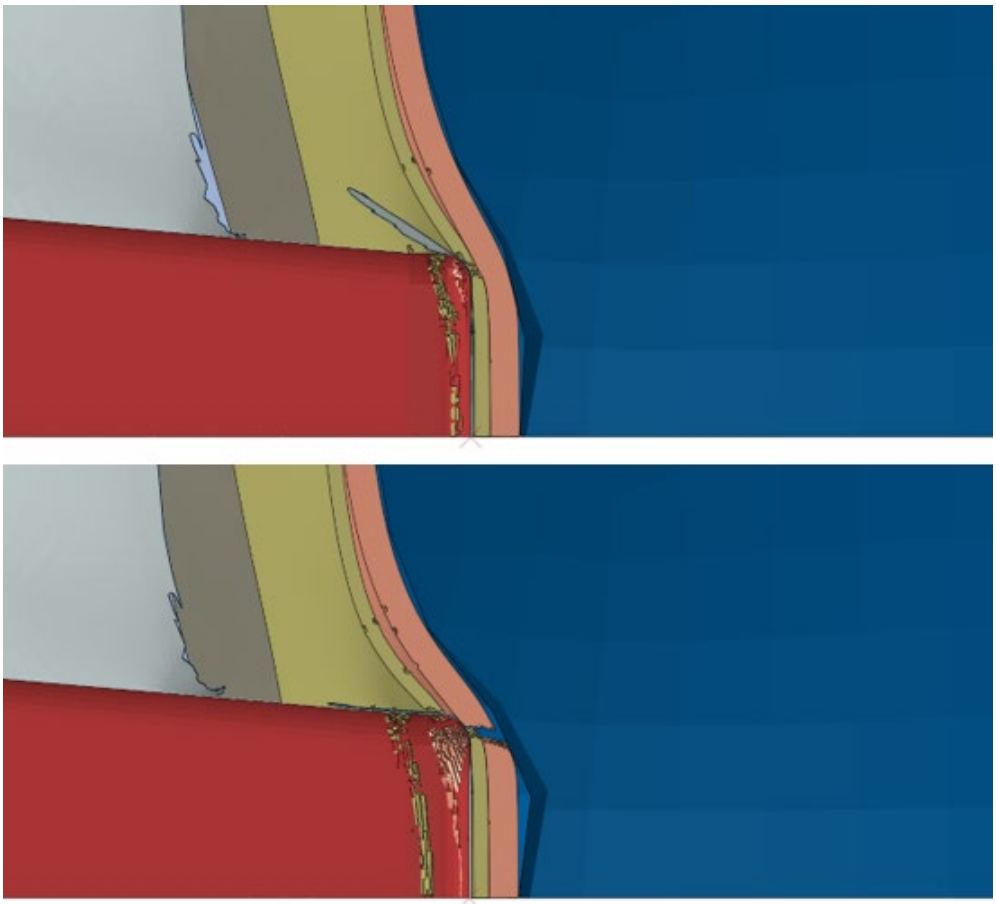

Figure 88. Failure of 0.5-inch-thick Outer Layer (top) Preceding Failure of 1.0-inch-thick Shell (bottom)

4.5.3 Strengthened Jacket Solution

The tank-within-a-tank solution, in which the outer jacket of the tank is strengthened by increasing its thickness and/or using stronger or more ductile metals, was considered by ATCCRP to provide the most promising solution for enhancing the puncture resistance of tank cars. This conclusion had been reached following a comprehensive review of mitigation solutions but had not been proven by testing.

The quarter-symmetry models developed in support of this research had demonstrated very good agreement with physical tests. These models were therefore used to assess the strengthened jacket solution using validated material models for both the shell and jacket. The different configurations investigated are shown in Table 26, with both the jacket and tank shell modelled using Actual TC128-B material. Both continuous and split outer jackets were considered as part of the study. The thicker jackets were modelled using the same centerline as the original A1011 jackets, with the thickness of the foam insulation reduced slightly to account for the slightly thicker jacket. This was not considered to have any significant bearing on the results given the limited role the foam layer plays in determining puncture resistance.

Table 26. Strengthened Jacket Solution Configurations

#	Shell Thickness (in)	Jacket Thickness (in)	Jacket Plate Width (in)	Impact Location
1	0.775	0.725	Continuous	-
2a	0.775	0.725	50	Middle of plate
2b	0.775	0.725	50	At plate boundary
3	0.775	0.725	100	Middle of plate
4	0.775	0.5	50	Middle of plate
5	1.0	0.5	50	Middle of plate

An overview of the model is shown in Figure 89 showing Configuration #2a. The arrow in Figure 89 identifies the location of the circumferential break, in this case 25 inches from the centerline. In Configuration #2b, the impact has been considered at the location where two plates are split, assuming the plates are free and there is no physical restraint between them. Figure 90 and Figure 91 compare these two configurations. These sensitivities were undertaken to determine if the location of the impact affects the performance, with impact centered at a plate boundary considered likely to represent the worst-case location for the side impact condition due to the perceived potential for the indenter to separate and therefore bypass the jacket plates.

Figure 90 and Figure 91 show full representations of the tank to illustrate the different impact locations only. All analyses were conducted using quarter-symmetry techniques.

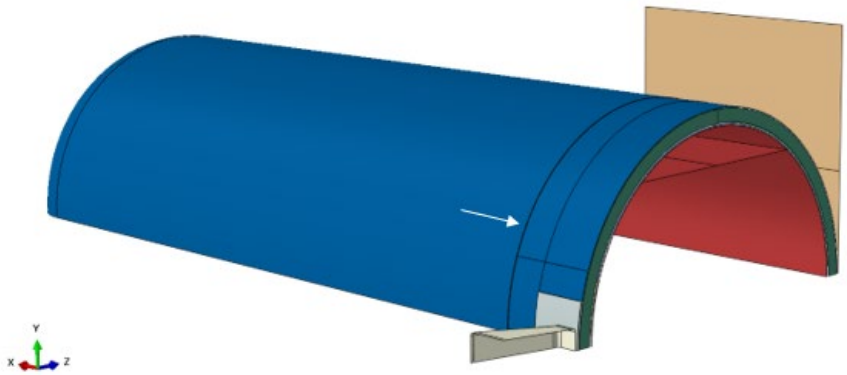

Figure 89. Overview of Quarter Symmetry Tank Car Model with Strengthened Jacket (Configuration #2a); Arrow Shows Location of the Circumferential Split

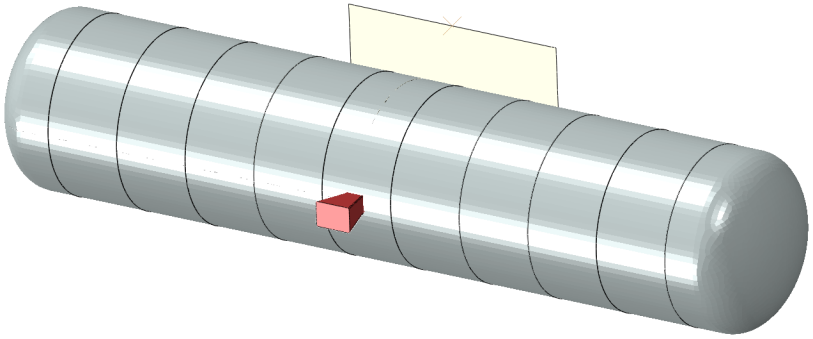

Figure 90. Configuration #2a – Indenter Striking Center of 50-inch-wide Split Plate Jacket

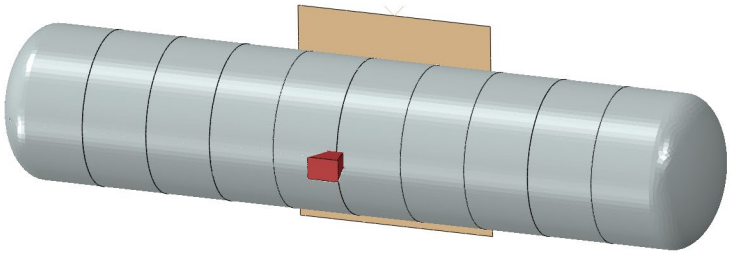

Figure 91. Configuration #2b – Indenter Striking at Center of Plate Boundary (No Restraint Between Adjacent Plates)

Another important feature of the models is that within the vicinity of the indenter, the jacket has been modelled using solid elements using the same element length and formulation as the tank shell. This is shown in Figure 92, in which the solid element region of the jacket measures 15 x 15-inches. The solid element region is connected to the shell element jacket using the same local mesh refinement and tie constraint technique as adopted in the previously validated tank shell models. As per previous parametric studies, the indenter speed was adjusted in 1 mph increments to determine the survival speed. The results are summarized in Table 27.

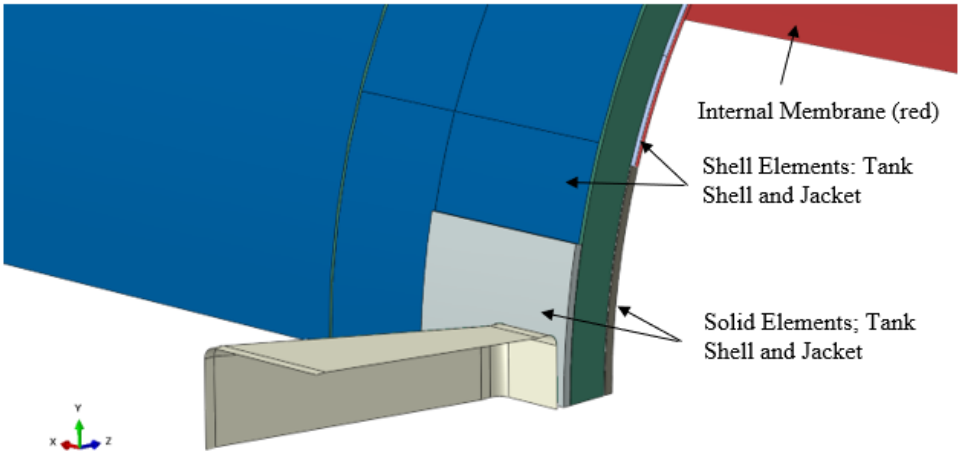

Figure 92. Overview of Puncture Zone Featuring Solid Element Representation of Both Jacket and Tank Shell

Table 27. Strengthened Jacket Configurations - Results

#	Shell Thickness (in)	Jacket Thickness (in)	Jacket Plate Width (in)	Impact Location	Survival Speed (mph)
1	0.775	0.725	Continuous	-	22
2a	0.775	0.725	50	Middle of plate	24
2b	0.775	0.725	50	At plate boundary	23
3	0.775	0.725	100	Middle of plate	23
4	0.775	0.5	50	Middle of plate	22
5	1.0	0.5	50	Middle of plate	23

The results showed that implementing a continuous 0.725-inch-thick jacket using Actual TC128-B material improved the side-impact puncture resistance by 9 mph, which equates to a 186 percent increase in puncture energy. An overview of this case is shown in Figure 93. In the cases

where the 0.725-inch-thick jacket was split at 50-inch intervals, the puncture resistance improved further, to 24 mph if the indenter strikes the center of the plate and 23 mph if it strikes a plate boundary. When the 0.725-inch jacket plate width was increased to 100 inches the effectiveness of splitting the jacket was reduced. This is shown in Figure 94 where Configuration #2a survives and #3 fails at 24 mph.

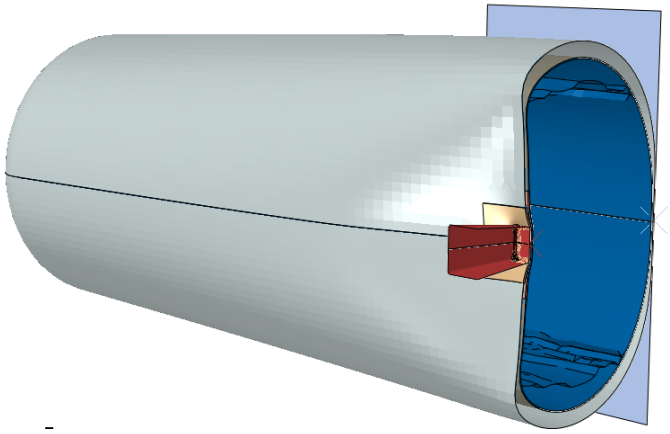

Figure 93. Overview of Configuration #1 – Continuous Outer Jacket

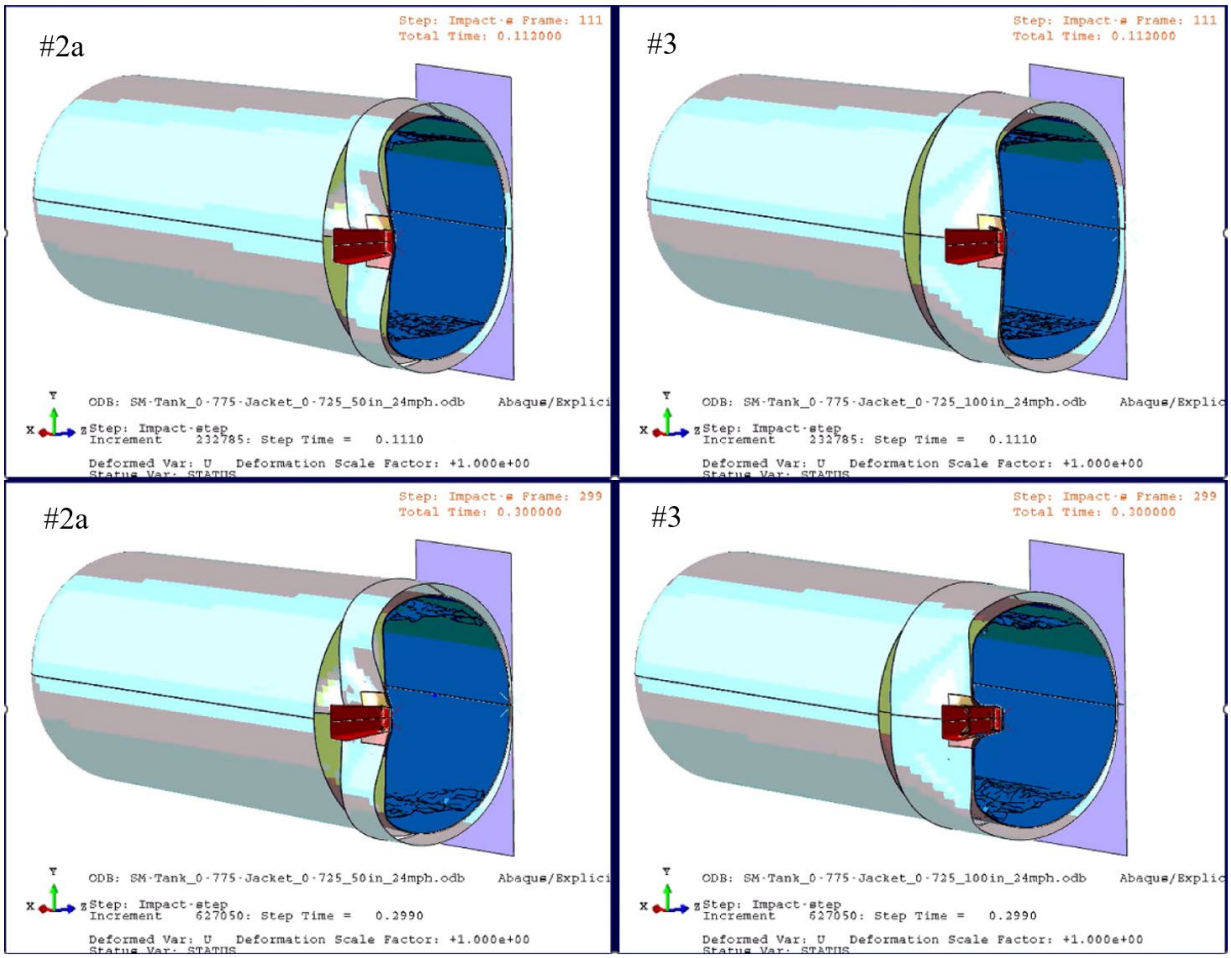

Figure 94. Response of Configurations #2a and #3 at 24 mph

Configurations #4 and #5 considered a 0.5-inch-thick jacket protecting 0.775- and 1.0-inch-thick shells. The puncture resistance was not significantly different in either case (22 and 23 mph), which is notable in that increasing the shell thickness from 0.775 to 1.0 inches resulted in only 1 mph increase in resistance.

4.5.4 Summary

The sub models used to assess the puncture resistance of multiple layered plates indicated conflicting results. The local punch model showed that puncture resistance is reduced if a single thick plate is split into multiple layers of thinner plate, whereas the flat plate model indicated that significant improvement could be obtained provided the right boundary conditions are adopted. Analyses of this solution using a validated quarter-symmetry tank car model indicated that the puncture resistance of multiple layers of plate was approximately equal to that of a single thick plate, with the boundary conditions of the outer plate layers again influencing the response. Finally, the strengthened jacket solution was investigated and again showed puncture resistance that was comparable to using a tank shell of equivalent thickness (1.5 inches).

One of the key findings from these analyses was that if using a multiple plate solution, the constraint applied to the outer layers of plate (i.e., jacket) influences the puncture resistance. It was found from the quarter-symmetry tank car analyses that implementing circumferential breaks in the outer plates can slightly improve puncture resistance versus using monolithic plates. However, the benefit was found to be relatively small (i.e., 1 – 2 mph improvement) and was tested on a relatively small set of side impact scenarios.

The comparison of puncture resistance between a single thick plate and multiple plates of equivalent overall thickness was undertaken on the assumption that ductility remained the same across the different plate thicknesses. The influence of ductility on puncture resistance was examined in Section 4.4.3 and was a feature of the Enhanced TC128-B material where it was shown that improving ductility, even at the cost of reducing strength, was found to improve puncture resistance. The assumption of constant ductility at increased shell thickness is therefore a key feature in the response of the thicker shells. For example, if ductility were to reduce with increasing shell thickness, then adopting a multi-plate solution could have greater benefit, particularly as multi-plate solutions offer the potential to use different higher strength or higher ductility materials in the outer layers. An investigation of the relationship between ductility and plate thickness was therefore undertaken and is discussed in Section 5.

4.6 Mitigation – Elastomeric Liners

4.6.1 Internal Containment Liner

An alternative mitigation concept not considered previously is the possible use of internal liners to prevent hazmat release in the event of puncture. Such liners have the potential to provide an additional ‘line of defense’ against hazmat release in cases where puncture occurred but with limited extent. The coupled action of the structural mitigation strategies discussed previously with internal liners could provide an additional benefit resulting in reduction of the conditional probability of release.

Research partner TT has been involved in previous projects in which an elastomer (i.e., polyurea) has been implemented to improve the blast resistance of concrete structures. In one such project, constitutive material models of polyurea were developed for use in FE simulations

and validated against experimental data. The engineering stress-strain curves for both are shown in Figure 95, where 'Data fit' represents the test data and 'PLIH' a von Mises[5] plasticity with piecewise linear hardening model. The results show that the polyurea has a high elongation with an engineering strain-to-failure of approximately 5.

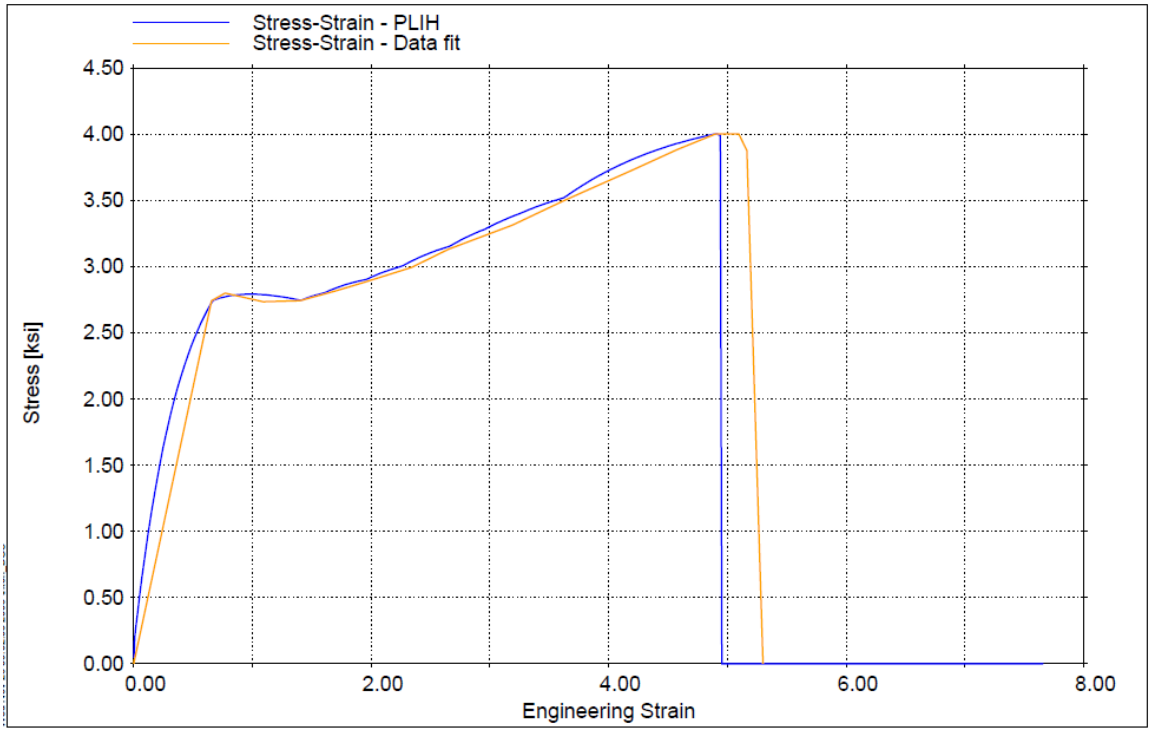

Figure 95. Experimental and Simulated Engineering Stress-strain Curves for Polyurea

A material model for polyurea (shown in Figure 95) was developed for use in Abaqus, with the process described in Appendix D. A single element test using the Abaqus material model was undertaken for verification purposes, with the resulting stress-strain curve comparing well against the experimental data (Figure 146).

To assess the potential effectiveness of the internal liner solution, a 0.25-inch-thick layer of polyurea was implemented in the validated Test 6 baseline quarter-symmetry tank car model (i.e., 0.775-inch-thick shell with 12 x 12-inch indenter and no other structural modifications). The liner was implemented as a discrete part, positioned between the tank shell and the fluid membrane, as illustrated in Figure 96. The liner was modelled using shell elements with a typical element length of 2 inches resulting in 11,111 elements within the quarter-symmetric part (Figure 97). The general contact algorithm available within Abaqus was used with hard contact and a tangential coefficient of friction of 0.3 assigned. This means that the liner can move relative to the tank shell and the fluid membrane, but with a frictional penalty. This is somewhat different to a spray-applied liner where there would be some adhesion between the liner and the tank shell. The only other modification made to the model was to reduce the diameter of the fluid membrane by 0.5 inch to facilitate implementation of the liner.

[5] A von Mises stress is a value used to determine if a given material will yield or fracture. It is mostly used for ductile materials, such as metals.

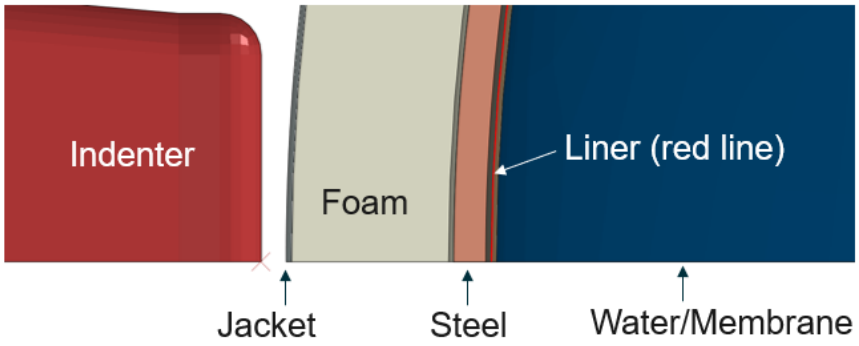

Figure 96. Local Cross-section through FE Model Showing Location of Liner

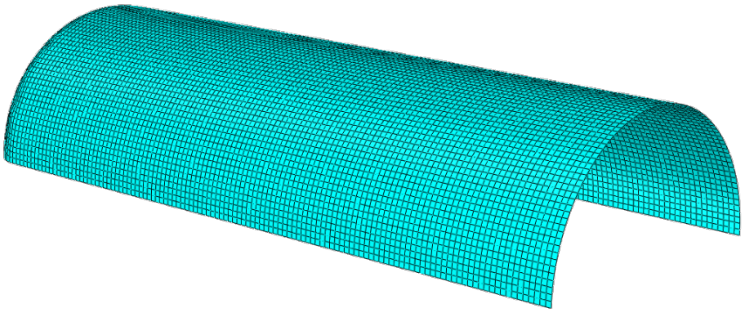

Figure 97. Internal Liner with Mesh Shown

The team conducted simulations at indenter speeds of 15 and 16 mph (i.e., speeds just greater than the puncture speed of the baseline model). In both cases the tank shell punctured, but the integrity of the liner remained intact showing that it was effective at preventing hazmat release. In the 15-mph case there was little change to the overall performance of the tank, with the indenter travelling to a depth of 38.7 inches and stopping. This is the same peak depth reached in the baseline 15-mph case with no liner. An overview of the response of the model is shown in Figure 98, where the left image shows the overall behavior, and the right image shows a plastic strain contour plot of the liner at the end of the simulation. The peak plastic strain reached in the liner is approximately 0.77, which coincidentally is approximately 77 percent of the failure strain. This behavior is further illustrated in Figure 99.

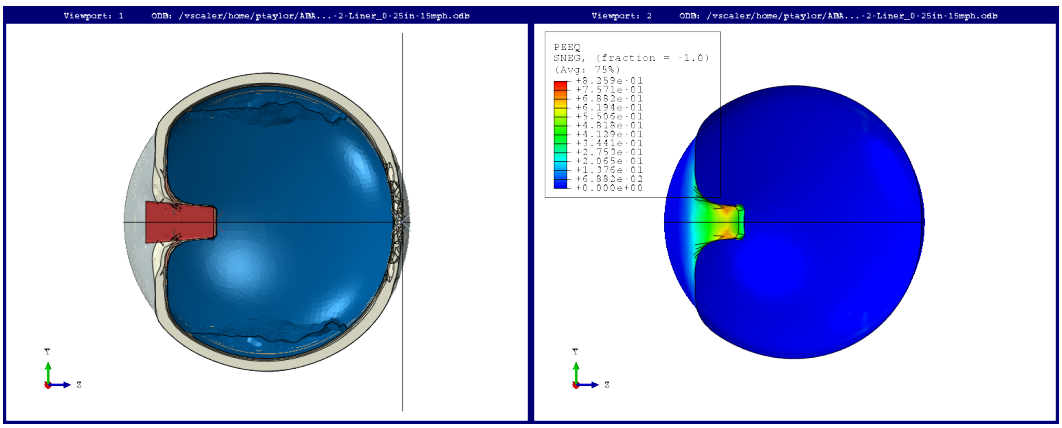

Figure 98. Response of Liner Model to 15-mph Impact (Right Image Shows Plastic Strain)

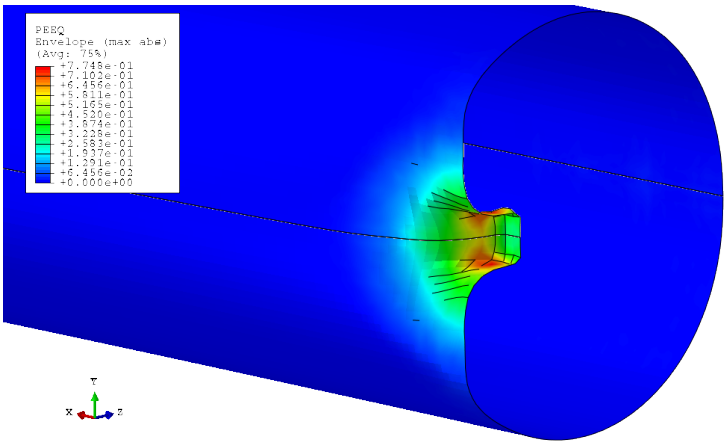

Figure 99. Plastic Strain Contour Plot Showing Response of Liner to 15-mph Impact

When the indenter speed was increased to 16 mph the indenter travel increased to 42 inches (+3.3 inches). This in turn increased the demand on the liner, with peak plastic strains found to reach 0.924, which is close to the limiting plastic strain. Given the high plastic strains observed it was concluded that any subsequent increase in indenter speed would likely result in failure of the liner, particularly as the mesh used for the liner was relatively coarse (2-inch element size) and mesh refinement may lead to locally higher plastic strains.

To consider potential variation in liner material properties, the plastic strain-to-failure of the liner material was reduced by approximately 50 percent and set to 0.5. The 16-mph simulation was repeated using the less ductile liner material with failure of the liner observed to occur at an indenter travel of 40 inches. Figure 100 compares the response of the liner in the 16-mph case where the liner has the original and reduced ductility material properties. In the reduced ductility case, failure of the liner is evident with element deletion occurring. For this type of liner solution to be effective a material with high elongation to failure is required.

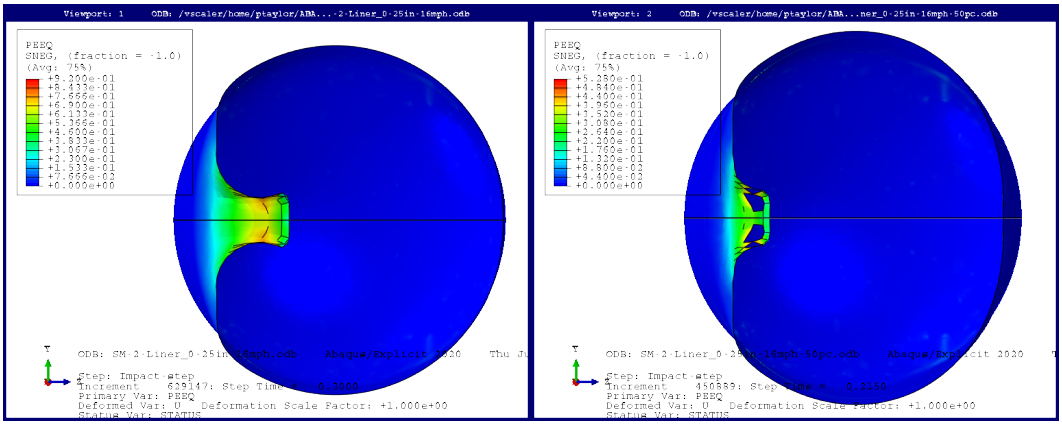

Figure 100. Plastic Strain Response of Liner in 16-mph Scenario: left – Polyurea Material, right – Reduced Ductility Polyurea

4.6.2 Metal-Elastomer Bilayers

In the analyses described above, the elastomeric liner was considered separate to the tank shell (i.e., no adhesion between the two components). The liner in that scenario was a ‘bag-type’ liner that would not be expected to, nor was it found to, increase the puncture resistance of the shell.

However, there are situations in which an elastomer layer bonded to a metal plate (i.e., metal-elastomer bilayer) can improve the energy absorption behavior versus an all-metal plate of equivalent mass. This topic was investigated numerically and experimentally by the US Navy in relation to underwater shock loading of steel plates, and subsequently by Xue and Hutchinson, [42].

Xue and Hutchinson found that if the ratio of the elastomer modulus to metal yield stress is sufficiently large, then the energy absorption characteristics of the bilayer can exceed that of an all-metal plate having the same mass/area despite a reduction in strength. The energy absorption improvement of the bilayer is a consequence of the elastomer layer delaying necking in the steel plate. Xue and Hutchinson considered quasi-static and dynamic biaxial stretching of round steel plate in their investigation. With regards to quasi-static loading, which is most applicable to the tank car puncture scenario, they concluded the following:

Under quasi-static loading, bilayers comprised of an elastomer layer bonded to a ductile metal layer can undergo appreciably greater stretch prior to necking than an all-metal plate if the stiffness/strength parameter satisfies:

$$S = h_0^e E/(h_0^m \sigma_R) \geq 0.1$$

Where: h_0^e: elastomer thickness

h_0^m: metal thickness

E: elastomer modulus elasticity

σ_R: yield stress of the metal

Implementing the parameters for the liner considered in the previous section (i.e., a 0.25-inch-thick liner bonded to a 0.775-inch-thick plate) with E = 4.2 ksi and σ_R = 71.5 ksi, gives S = 0.019. This is less than 0.1, indicating that with this arrangement the bilayer would not be expected to yield an improvement in energy absorption through delayed necking. To achieve S = 0.1 the elastomer layer would need to be 1.33 inches thick.

To verify these findings a series of single element tests were performed with the three configurations considered shown in Table 28. Simple uniaxial tensile tests were undertaken on 2 x 2-inch, four-node, full integration shell and composite shell elements. The Actual TC128-B material derived for the tank car was assigned to the metal plate, and the polyurea material assigned to the elastomer layer.

Table 28. Single Element Test Configurations

Test #	Metal Thickness (in)	Elastomer Thickness (in)	Element Type
1	0.775	-	Shell
2	0.775	0.25	Composite Shell
3	0.775	1.33	Composite Shell

The force-displacement curves extracted from each configuration are shown in Figure 101. As predicted by the calculation above, there is little observable benefit from the 0.25-inch-thick layer, with the 1.33-inch-thick layer resulting in a relatively small improvement. A higher

modulus elastomer would yield an improved response, although this has not been investigated and there would therefore likely be a reduction in elongation.

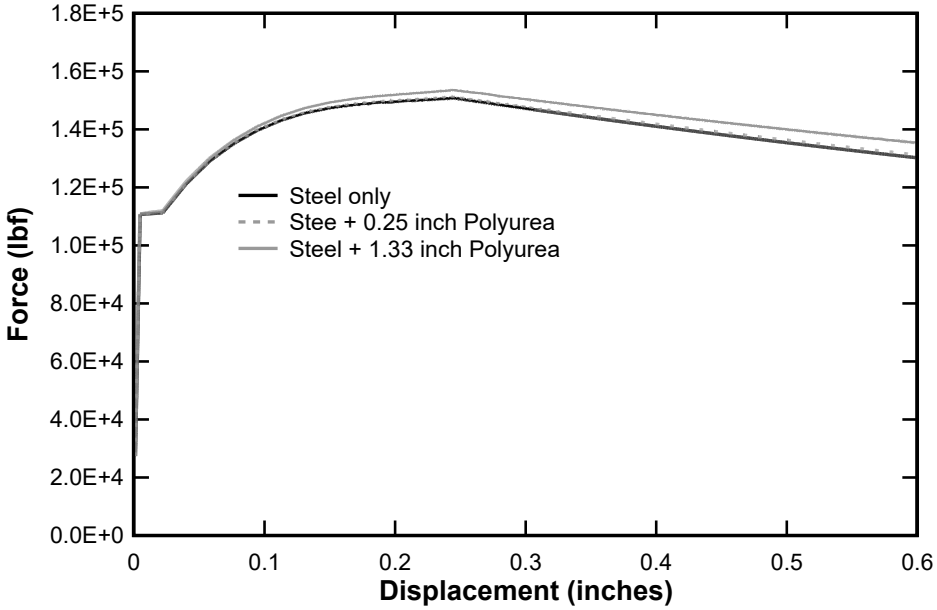

Figure 101. Force-displacement Curves, Steel-elastomer Bilayer Single Element Tensile Tests

In mass terms, a 1.33-inch-thick layer of polyurea has an equivalent metal plate thickness of approximately 0.21 inches. As seen in previous investigation of shell thickness, increasing the shell thickness from 0.775 inches to 0.985 inches would result in a significant improvement in puncture resistance.

4.6.3 Elastomeric Liner Summary

Researchers investigated two types of elastomeric liner: one aimed at providing a secondary containment mechanism in cases where the shell just punctures, and another aimed at improving the puncture resistance of the tank shell. The two types have very different desired material properties, with the containment-type liner requiring large elongation and the bilayer-type liner requiring a combination of stiffness and elongation. The polyurea layer considered in this study was more suited to the former application, with tank car simulations demonstrating that in the side impact case the liner could be effective at containing hazmat at impact speeds in the region of 1 to 2 mph greater than the puncture speed. The same polyurea material used as the elastomeric component of a bilayer with TC128-B indicated little benefit, particularly when compared against an all-metal plate of equivalent mass/area. In these calculations the elastomer component has been assessed based on its ability to delay necking in the steel.

4.7 Mitigation – Blunting

The indenter shape and size are known from various previous studies to strongly influence the puncture resistance of tank cars. The standard 6 x 6- and 12 x 12-inch indenters used with side and head impact tests are notionally considered to represent a broken rail and a car coupler, respectively. Puncture speeds for both indenter sizes have been determined in this research effort

making use of the validated FE models. To investigate the potential effectiveness of blunting mitigation solutions, an additional set of simulations were undertaken to determine the survival speed of the baseline tank car when subjected to impact by a 24 x 24-inch indenter. The indenter was modelled with a 2-inch corner radius and the quarter-symmetry model was used for these simulations. Figure 102 illustrates the response of the model to a 22-mph impact.

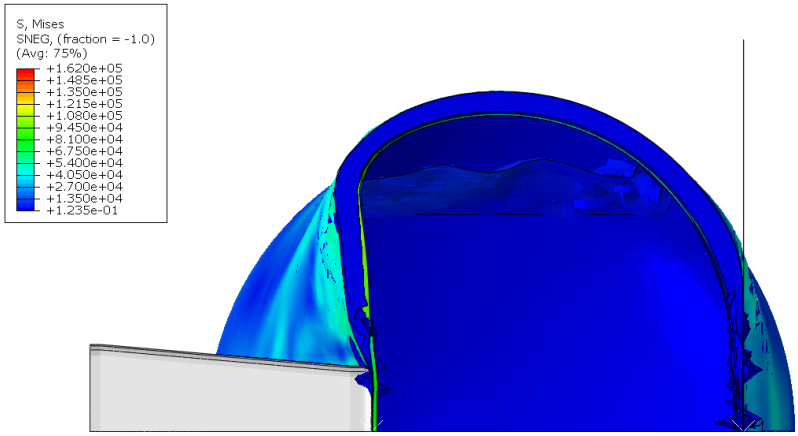

Figure 102. Illustration of Impact by 24 x 24-inch Indenter

The calculated survival speeds and associated impact energies for each indenter size are summarized in Table 29. The results illustrate the effectiveness of blunting, with a 24-inch indenter showing approximately the same puncture resistance as increasing the tank shell thickness to 1.5 inches. This assumes that the indenter shape is square, which imposes high local stresses at the indenter corners and ultimately results in failure of the tank shell in shear. A blunting solution that creates a more uniform (e.g., circular) load on the shell would likely be more effective as it would reduce the local shear demand.

Table 29. Survival Speeds for Different Indenter Sizes

Indenter Size (in)	Survival Speed (mph)	Impact Energy (million-ft-lb)
6 x 6	8.0	0.636
12 x 12	13.0	1.679
24 x 24	22.0	5.255

To achieve a blunting area equivalent to that imposed by a 24-inch indenter when impacted by a 12-inch indenter, the 4-inch-wide void space currently occupied by foam insulation would need to be increased and the foam replaced by a much more robust and stiffer material. This is illustrated in Figure 103, which shows both the 12- and 24-inch indenters positioned adjacent to the tank. The required increase in space between the tank shell and jacket would depend on the chosen material/solution, but any solution implemented within that space would almost certainly have a much higher mass per area than the current, lightweight foam material. The new material would also have to provide an equivalent thermal resistance to the foam. This being the case, it is unlikely that any solution implemented with the specific role of blunting impact loads would be any more efficient than simply increasing the shell or jacket thickness.

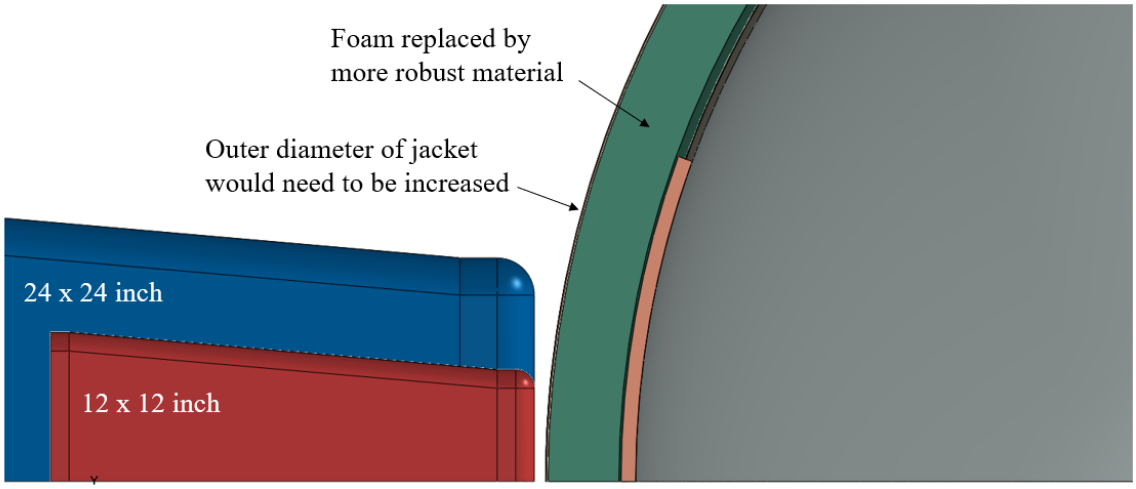

Figure 103. Overview of Side Impact Arrangement with 12 x 12-inch (red) and 24 x 24-inch (blue) Indenters

5. Investigation of the Relationship between Plate Thickness and Ductility

Investigation of the relationship between tank shell thickness and puncture resistance showed a strong correlation between the two. Subsequent investigation of multiple layered and offset plate solutions, in which the total plate thickness was the same as a thick (i.e., 1.5-inch-thick) shell, showed that similar magnitudes of puncture resistance could be attained in various configurations. However, these findings assumed that material ductility remains constant across different plate thicknesses. If, as suspected, ductility is adversely affected by increasing plate thickness, then the puncture resistance of a single thick shell may be overestimated, and similarly the resistance provided by multiple layers of thinner plate underestimated. The research team investigated this topic as part of the research effort, building on recent work published by Anderson et al. [43] which investigated the fundamental differences between plane strain bending and far-field plane strain tension in ductile plate failure.

Anderson et al. [43] employed the micro-mechanics-based Gurson-Tvergaard-Needleman (GTN) model to investigate the underlying mechanics behind differences observed in fracture strain of thin metal plates; it was previously experimentally observed to be significantly higher in plane strain bending than in far-field plane strain tension. In that research, a 1.4-mm-thick plate was considered in the bending and tension cases; the absence of thinning in the plane strain bending condition was identified as one of the key factors behind lower void growth rate and therefore greater strain to failure in that case. The results published for the 1.4-mm-thick plate were used in the current research as baseline data against which FE models were developed and verified. Thicker plates, such as those used in tank car construction were then investigated by modifying the FE models to determine how the relationship changes with increasing plate thickness. The methodology and results from this study are described in the following sections.

5.1 Gurson-Tvergaard-Needleman (GTN) Model

The GTN model is a micro-mechanics-based material model that is well suited for capturing the complexity of the plate fracture process, accounting for crack initiation where voids grow and coalesce to micro-crack formation, as well as stress triaxiality dependence. The model operates on the basis that individual elements are of a similar size to the distance between microvoids within the metal, with the damage parameters calibrated for a specific element size. A change in element size would therefore require redefining the damage parameters. Anderson et al. [43] used an element size L_e = t/128, where t is the plate thickness (i.e., 1.4 mm). This gives an element size of 0.01094 mm, resulting in 33,603 elements within a simple 1.4 x 10.0 mm 2-dimensional plate. Therefore, this model, while well-suited for investigation of highly localized failures in small samples, would not be well-suited for use in large tank car simulations due to the significant scale increase. The number of elements required within the puncture zone would simply be too large.

5.2 Verification of Plane Strain Tension and Bending Models

In the first step in this investigation, the team reproduced the plane strain tension and plane strain bending simulations published in [43]. Following this initial verification, the models were modified to investigate the response of thicker plates.

5.2.1 Far Field Plane Strain Tension Case

An overview of the double-edge notch tension (DENT) test used to investigate far-field plane strain tension is shown in Figure 104. The ligament at the center of the specimen approximates a plane strain condition (i.e., strain in the x-direction = 0). This can be represented using a 2D model with plane strain conditions, where plate thickness, t, is 1.4 mm and plate length, L, is 10 mm. This gives a length to thickness ratio $L/t = 7.1$, which is sufficiently large to capture through-thickness necking, shear localization, and fracture related to ductile tearing.

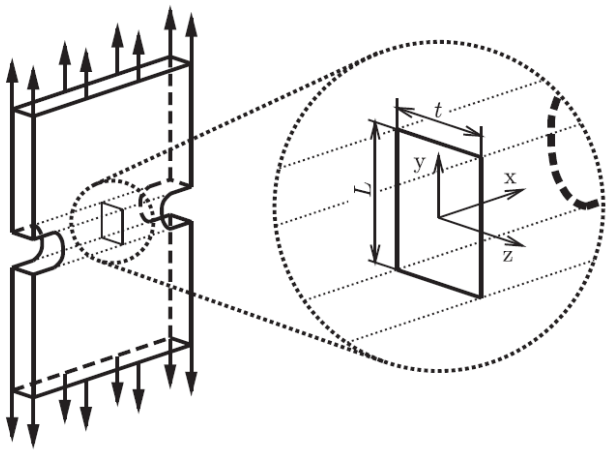

Figure 104. Far-field Plane Strain Test Setup – Only the Highlighted 2D Region with Length, *L*, and Thickness, *t*, Considered in Numerical Simulations [43]

An overview of the FE model researchers developed is shown in Figure 105, with the material parameters summarized in Table 30. Across the central portion of the model, with gauge length $2t = 2.8$ mm, the element length was fixed at 0.01094 mm using an enforced partitioning strategy. Outside of the gauge region the mesh was coarsened off for computational efficiency. At the top and bottom of the specimen an adjustment was made to the material model to reduce the initial void volume fraction, f_0, from 0.02 to 0.018 to avoid potential localization at the ends of the specimen where the boundary conditions were applied. Similarly, a single element located at the edge of the specimen at a 45-degree angle from center was assigned a material model with the same parameters as those shown in Table 30, but with a 10 percent reduction in the elastic modulus to promote localization at the center of the specimen. This element location is denoted by the arrowed 'X' in Figure 105.

The upper and lower edges of the specimen were simultaneously pulled to load the specimen in tension. A node at the center of the upper and lower edges was also fixed in the x-direction. Four-node bilinear plane strain elements with reduced integration (CPE4R) were assigned throughout and the Abaqus Explicit dynamic solver was used (with double precision on), to quasi-statically load the specimen. Plastic strain contour plots of the specimen undergoing through-thickness necking and failure are shown in Figure 106 and Figure 107. The force-displacement response of the specimen was extracted and normalized with respect to both the yield stress and the original length. This curve is compared to that produced by Anderson et al. [43] in Figure 108 with good agreement observed.

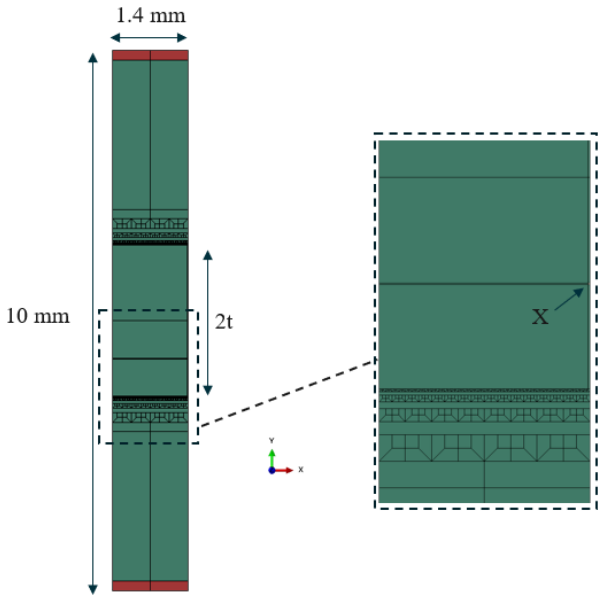

Figure 105. Overview of 1.4 mm Plane Strain Tension FE Model

Table 30. GTN Material Model Parameters

Parameter	Notation	Value
Density	ρ	7,850 kg/m^3
Young's Modulus	E	210 GPa
Poisson's Ratio	v	0.3
Yield Stress	σ_0	630 MPa
Strain hardening exponent	N	0.05
Gurson fitting parameters	q_1, q_2, q_3	1.5, 1.0, 2.25
Initial void volume fraction	f_0	0.02
Critical void volume fraction	f_C	0.15
Final void volume fraction	f_F	0.25

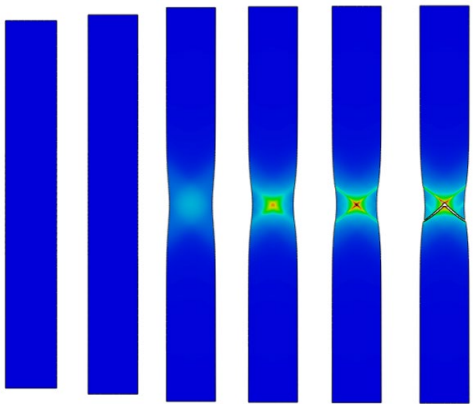

Figure 106. Through-thickness Necking and Failure of 1.4 mm Plane Strain Tension Sample

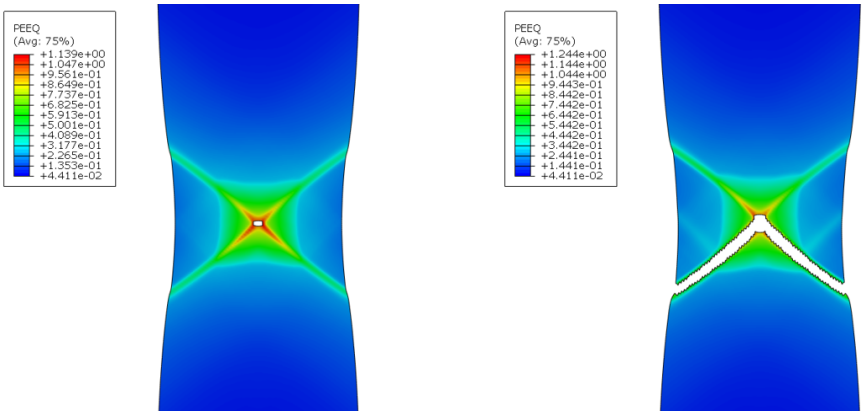

Figure 107. Initiation and Failure of 1.4 mm Plane Strain Tension Sample

Figure 106 and Figure 107 illustrate the response of the sample at the various stages of deformation. Initially, deformation of the plate was homogeneous, followed by a localization setting in and a through-thickness neck developing. Development of the neck increased the stress triaxiality at the center of the neck to a level significantly above that of plane strain tension ($T_{\text{Plane strain}} = 1/\sqrt{3}$). Further loading caused localization of plastic straining into a narrow shear band at the center of the plate, followed by final fracture. This is consistent with the results shown by Anderson et al. [43] and in conjunction with the matching force-displacement response verifies the plane strain tension model developed here.

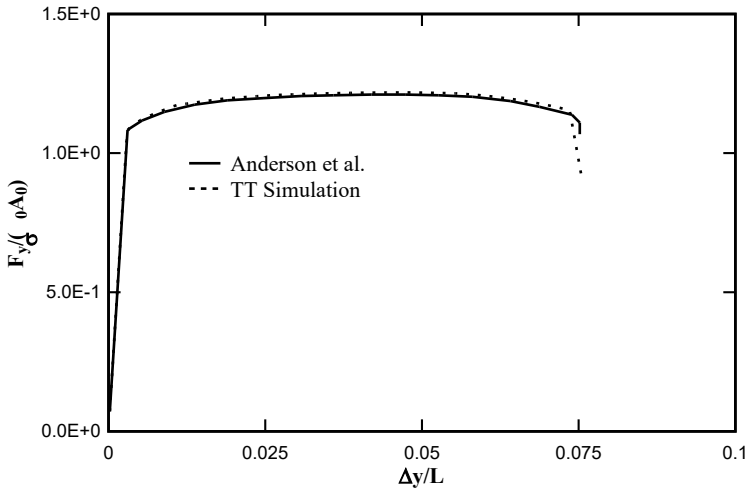

Figure 108. Normalized Force-displacement Curves for the Far-field Plane Strain Tension Tests for $N = 0.05$ and $f_0 = 0.02$

5.2.2 Plane Strain Bending Case

An overview of the plane strain bending test is shown in Figure 109. It comprises a deformable plate of thickness, t, and length, L, positioned above two rigid rollers with radius R_r. A rigid punch with a tip radius R_p was centered above the plate and translated vertically downward to simulate the test. The half distance between the rollers is denoted l_r and is determined from the plate thickness ($2l_r = 2R_p + 3t$) such that the plate and punch cannot jam between the rollers. The

rollers were constrained against translation, but free to rotate, with a tangential coefficient of friction $\mu_{fr} = 0.02$.

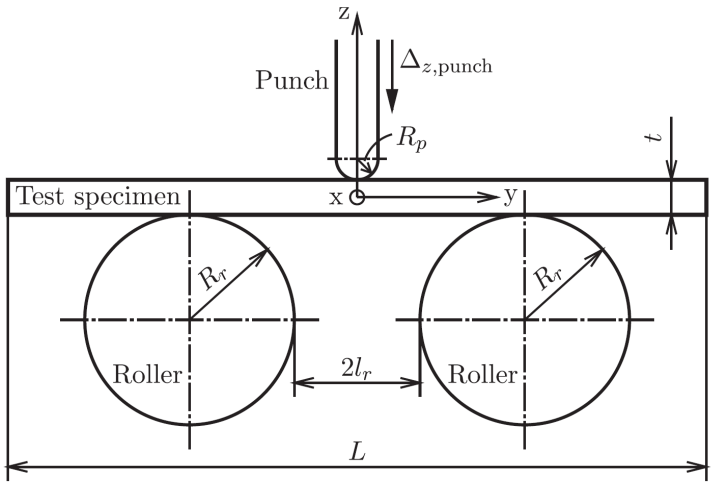

Figure 109. The Plane Strain Bending Test Setup [43]

The GTN material parameters used were the same as those adopted for the plane strain tension case (Table 30) with the remaining model parameters summarized in Table 31. An overview of the FE model developed is shown in Figure 110.

Table 31. Model Parameters for Plane Strain Bending

Parameter	Notation	Value
Length of plate	L	60 mm
Plate thickness	t	1.4 mm
Punch radius	Rp	0.43 mm
Roller radius	Rr	20 mm
Distance between rollers	2lr	5.06 mm

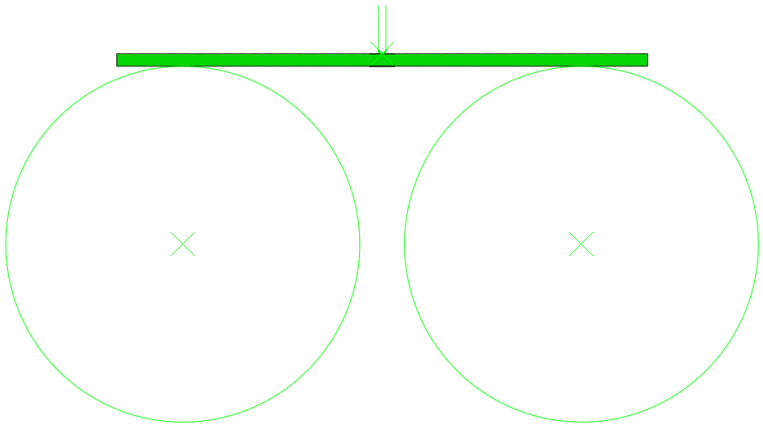

Figure 110. Overview of FE Model of 1.4 mm Plane Strain Bending Case

Figure 111 shows the response of the simulation at the point where instabilities and shear bands form on the tension side of the plate followed by crack initiation and propagation. The results show good correlation between those produced by Anderson et al. [43] as well as those observed

by Dykeman [44] during physical experiments. This includes the apparent ‘flattening’ at the mid-section and the observation of surface undulations (i.e., wrinkles) inside the region where the curvature has stopped evolving. A normalized bending moment-bending angle curve was also produced from the simulated test and compared to that produce by Anderson et al. This is shown in Figure 112, where again good agreement was achieved.

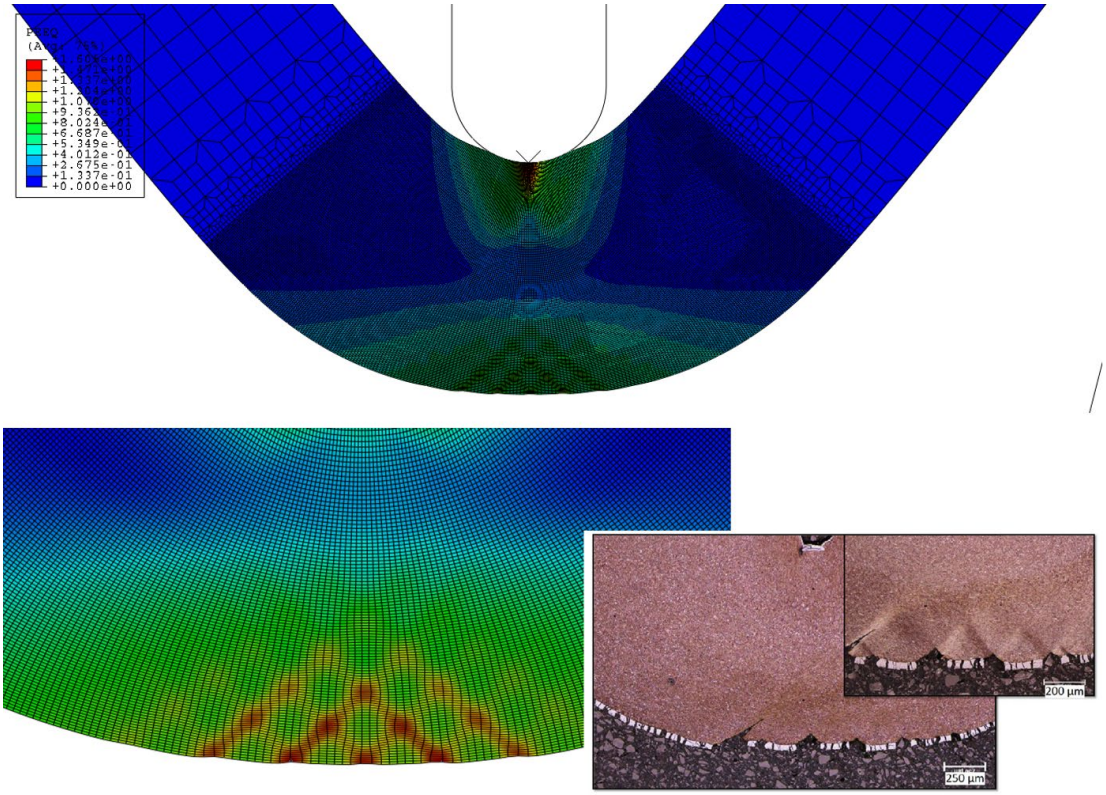

(a)

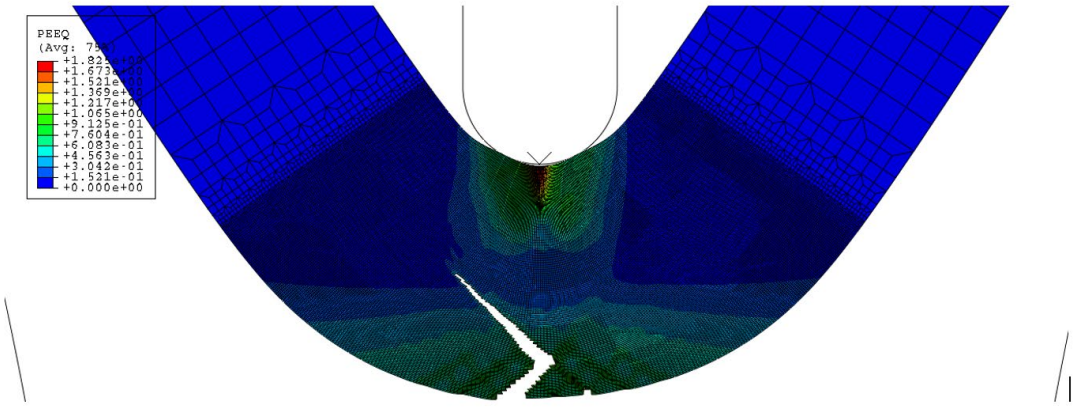

(b)

Figure 111. (a) Plastic Strain Contour Plots at Late Stage of Plane Strain Bending, Showing Surface Instabilities and Shear Band Formation on the Tension Side of Plate Compared with That Photographed by Dykeman Investigating Plane Strain Bending of 22mnb5 Boron Steel Plate with an Aluminum-Silicon Coating; (B) Crack Propagation and Failure of Plate

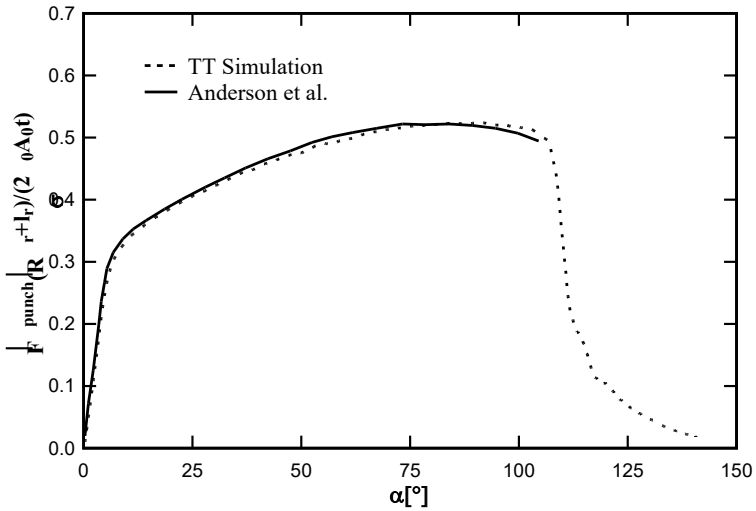

Figure 112. Normalized Bending Moment-bending Angle Curves for the Plane Strain Bending Test

5.3 Modified Plane Strain Tension and Bending Models

Following verification of the plane strain tension and plane strain bending models (and associated material models), the team conducted a series of sensitivities in which the plate thickness was increased. The plate thicknesses considered in the far-field plane strain tension and plane strain bending cases are summarized in Table 32 and Table 33. In each case the 'notional' and exact plate thicknesses are given since the exact plate thickness was required to be a multiple of the fixed element size (0.0109375 mm). In the plane strain tension cases the aspect ratio of length-to-thickness ~7.1:1.0 was maintained in all cases, as illustrated in Figure 113. In all cases the gauge (length 2*t*) was assigned a uniform fine mesh, with the mesh coarsening off outside that region.

The approximate number of elements is also provided in each case, and as the plate thickness increases the number of elements increases significantly. This has a corresponding effect on the simulation times, with the thicker plates taking longer to run (over 1 week for the 25.4 mm case on a high-powered cluster with 23 processers). It was also necessary to implement mass scaling to reduce the simulation times to reasonable timeframes.

Table 32. Model Parameters for Plane Strain Tension, Increased Thickness Study

Plate Thickness, *t* (mm)	Exact Plate Thickness, *t* (mm)	Plate Length, *L* (mm)	Gauge Length, *g* (mm)	Number Elements
1.4	1.4000	10.0000	2.800	~34E3
3.0	2.9750	21.1225	5.950	~152E3
9.0	8.9250	63.3675	17.850	~1.35E6
25.4	25.3750	180.16250	50.750	~55E6

Table 33. Model Parameters for Plane Strain Bending, Increased Thickness Study

Plate Thickness, t (mm)	Exact Plate Thickness, t (mm)	Plate Length, L (mm)	Punch Radius, R_p (mm)	Spacing Between Rollers, $2l_r$ (mm)
1.4	1.4000	60	0.43	45.06
3.0	2.9750	60	0.91	50.39
9.0	8.9250	80	2.74	72.26
12.7	12.6875	90	3.90	85.86
25.4	25.3750	180	7.79	131.71

For the plane strain tension simulations, the sample size was scaled up as the plate thickness increased. However, for the plane strain bending cases, some additional parameters needed to be fixed. The roller radius was therefore fixed across cases at R_r = 20 mm. The relationship between punch radius R_p and plate thickness t was also assumed to remain constant across all cases, as in the baseline case, such that t / R_p = 1.4 / 0.43 = 3.26. The equation used by Anderson et al. for determining the gap between rollers ($2l_r$) (shown in Figure 113) was then used to complete the arrangement. The length of the sample L was just sufficient to bridge between rollers. This gave a length-to-thickness aspect ratio for the plates that was greater than that used in the plane strain tension simulations.

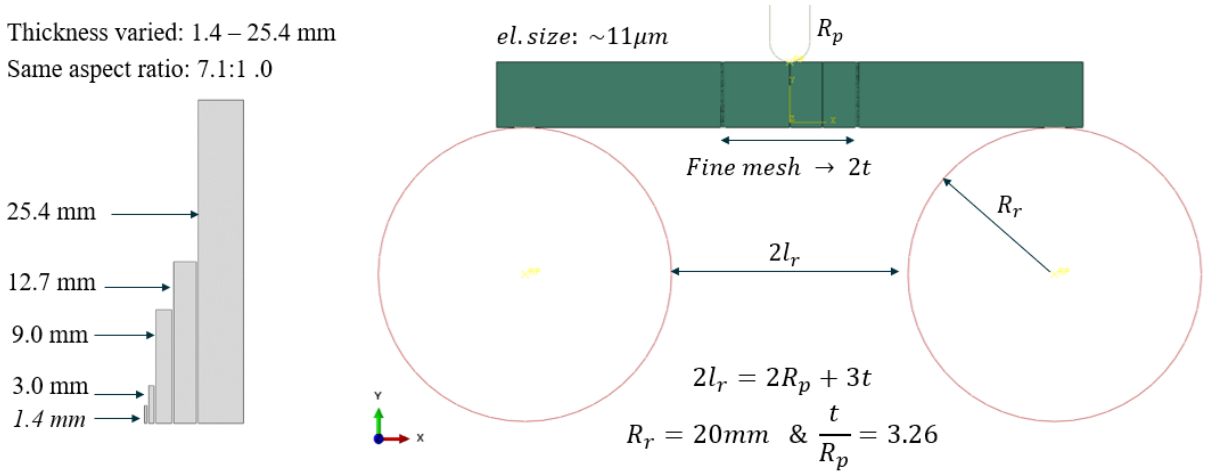

Figure 113. Illustration of Plane Strain Tension Samples and Plane Strain Bending Arrangement

5.3.1 Far-Field Plane Strain Tension Results

The far-field plane strain tension simulations showed a relatively weak relationship between plate thickness and ductility, with ductility increasing slightly with increasing plate thickness (see Figure 114 and Table 34). Figure 114 shows the normalized forced-displacement curves for each sample while Table 34 provides the calculated strain-to-failure. Some results from the 9.0 mm tension sample are shown in Figure 115 and Figure 116, where the sample necks, triaxiality increases, and then fracture initiates. In Table 34, the fracture strain has been calculated across the gauge length ($2t$) in each case. For conciseness not all results are illustrated here.

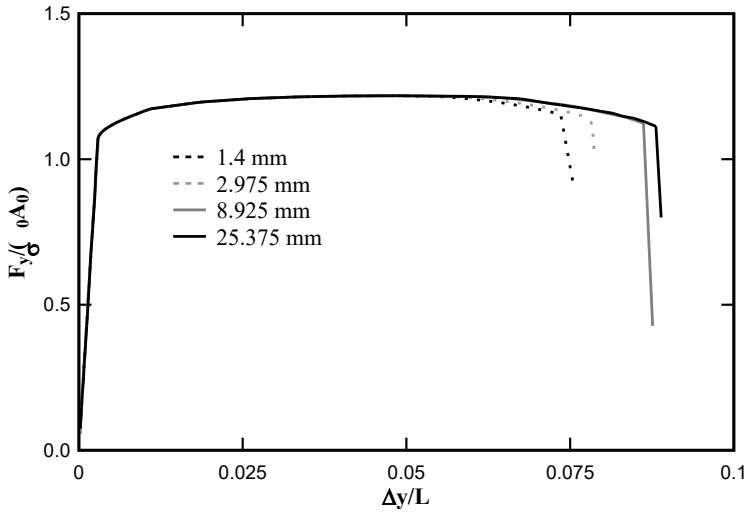

Figure 114. Normalized Force-displacement Curves for the Far-field Plane Strain Tension Tests for t = 1.4, 3.0, 9.0, and 25.4 mm

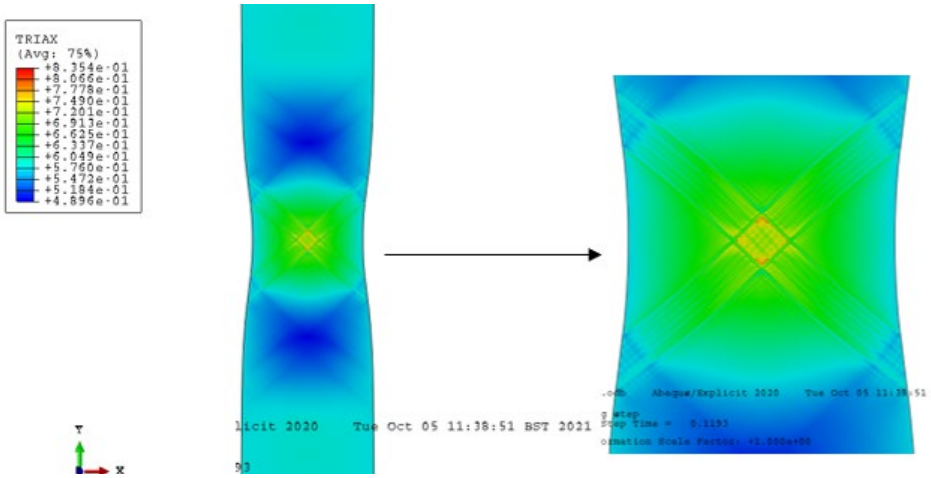

Figure 115. Plot showing Stress Triaxiality in 9.0 mm Plane Strain Tension Sample at Onset of Failure

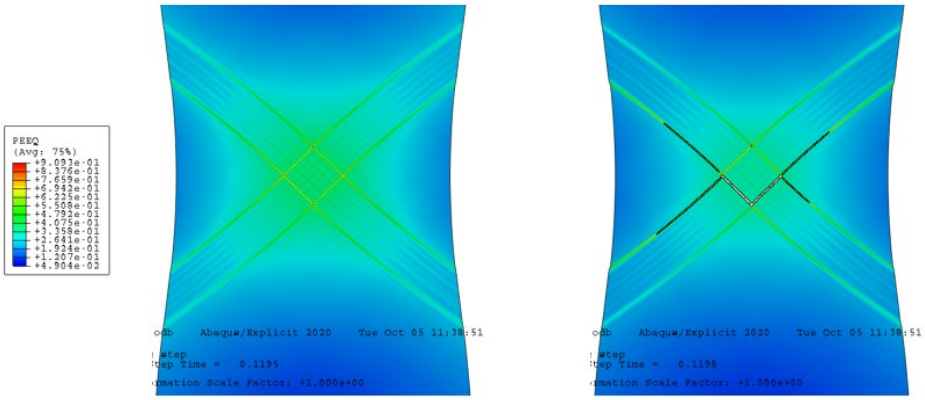

Figure 116. Plot Showing Plastic Strain in 9.0 mm Plane Strain Tension Sample When Failure Initiates and Starts Propagating through the Thickness

Table 34. Results from Plane Strain Tension, Increased Thickness Study

Plate Thickness, *t* (mm)	Fracture Strain (%)
1.4	7.36
3.0	7.87
9.0	8.62
25.4	8.81

5.3.2 Plane Strain Bending Results

The plane strain bending simulations showed a stronger correlation between ductility and plate thickness, with ductility decreasing with increasing plate thickness. Figure 117 shows the normalized bending-moment bending angle curves for 4 of the 5 samples investigated. It shows that as the plate thickness increases, the bend angle at which failure initiates decreases. Moreover, the area under the curve in each case represents the energy absorbed before failure, which decreases with increasing plate thickness.

The output required to plot this curve for the 25.4 mm sample was not requested, therefore it has not been included in Figure 117. Nevertheless, the output obtained from the 25.4-mm-thick sample enabled calculation of the fracture strain, which has been compared to that of the remaining samples in Table 35.

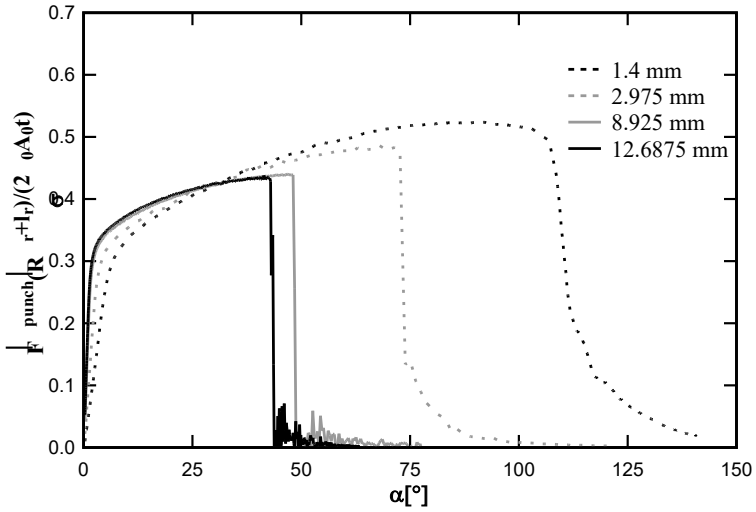

Figure 117. Comparison of the Normalized Bending Moment-bending Angle Curves for the Plane Strain Bending Tests at Increased Thickness

In Table 35, the fracture strain calculated was obtained from the bottom (i.e., tensile) surface using the gauge length, 2*t,* at the point at which fracture first initiates. The procedure for extracting the fracture strains is shown in Figure 118. The deformed length of the bottom surface was obtained by creating a path along the length of the gauge and plotting the true distance of the path. In Figure 118 (c) the true distance has been plotted against plastic strain. It shows that in this case (i.e., the 25.4-mm sample) plasticity at the extremities of the gauge is close to zero, and then gradually increases toward the center where the average plastic strain is approximately 40 percent. Local spikes in plastic strain are observed, and these are associated with the formation of localizations and instabilities on the bottom surface just prior to fracture initiation. This is

illustrated by way of example in Figure 119, which shows the response of the 9.0-mm-thick sample when fracture initiates. Note that a similar surface undulation or wrinkling pattern is observed in the tension face of the bending sample prior to fracture propagation.

Table 35. Results from Plane Strain Bending, Increased Thickness Study

Plate Thickness, *t* (mm)	Bend Angle (deg)	Fracture Strain (%)
1.4	106	42.9
3.0	73	32.6
9.0	48	23.5
12.7	43	20.6
25.4	35	17.4

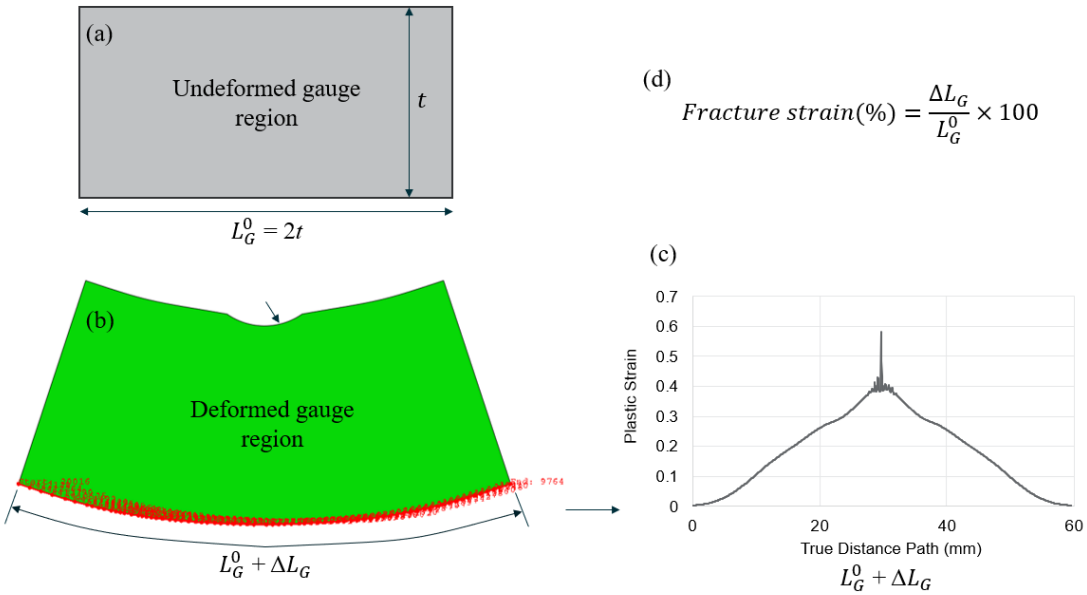

Figure 118. Calculation of Fracture Strain: (A) Initial Undeformed Shape of Gauge Region; (B) Deformed Shape of Gauge Region at Initiation of Fracture; (C) Plot Showing Plastic Strain vs. Distance Along Deformed Gauge Length (bottom surface); (D) Fracture Strain Calculation

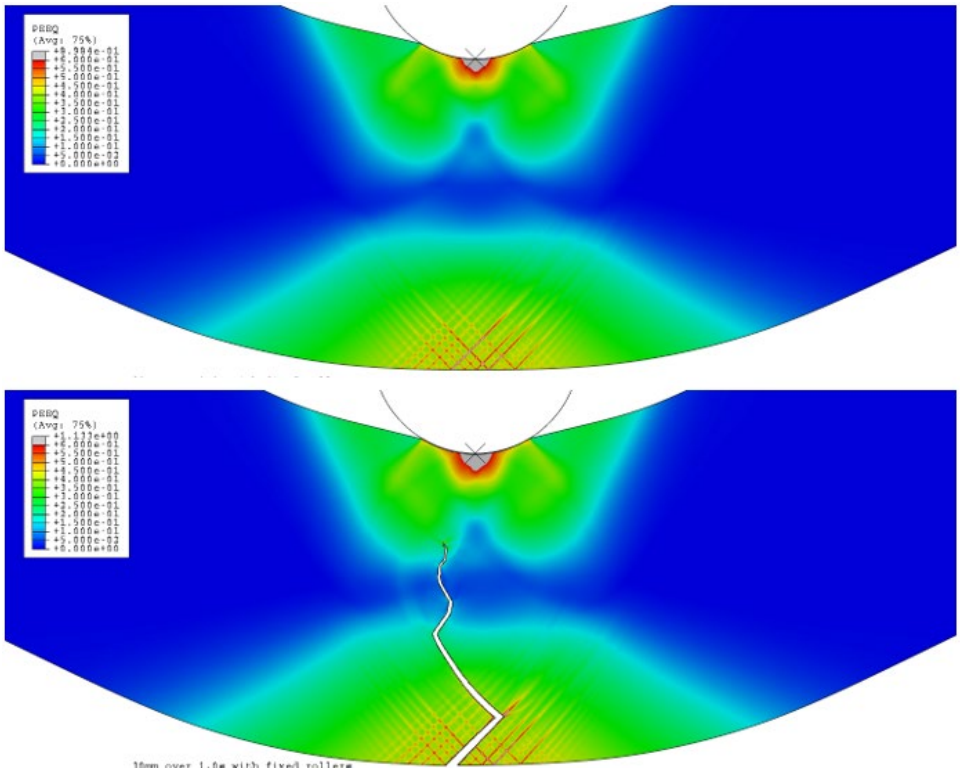

Figure 119. Plastic Strain Contour Plot of 9.0 mm Plane Strain Bending Sample When Fracture Initiates

5.4 Plate Thickness vs Ductility Results Summary

The results of the plate thickness versus ductility investigation are summarized in Figure 120, which shows that there are fundamental differences between plane strain tension and plane strain bending. The first fundamental difference is that the fracture stain in plane strain bending is higher than in plane strain tension. This was one of the key findings of Anderson et al. [43] and is explained by the absence of necking in the plane strain bending case. When necking occurs in plane strain tension the stress triaxiality at the center of the neck increases to levels significantly above that of plane strain tension (i.e., 0.577). By contrast, the absence of necking in plane strain bending maintains the stress triaxiality on the lower tensile surface equal to that of plane strain tension. Figure 121 shows stress triaxiality in the 9 mm plane strain bending simulation with the lower contour limit set to 0.4.

The second fundamental difference observed, and which is unique to this study, is the apparent reduction in ductility in the plane strain bending condition that occurs with increasing plate thickness, and conversely the relatively little change in ductility that occurs over the same range of plate thicknesses (i.e., 1.4 – 25.4 mm) in the plane strain tension condition. The reason for this behavior is currently not well understood and further research is necessary to understand the mechanism behind the observed differences based on thickness.

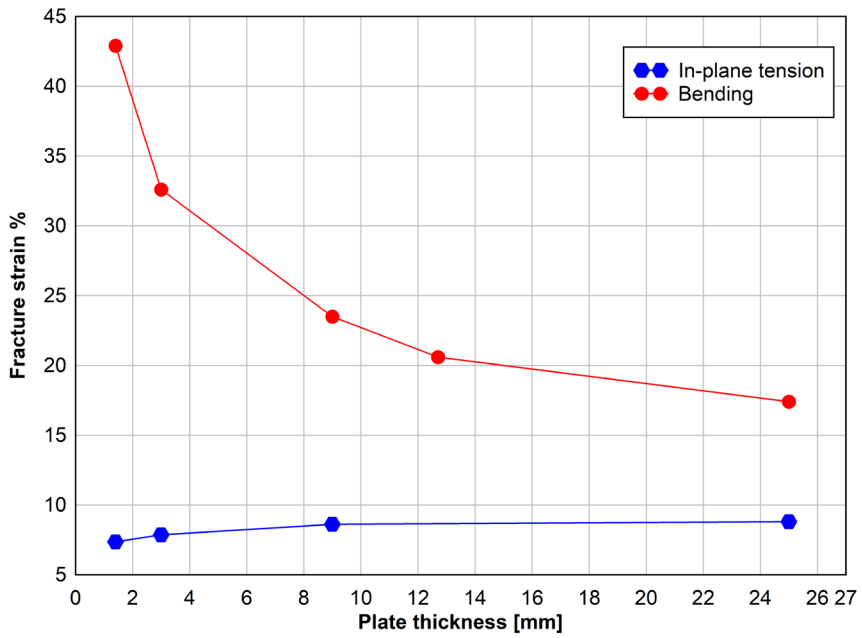

Figure 120. Fracture Strain Versus Plate Thickness for Far-field Plane Strain Tension and Plane Strain Bending Conditions

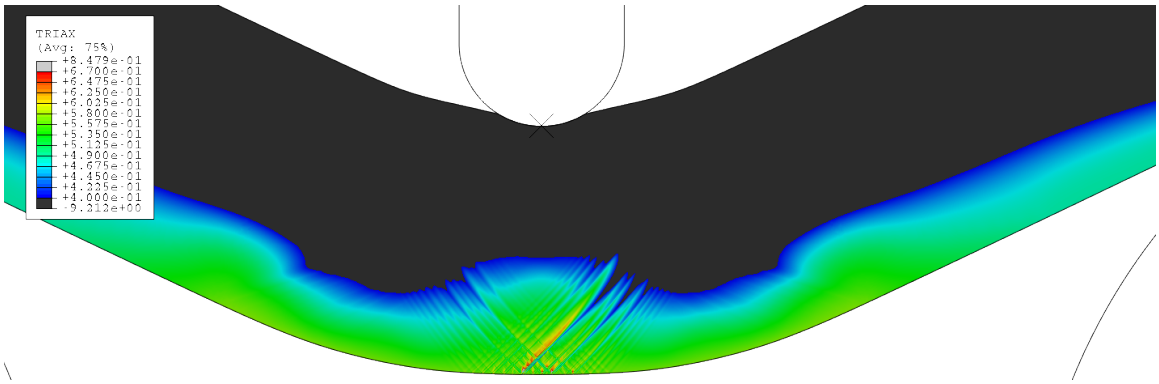

Figure 121. Plot Showing Stress Triaxiality in 9-mm-thick Plane Strain Bending Simulation

These findings are consequential for many industries including the tank car industry since the results show that increased plate thickness is associated with reduced ductility in bending. In previous sections of this report, it was shown that similar levels of puncture resistance could be achieved by increasing shell thickness or implementing a multi-layer solution in which the total plate thickness is the same as the equivalent thick shell solution. For reference, side impact survival speeds in the region of 23 mph were achievable with both solutions when using an equivalent shell thickness of 1.5 inches and a 12 x 12- inch indenter. Those findings assumed constant ductility across the different plate thicknesses, which varied from 0.5 to 1.5 inches.

However, the results of this study show that a penalty is incurred by increasing thickness, and therefore the survival speed of the monolithic 1.5-inch-thick shell may be lower than that which was previously calculated. In the ductility versus plate thickness study, it was not feasible to run the 1.5-inch-thick bend test within a reasonable timeframe since the model size simply became too large. However, it was possible to extrapolate out using the data gathered from the 1.4- to

25.4-mm-thick samples. The plane strain bending fracture strains relevant to the thicknesses considered within the tank car puncture analyses are summarized in Table 36. In the final column of Table 36, the relative change in fracture strain has been calculated in comparison to the baseline thickness of 0.775 inches for which the BW curve used in the various puncture analyses was validated. The table shows that reducing the plate thickness to 0.5 inches gives a 12 percent increase in ductility, while increasing the plate thickness to 1.5 inches is projected to reduce the ductility by 19 percent. While it was not possible within this research effort to quantify how this translates to puncture speed, the results indicate that there is potential benefit to using multiple thinner plates and consequences for increasing plate thickness.

Table 36. Summary of Plane Strain Bending Fracture Strains for Tank Car Applications

Plate Thickness, *t* (in)	Plate Thickness, *t* (mm)	Fracture Strain (%)	Relative Change to 0.775-inch (%)
0.500	12.7	20.6	+12.0
0.775*	19.7*	18.4	0
1.000	25.4	17.4	-5.4
1.500**	38.1**	14.9	-19.0

*Interpolated value, ** extrapolated value

6. Feasibility, Scalability and Cost

This section discusses the feasibility, scalability, and cost associated with the mitigation measures considered in Section 4. The focus is shifted from development to design and where possible the following aspects have been considered:

- Feasibility – volumetric and mass constraints, impact on operations and performance, inspection and maintenance
- Scalability – manufacturing methods, joining methods, availability of materials, repeatability
- Long term performance – fatigue, corrosion, impact on rails
- Cost

6.1 Enhanced TC128-B

AM has developed a new low-carbon steel version of TC128-B that they estimate would improve puncture energy by approximately 12 – 14 percent over the current version. The new low-carbon steel features improved ductility and reduced strength. When similar modifications were made to the Actual TC128-B material model developed by Carolan and implemented within validated FE models of side impact, puncture energies were predicted to improve by the amount estimated by AM. This would show that from a crashworthiness perspective, there is merit to adopting the new low-carbon steel in future tank car construction. However, the improvement in puncture energy corresponds to a relatively small increase in puncture speed (~1 to 2 mph), and alone it is unlikely to significantly change the conditional probability of release.

From a feasibility, scalability, and cost perspective there is little difference in adopting the new steel as it has been designed to meet the requirements of grade TC128-B.

6.2 High Strength Steel

In Section 4.4.2 a high strength steel was calculated to more than double the puncture energy of the tank car if it were to replace the Actual TC128-B material. The high strength steel was considered to have a yield stress of 138 ksi (951 MPa) and the same failure strain as the Actual TC128-B material (~22 percent for a 2-inch gauge). These results were consistent with similar findings by the ATCCRP [41] where similar magnitudes of improvement were calculated across a wider range of puncture scenarios when using steels with yield strengths up to 135 ksi (HY-130).

High strength steels, or ultra-high strength steels (UHSS) as they are often called, are available in standard sheet thicknesses (3/16 – 4 inches), widths (48 – 120 inches) and lengths (up to 480 inches) and could be used in tank car manufacture. There is however a wide range of UHSS's, and manufacturing methods differ quite significantly (e.g., in terms of welding and heat treatment) depending on the type used. Therefore, it is difficult to generically assess the impact on cost by transitioning to a UHSS, but it is expected to be somewhat higher than current manufacturing costs.

There would be no direct impact on the rail by adopting this mitigation measure as the mass of the tank car would remain broadly the same.

6.3 High Ductility Steel

In Section 4.4.3 a high ductility steel was investigated and calculated to approximately double the puncture energy. The Actual TC128-B material model used in the baseline validated simulations had a relatively low ductility, only just meeting the minimum requirement of 22 percent elongation over a 2-inch gauge. The higher ductility version maintained the same strength but approximately doubled the elongation to failure. Implementing a high ductility material, where the objective is to approximately double the elongation to failure while maintaining strength, would require the transition from carbon steel to stainless steel. Types 304 and 316 stainless steel, for example, have elongations at break in the region of 60 to 70 percent, however the yield stress of both materials is only approximately half that of TC128-B. Duplex stainless steels have yield strengths closer to that of the Actual TC128-B material considered here, but the minimum elongations at break are correspondingly lower as a result (~25 percent).

From a feasibility and scalability perspective, transitioning to stainless steel for the tank shell would require significant changes to the manufacturing process. Stainless steel tanks would also be more expensive to manufacture and procure, but as evidenced in the oil and gas industry, they can provide good long term corrosion resistance in addition to good thermal resistance in the event of fire.

6.4 Thicker Tank Shell

The effect of increasing the tank shell thickness was investigated in Section 4.3, where plate thicknesses of 1.25 and 1.50 inches were considered. The shell thickness was shown to strongly influence puncture resistance, with the 1.5-inch-thick shell giving an approximate threefold increase in puncture energy. However, the findings from the plate thickness versus ductility study showed that increasing the plate thickness would reduce the strain to failure in plane strain bending. The corresponding influence on puncture resistance has not been quantified, other than to note that the findings from the 1.5-inch-thick plate tank car simulations may be overestimated.

Nevertheless, increasing the shell thickness represents a robust and, in some ways, simple solution to improving puncture resistance. From a volumetric and weight perspective, the solution satisfies the AAR plate B requirements, with minimal change to the overall dimensions of the tank and the overall mass remaining within the 286,000 lb limit. However, there are several challenges associated with this solution. The manufacturing process at many facilities may need to be adjusted, since rolling 1.5-inch-thick plate to a diameter of 102 inches appears to be feasible, specialist plate bending machinery may be required to do so. There would also clearly be an increased cost associated with welding. Currently the tank is constructed with two elliptically shaped heads and multiple barrel shaped shell sections (i.e., rings) all joined by submerged arc welding. If the current welding process could be used with the thicker plate, then as a minimum multiple more passes would be required to build up the welded joints.

There would also be repercussions for rail integrity and overall efficiency of transporting the commodity because of the weight increase. The addition of ~29,500 lb to a single tank (i.e., the weight increase from moving from a 0.775- to 1.5-inch-thick shell) would increase individual wheel loads by ~3.7 ton. This would increase wear on rail and affect useful fatigue life, with wheel loading being one of the most influential factors.

6.5 Multi-Plate Solution

The mitigation solutions discussed in the previous sections require modification to the tank shell and are therefore applicable to the design of new tank cars only. However, various multi-plate solutions may be applicable to both new and retrofit designs. The solutions investigated in this research demonstrated that, for this type of solution, the most important factor to affect puncture resistance was the total plate thickness. This is illustrated in Figure 122, where three different solutions provide approximately the same level of puncture resistance.

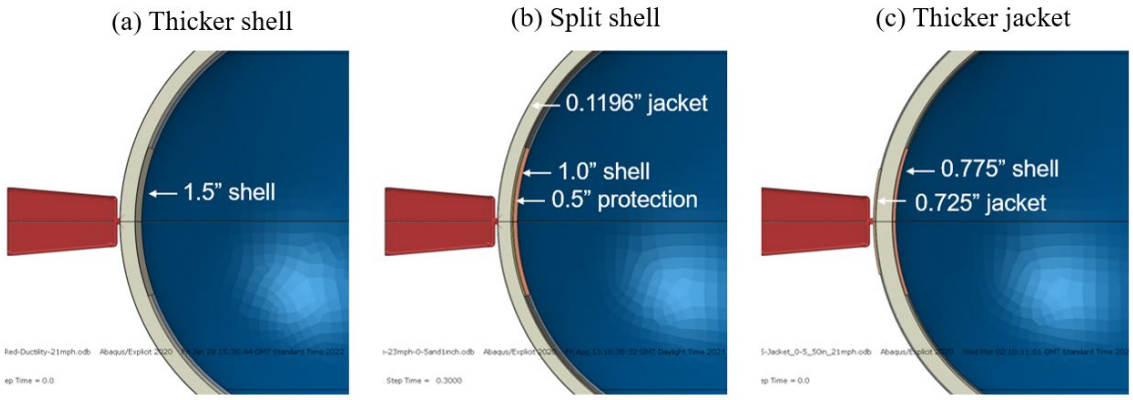

Figure 122. Different Mitigation Solutions with Total Plate Thickness of 1.5 inches

The multi-plate solutions discussed here refer to the split plate and thicker jacket solutions, with several benefits to adopting one of these solutions over the thicker shell solution. One is that the mitigation solution can be retrofitted to existing tanks, and another is that the existing tank construction methods can be retained with little or no change to the tank shell manufacture processes. Further improvement in puncture energies could be obtained by using different materials for the outer plate layers (e.g., high strength or high ductility steels). This is a clear advantage over the single thick shell solution, but one that was not quantified in this research effort. However, the reduction in ductility of thicker steel in bending coupled with the option of using high performance steel in the multi-plate solutions indicate that for an equivalent total plate thickness the multi-plate solution would provide superior puncture resistance.

One of the unique findings from this research is that splitting the outer plates into a series of unconnected vertical rings in some cases improved puncture resistance. However, the improvement was not significantly better than a continuous tank-within-a-tank solution. Nevertheless, the results indicate that the level of constraint (i.e., the strength of the connections) between adjacent outer plate layers was not consequential for puncture resistance. This provides a greater degree of freedom in regard to the manufacturing and joining process, with less emphasis placed on ensuring the strength and integrity of joints (i.e., welded connections).

Another option available with the multi-plate solution is to target the thicker material at the locations where there is the highest likelihood of impact (i.e., below the horizontal centerline and near the ends of the tank). This is illustrated graphically in Figure 123, which originated from a review of the relative frequency of damage to various tank car configurations [45], [46]. Targeting material would improve the overall weight efficiency of the tank car, providing further cost advantages over the single thicker shell solution.

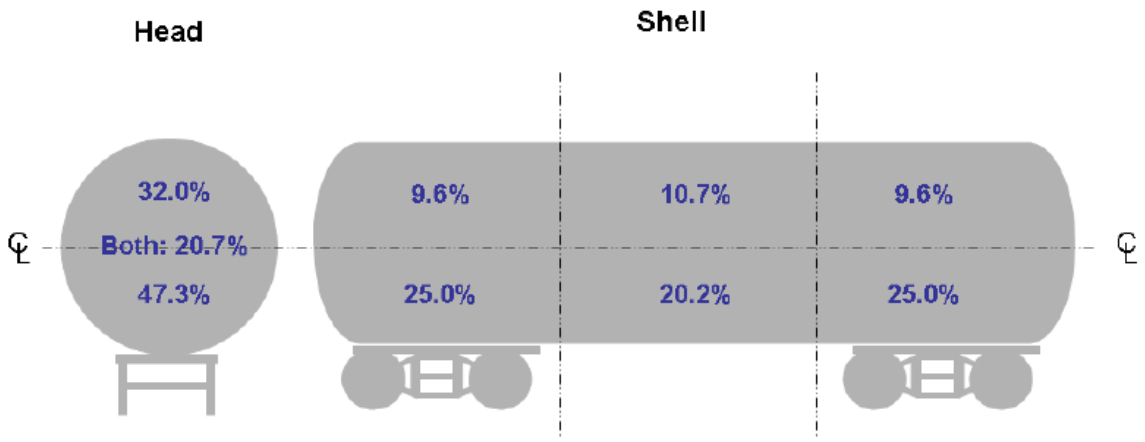

Figure 123. Percentage of Damage by Location on Insulated Tank Cars in Mainline Accidents [46]

6.6 Liners

Two types of liners were considered in Section 4.6: a liner aimed at providing secondary containment in the event the tank shell punctured, and a metal-elastomer bilayer aimed at improving the puncture resistance of the tank. The former was shown to be potentially effective in situations where the tank shell just punctured (i.e., at impact speeds in the region of 1 – 2 mph above the survival speed of the tank). In this scenario, the liner is required to have sufficient elongation to accommodate the indenter penetrating some way into the tank. Many tank cars are already lined, primarily with the objective of preventing internal corrosion or solvent action (specification provided in 49 CFR § 179.201-3 - Lined tanks). It is unlikely that any of these lined tanks would have been designed to provide a secondary containment mechanism in the event of shell puncture, but they could conceivably be designed to do so. This would require a much more specific research effort in collaboration with lining providers to determine the potential merits and feasibility of this solution. However, it is a solution that can be applied to new or existing tanks, is relatively lightweight, and would not significantly affect the basic manufacturing process of tank cars.

The metal-elastomer bilayer solution aimed at improving puncture resistance of the shell was not found to be effective, with an equivalent mass of steel offering better resistance.

6.7 Blunting Solutions

Blunting was shown in Section 4.7 to provide an effective means of improving puncture resistance. However, mitigation solutions developed with the specific aim of blunting the indenter are unlikely to provide any improved performance versus either the thicker shell or multi-plate solutions. In the side impact case, a 24-inch square indenter provided a similar level of puncture resistance (22 mph) to a total plate thickness of 1.5 inches exposed to a 12-inch square indenter (23 mph). However, to effectively blunt a 12-inch indenter to act over a 24-inch square area would likely require the 4-inch space between the tank shell and jacket to be increased and the void filled with a composite material or other novel structure. Additionally, the new material or solution would have to provide the same level of thermal performance as the current foam insulation. Taking these factors into consideration, it is not recommended to pursue solutions that focus on blunting as the primary means of mitigation.

7. Conclusion

The research team investigated various mitigation solutions aimed at improving the puncture resistance of hazmat tank cars by exercising validated FE models subject to side (i.e., shell) impact.

First, the team assessed a new low-carbon version of TC128-B steel developed by AM. The new steel featured higher ductility and reduced strength and had been predicted by AM to provide in the region of 12 – 14 percent improvement in puncture energy. Using information published by AM, researchers developed and evaluated a new pseudo-material model representing the new steel. The calculated improvement in puncture energy was very similar to that estimated by AM, representing an incremental improvement in the puncture resistance of tank cars.

Within the available tank car space and weight constraints, one of the simplest theoretical solutions is to increase the thickness of the tank shell. This applies to the design of new tank cars only and is a solution that has been adopted by the tank car industry in generational improvements where the head and shell thickness have been increased. The team investigated this solution by increasing the tank shell thickness to 1.5 inches and calculating the tank car response to side impact. A survival speed of ~22 – 23 mph (an approximate threefold increase in energy) was achieved. This utilized ~90 percent of the available weight.

Recognizing the challenges related to manufacturing a tank car with a 1.5 inch shell, researchers conducted a parametric study to investigate the effect of increased ductility and strength. In both cases, the puncture energy approximately doubled, with survival speeds increasing to 19 and 20 mph for the high ductility and high strength materials, respectively. These findings are consistent with those in previous research. Implementing a multi-layer (i.e., tank-within-a-tank) solution was also considered. The results indicated that in various configurations the survival speed could approximately match that of the 1.5-inch-thick shell provided that the total steel thickness was the same. The team found that splitting the outer plates into a series of rings did not significantly change the puncture resistance, despite separate sub-model analyses indicating otherwise. One significant benefit the multi-layer solution offers is the use of increased strength or ductility materials for the outer layers. This was not investigated in detail in this research but would likely improve the puncture resistance beyond that of a single plate of equivalent thickness.

Researchers investigated a secondary containment solution in the form of an internal liner, which was shown to be potentially effective at impact speeds just above the puncture speed. However, it was not effective at improving puncture resistance as a metal-elastomer bilayer. Mitigation solutions aimed at blunting the indenter were also considered, with the effectiveness similar to that of increasing the shell thickness, but with significant added complexity and cost. Therefore, pursuing mitigation solutions aimed primarily at blunting is not recommended.

Separately, the research team conducted a numerical investigation of the relationship between steel ductility and thickness. It was found that increasing steel thickness reduced ductility in the plane strain bending condition. This may have consequences for the puncture resistance of thicker steel tank cars (i.e., the predicted improvement may not be as high as expected).

In summary, the most promising mitigation approach to improve tank car puncture resistance is likely to be the multi-layer (i.e., tank-within-a-tank) approach, in which different steel grades can be used for the outer layers with the specific purpose of enhancing the overall puncture

resistance of the tank car. These findings match one of the key findings of the Advanced Tank Car Collaborative Research Program (ATCCRP), although it is not yet clear what level of puncture resistance may be achieved using this approach. The team recommends further research to investigate the level of puncture resistance possible using the multi-layer approach.

8. References

[1] NTSB (2004). Derailment of Canadian Pacific Railway Freight Train 292-16 and Subsequent Release of Anhydrous Ammonia Near Minot, North Dakota, January 18,2002 (Railroad Accident Report NTSB/RAR-04/01).

[2] NTSB (2008). Derailment of Norfolk Southern Railway Company Train 68QB119 with Release of Hazardous Materials and Fire, New Brighton, Pennsylvania, October 20, 2006 (Railroad Accident Report NTSB/RAR-08-02).

[3] NTSB (2009). Derailment of CSX Transportation (CSX) freight train Q380-09, Painesville, Ohio, October 10, 2007 (Railroad Accident Report NTSB/RAB-09-02).

[4] NTSB (2012). Derailment of CN Freight Train U70691-18 With Subsequent Hazardous Materials Release and Fire, Cherry Valley, Illinois, June 19, 2009 (Railroad Accident Report NTSB/RAR-12-01).

[5] NTSB (2013). Iowa Interstate Railroad Train Derailment and Subsequent Hazardous Materials Release and Fire, Tiskilwa, Iowa, October 7, 2011 (Railroad Accident Report NTSB/RAB-13-02).

[6] NTSB (2014). Norfolk Southern Railway Company Train Derailment and Hazardous Materials Release, Columbus, Ohio, July 11, 2012 (Railroad Accident Report NTSB/RAB-1408).

[7] NTSB (2017). Railroad Accident Brief: BNSF Railway Train Derailment and Subsequent Train Collision, Release of Hazardous Materials, and Fire, Casselton, North Dakota, December 30, 2013 (Railroad Accident Report NTSB/RAB1701).

[8] TSBC (2014). Runaway and main-track derailment, Lac-Mégantic, Quebec, 06 July 2013 (Railway Investigation Report R13D0054).

[9] NTSB (2006). Collision of Union Pacific Railroad Train MHOTU-23 with BNSF Railway Company Train MEAP-TUL-126-D with Subsequent Derailment and Hazardous Materials Release, Macdona, Texas, June 28, 2004 (Railroad Accident Report NTSB/RAR-06/03).

[10] NTSB (2005). Collision of Norfolk Southern Freight Train 192 with Standing Norfolk Southern Local Train P22 with Subsequent Hazardous Materials Release at Graniteville, South Carolina, January 6, 2005 (Railroad Accident Report NTSB/RAR-05/04).

[11] Pipeline and Hazardous Materials Safety Administration (2006). Hazardous Materials: Improving the Safety of Railroad Tank Car Transportation of Hazardous Materials. Notice of Public Meeting, Federal Register, Vol. 71, No. 222.

[12] US Department of Transportation (2015). Rule Summary: Enhanced Tank Car Standards and Operational Controls for High-Hazard Flammable Trains.

[13] Code of Federal Regulations (2015). Title 49 – Transportation, Appendix A to Part 179 – Procedures for Tank-head Puncture-Resistance Test, Pipeline and Hazardous Materials Safety Administration.

[14] Jeong, D. Y. (2009). Probabilistic Approach to Conditional Probability of Release of Hazardous Materials from Railroad Tank Cars During Accidents (Report No. IMECE2009-10872). FRA.

[15] Jeong, D. Y. (2016). Overview of Full-scale Tank Car Shell Impact Testing and Analysis. (Volpe National Transportation Systems Center Report).

[16] Tyrell, D. C., Jeong, D. Y., Jacobsen, K., & Martinez, E. (2007). Improved Tank Car Safety Research (Report No. RTDF2007-46013). FRA.

[17] Tyrell, D. C., Jacobsen, K,. Talamini, B., & Carolan, M. (2007). Developing Strategies for Maintaining Tank Car Integrity During Train Accidents (Report No. RTDF2007-46015). FRA.

[18] Carolan, M., Talamini, B., & Tyrell, D. (2008). Update on Ongoing Tank Car Crashworthiness Research: Predicted Performance and Fabrication Approach (Report No. JRC2008-63052). FRA.

[19] Carolan, M. E., Jeong, D. Y., Perlman, A. B., Tang, Y. H., & Gonzalez, F. (2011). Deformation Behavior of Welded Steel Sandwich Panels under Quasi-static Loading (Report No. JRC2011-56054). FRA.

[20] Jeong, D. Y., Tyrell, D. C., Carolan, M. E., & Perlman, A. B. (2009). Improved Tank Car Development: Ongoing Studies on Sandwich Structures (Report No. JRC2009-63025). FRA.

[21] Jeong, D. Y., Carolan, M. E., Perlman, A. B., & Tang, Y. H. (2011). Deformation Behavior of Welded Steel Sandwich Panels under Quasi-static Loading (Report No. DOT/FRA/ORD-11/06). FRA.

[22] Carolan, M. E., Jeong, D. Y., Perlman, A. B., Murty, Y. V., Namboordri, S., Kurtz, R., Elzey, R. K., Ananikitpaiboon, S., Tunna, L., & Fries, R. (2013). Application of Welded Steel Sandwich Panels for Tank Car Shell Impact Protection (Report No. DOT/FRA/ORD-13/19). FRA.

[23] Tang, Y. H., Yu, H., Gordon, J. E., Jeong, D. Y., & Perlman, A. B. (2008). Analysis of Railroad Tank Car Shell Impacts Using Finite Element Method (Report No. JRC2008-63014). FRA.

[24] Yu, H., Jeong, D. Y., Gordon, J. E., & Tang, Y. H. (2007). Analysis of Impact Energy to Fracture Un-Notched Charpy Specimens Made from Railroad Tank Car Steel (Report No. RTDF2007-46038). FRA.

[25] Bao, Y. & Wierzbicki, T. (2005). On the cut-off value of negative triaxiality for fracture. *Engineering Fracture Mechanics, 72*(7), 1049-1069.

[26] Nahshon, K. & Hutchinson, J. W. (2008). Modification of the Gurson Model for shear failure. *European Journal of Mechanics A/Solids, 27*(1), 1-17.

[27] Gonzalez, F. (2021). FRA Hazmat Tank Car Impact Test Research. *Railway Age*.

[28] Roman, J. (2020). Learning from Crude. *NFPA Journal*.

[29] PHMSA (2020). Federal Register / Vol. 85, No. 143/ Friday, July 24, 2020 / Rules and Regulations Hazardous Materials: Liquefied Natural Gas by Rail.

[30] Carolan M., & Przemyslaw, R. (2019). Side Impact Test and Analyses of a DOT-105 Tank Car (Report No. DOT/FRA/ORD-19/12). FRA.

[31] Wilson, N., Eshraghi, S., Trevithick, S., Carolan, M., & Rakoczy, P. (2020). Side Impact Test and Analyses of a DOT-105 Tank Car (Report No. DOT/FRA/ORD-20/38). FRA.

[32] Elkins, A. (2017). Field Guide to Tank Cars. Third Edition. Association of American Railroads.

[33] Carolan, M., Eshraghi, S., Wilson, N., Trevithick S., & Przemyslaw, R. (2020). Side Impact Test and Analyses of a DOT-105 Tank Car – 6 X 6 Inch Indenter (Report No. DOT/FRA/ORD-20/38). FRA.

[34] Tyrell, D. (2007). Developing Strategies for Maintaining Tank Car Integrity During Train Accidents (Report No. RTDF2007-46015). FRA.

[35] McKeighan, P. C., Jeong, D. Y., Cardinal, J. W. (2008). Mechanical Properties Of Tank Car Steels Retired From The Fleet (Report No. JRC2009-63060). FRA.

[36] Abotula, S., Konda, B., Walsh, W. J., Challa, V., Ros, T., & Murali, M. (2018). Analysis of Puncture Resistant Steel for Tank Cars *Steel Manufacturing Simulation and Visualization, 90*(4).

[37] Railway Supply Institute (n.d.). Tank Car Standards in North America.

[38] Anderson, T. L., Rose, B., McKeighan, P. C., & Kirkpatrick, S. W. (2007). Quantifying and Enhancing Puncture Resistance in Railroad Tank Cars Carrying Hazardous Materials, Phase II: Development and Validation of a Puncture Resistance Evaluation Methodology. Quest Reliability.

[39] Kirkpatrick, S. W. (2010). Detailed Puncture Analyses of Various Tank Car Designs, Final Report - Revision 1. Applied Research Associates.

[40] Pipeline and Hazardous Materials Safety Administration (2017). Petition for Rulemaking to Phaseout the Use of Tank Cars Not Meeting the HM-246 Specification to Transport Toxic-by Inhalation Materials (Docket No. PHMSA-2016-0165).

[41] Advanced Tank Car Collaborative Research Program Executive Committee (2016). ATCCRP Executive Summary and Conclusions.

[42] Xue, Z., & Hutchinson, J. W. (2005). Neck retardation and enhanced energy absorption in metal-elastomer bilayers. *Mechanics of Materials, 39*(5), 473-487.

[43] Anderson, R. G., Londono, G. J., Woelke, B. P., & Nielson, K. L. (2020). Fundamental differences between plane strain bending and far-field plane strain tension in ductile plate failure. *Journal of the Mechanics and Physics of Solids, 141*.

[44] Dykeman, J. (2019). Evolving test methods for fracture characterization and prediction. *EWI Workshop 2019*.

[45] Jeong, D. Y., Carolan, M. E., Perlman, A. B., & Tang, Y. H. (2011). Deformation Behavior of Welded Steel Sandwich Panels Under Quasi-Static Loading (Report No. JRC2011-56054). FRA.

[46] Treichal, T. T. (2007). Specific Locations of Damage and Lading Losses on Tank Heads and Shells (Report No. RA 06-04). RSI-AAR Railroad Tank Car Safety Research and Test Project

[47] Kirkpatrick, S.W. Ph.D (2010). Detailed Puncture Analyses of Various Tank Car Designs. Applied Research Associates.

[48] ASTM International (2008). Standard Test Methods for Tension Testing of Metallic Materials (E8/E8M - 16a).

Appendix A.
Material Properties

This section contains additional information about specific material properties or parameters that were used in development of the FE models.

A1 – Pneumatic Cavity / Air Properties

Table 37 and Table 38 contain information on the material properties used to define the air cavity in the full-scale and quarter-symmetry FE models. These properties were obtained from Carolan & Przemyslaw [30].

Table 37. Air Properties

Parameter	Value	Units
Universal Gas Constant (R)	73.583	in*lbf / mol*K
Molecular Weight (MW)	1.654×10^{-4}	$lbf*s^2$ / mol

Table 38. Molar Specific Heat for Air

Temperature (K)	C_{pmolar} (in*lbf / mol*K)
250	257.2
300	257.2
350	258.5
400	259.7

A2 – A1011 Jacket Material Properties

Carolan [30] developed and provided material property data to define the plasticity and damage behavior of A1011 based on available tensile test data. The true stress/true plastic strain data provided and required by Abaqus is tabulated in Table 39 and shown in Figure 124.

Table 39. True Stress/True Plastic Stain Inputs for A1011 [30]

True Stress (psi)	Plastic Strain (in/in)
47,000	0
46,000	8.22E-04
46,200	1.20E-02
53,000	3.00E-02
58,000	6.00E-02
62,000	1.10E-01
68,000	1.95E-01
125,000	1.15

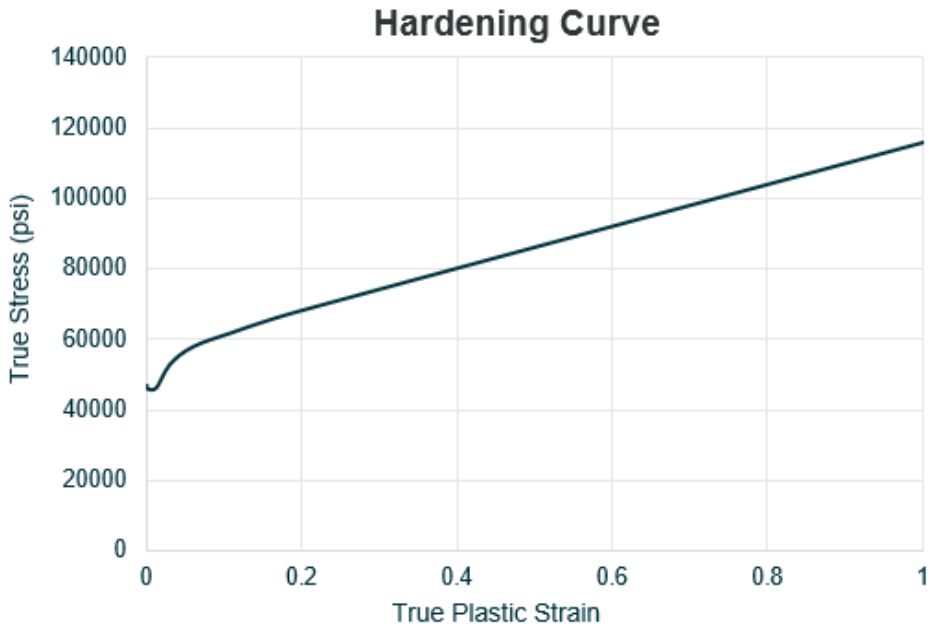

Figure 124. A1011 True Stress True Plastic Strain Curve [30]

Carolan developed a B-W failure envelope for A1011 using fully integrated shell elements (S4) with a fine mesh size of 0.04 inches and demonstrated good agreement between a simulated tensile test and the experimental data. In this research effort, the initial simulation was first replicated, and then new simulations were undertaken to develop a new B-W curve that could be used with larger and therefore more computationally efficient elements.

The original B-W curve developed by Carolan is shown in Figure 125. When used by the research team with S4 elements and a 0.04 inch mesh it resulted in the engineering stress-strain curve shown in Figure 126. This compared well to that originally produce by Carolan (Figure 127).

In a subsequent iterative process, researchers ran a series of new simulations in which the mesh size of the 'dog bone' tensile test piece was increased to 0.1196 inches (to provide an aspect ratio of 1:1) and the plasticity data points of the B-W curve were scaled by different amounts. The element type was also changed from full-integration (S4) to reduced integration (S4R) elements, again for computational efficiency. The damage progression energy was not changed and remained 1500 in-lbf/in^2. It was determined from the analyses that scaling the B-W curve by a factor of 0.9 gave good agreement with the results obtained using the parameters provided by Carolan. The resulting engineering stress-strain curves are compared in Figure 128.

The computational efficiency achieved by using larger elements and switching element type was approximately 9-fold. This increase in efficiency was important in the development of an efficient sub-model that could be used to assess multiple different mitigation solutions.

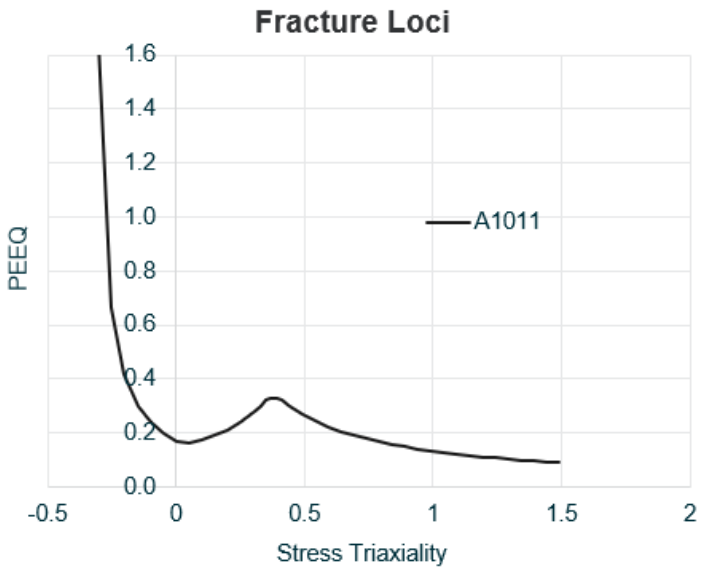

Figure 125. B-W Failure Envelope [30]

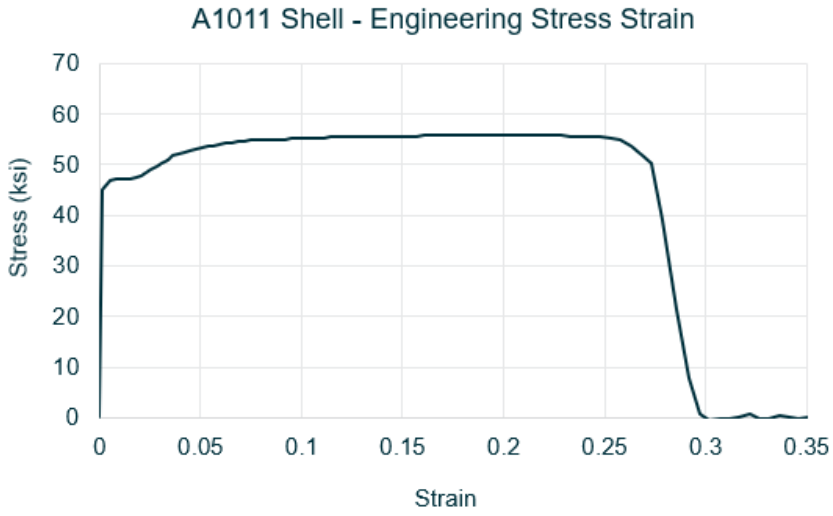

Figure 126. Engineering Stress Strain Curve Produced by Researchers

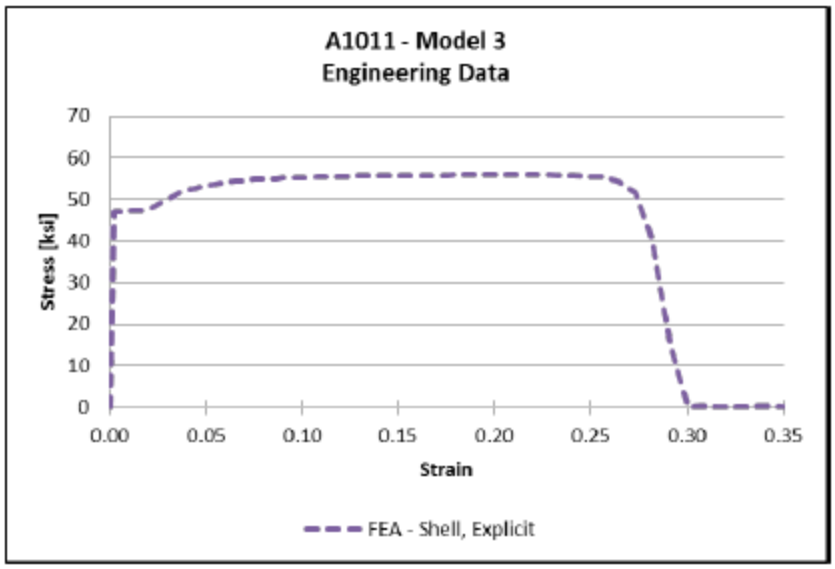

Figure 127. Engineering Stress Strain Curve Produced by Carolan [30]

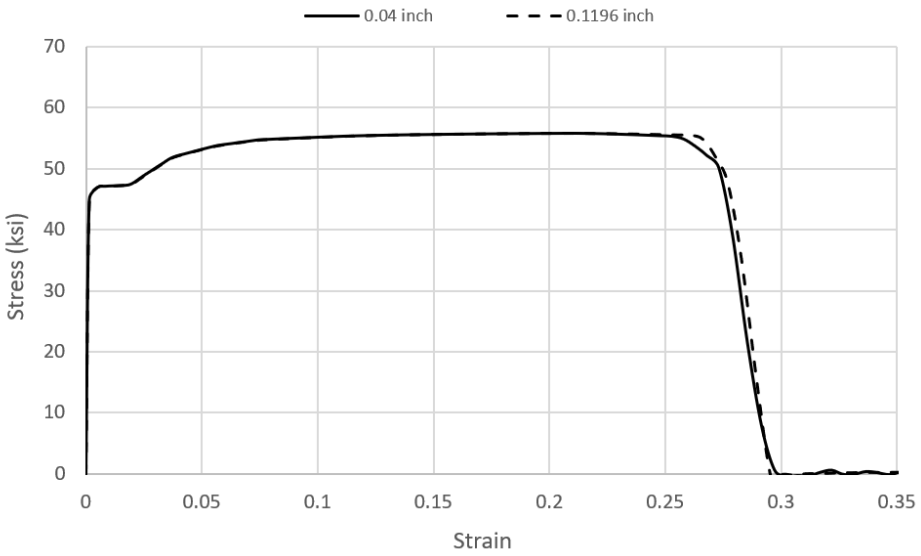

Figure 128. Comparison of Engineering Stress Strain Curves Produced using Carolan Parameters (0.04 inch & S4 elements) vs Research Parameters (0.1196 inch, S4R and scaled B-W curve)

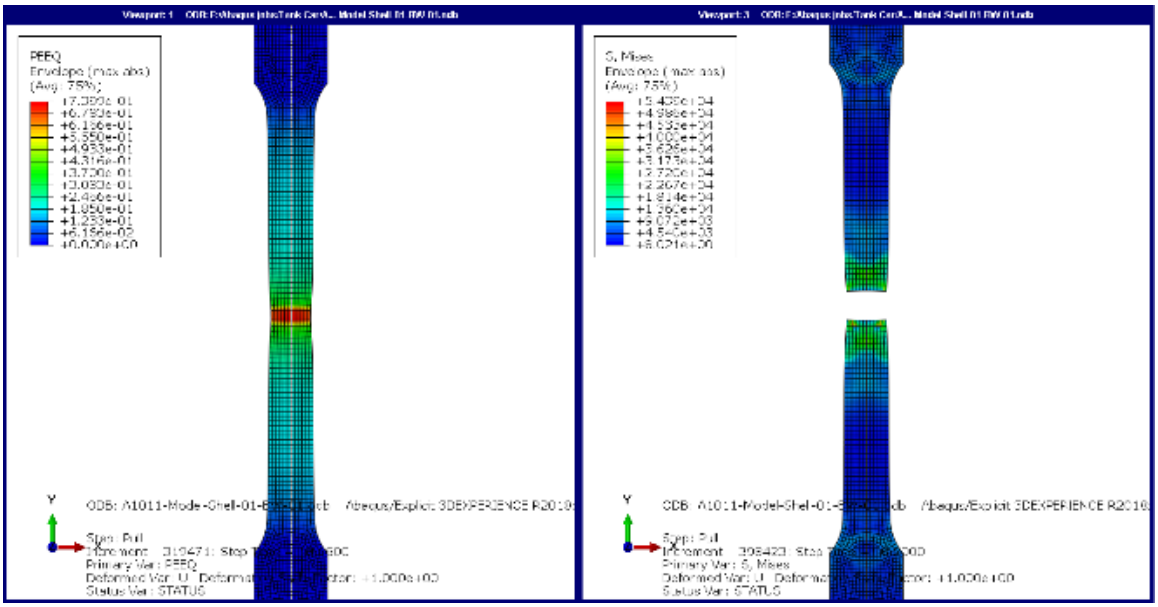

Figure 129. Plastic Strain Plot of Tensile Tests using Calibrate Material Properties for A1011 Material

Figure 129 above shows an overview of the 'dog bone' specimen used in the tensile test simulations. The plot shows plastic strain as the specimen undergoes necking and failure.

Appendix B.
TC128-B Material Properties

This section describes the development and verification of the Actual TC128-B material model used within the solid element regions in both the full-scale models and applicable sub-models.

In Appendix F4 of [30], Carolan describes the characterization procedure of three different variations of TC128-B material. Two of the variations, referred to as '*New Normalized*' and '*Test 2,*' were developed prior to the full-scale impact test (i.e., Test 6). These two materials were used in pre-test FE models to predict the puncture speed and therefore calculate the target ram car speed for Test 6. Following the completion of Test 6, a third material referred to as '*Actual Test Material*' was characterized using tensile test data obtained from material cut directly from the tank shell. A summary is provided in Table 40 below.

Table 40. TC128-B Material Models

TC128B Model	Performed	(Original) Source
Test 2	Pre-Test	Kirkpatrick [47]
New Normalized	Pre-Test	Kirkpatrick [47]
Actual Test Material	Post Test 6	Carolan [30]

Carolan provided hardening curves, fracture loci (i.e., B-W Damage Models), and damage evolution parameters for each of the three materials, along with information on the element type and size for which the material models were calibrated. Note that the B-W damage models and associated damage evolution parameters are mesh dependent. The hardening curves and B-W damage models for each material are shown in Figure 130 and Figure 131, respectively.

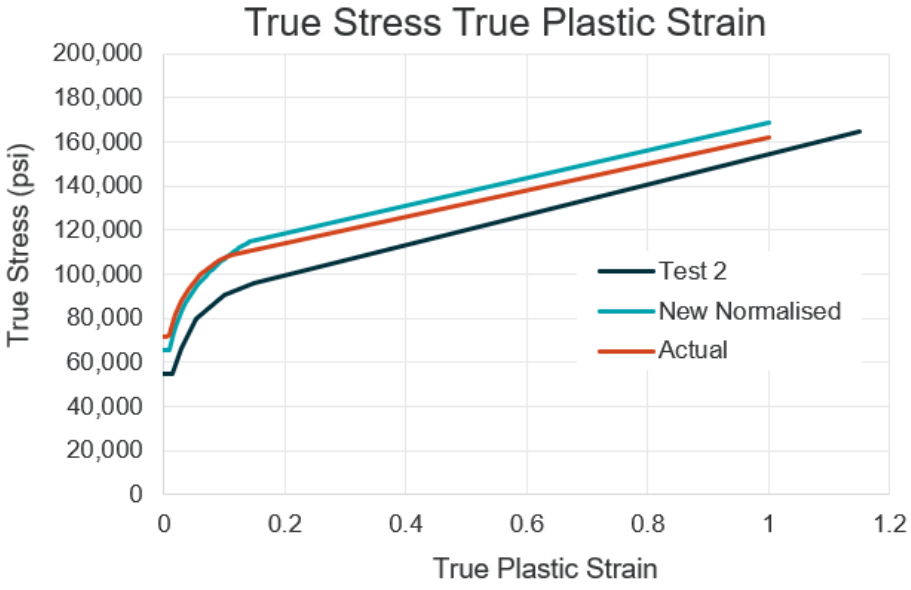

Figure 130. TC128-B True Stress/True Plastic Strain Curves [30]

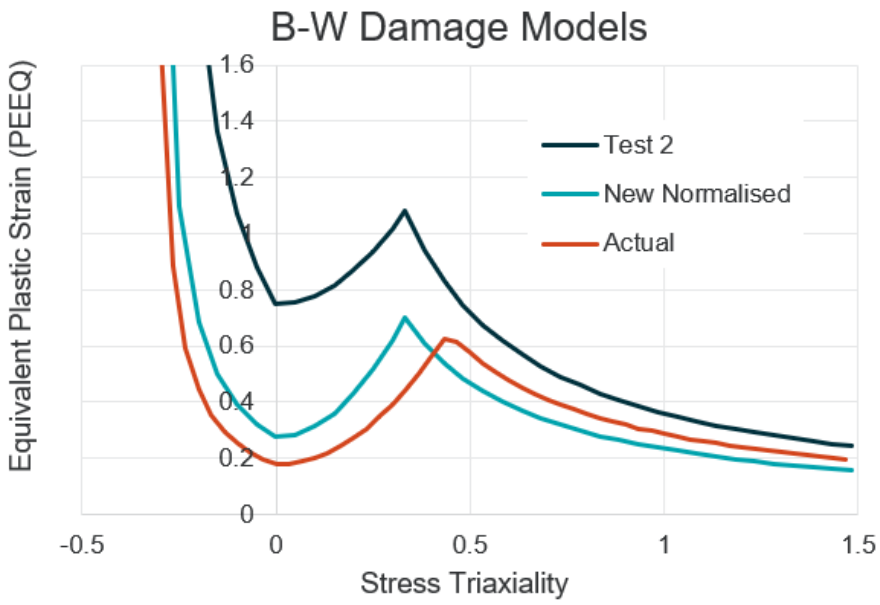

Figure 131. TC128B Fracture Loci [30]

A summary of the element formulations and damage evolution parameters used for each material model is provided in Table 41.

Table 41. TC128-B Tensile Coupon Model Characteristics

TC128B Model	Mesh & Elements	Mesh Size in Neck	Damage Progression
Test 2	Bricks – C3D8I	0.085 in	700 in-lbf/in^2 Exponential
New Normalized	Bricks – C3D8I	0.085 in	700 in-lbf/in^2 Exponential
Actual Test Material	Bricks – C3D8I	0.085 in	1,400 in-lbf/in^2 Linear

To verify the Actual material model for use in the full-scale tank car analyses (and subsequent sub-model analyses), the research team conducted a series of Round Bar Tensile test simulations using geometry developed in accordance with ASTM E8 [48] (i.e., 2-inch gauge). Sample images from the analyses are shown in Figure 132 and Figure 133.

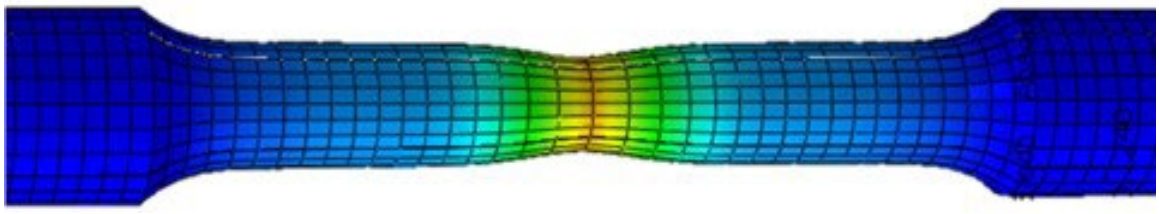

Figure 132. Necking of Round Bar During Tensile Test

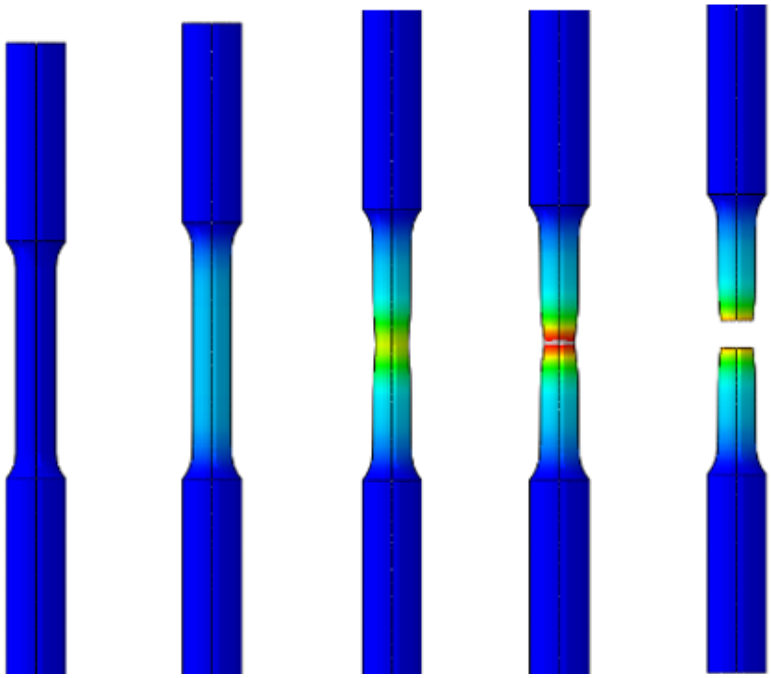

Figure 133. Round Bar Tensile Tests Showing Plastic Strain Contours

The resulting engineering stress-strain curves computed from the simulated tests are shown in Figure 134. They compared very well to the experimentally obtained curves, as shown in Figure 135 and Figure 136, in which the calculated engineering stress-strain curves have been overlaid onto the experimentally obtained versions.

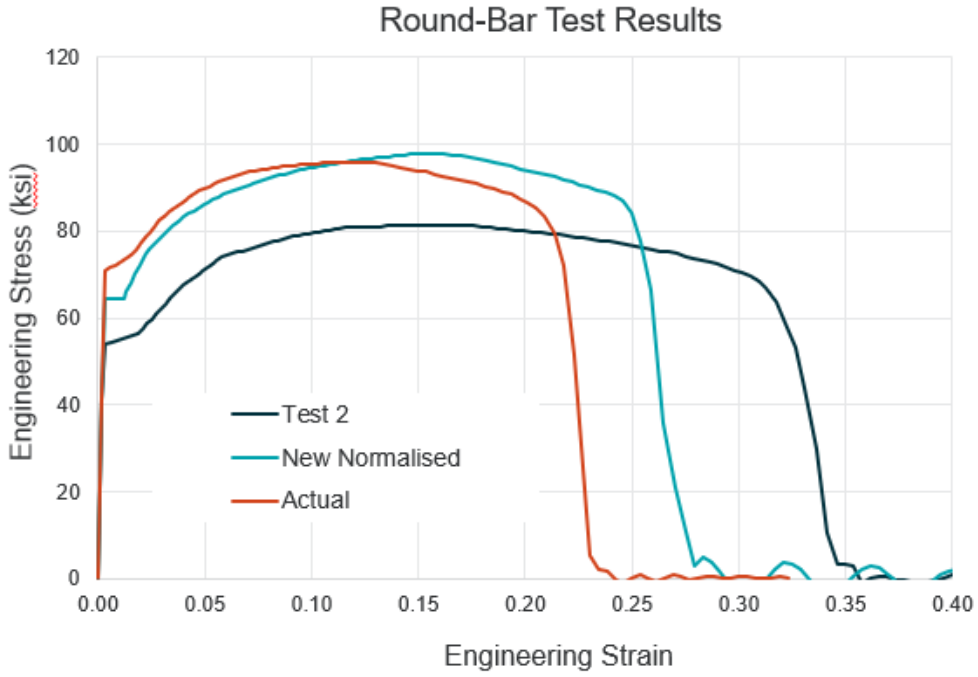

Figure 134. Engineering Stress Strain Curves from Round Bar Simulations

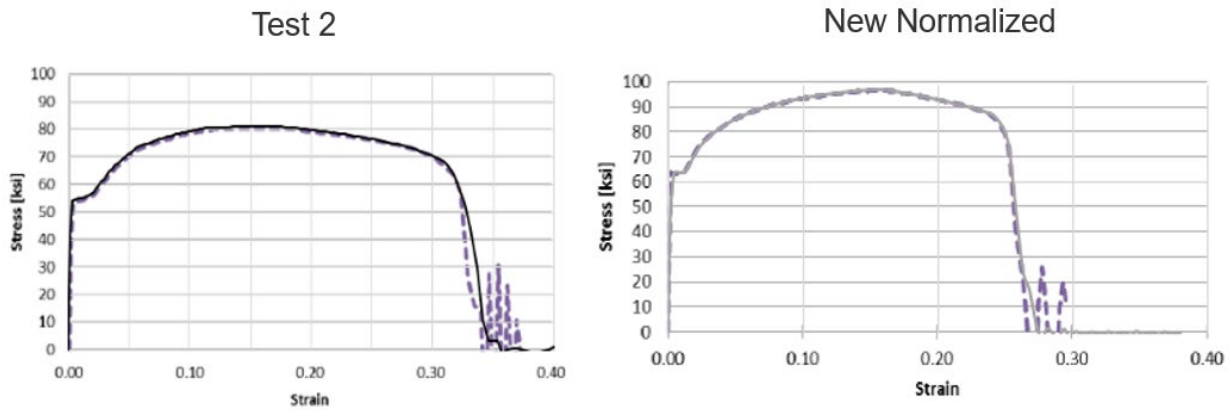

Figure 135. Engineering Stress Strain Curves from Researched Round Bar Simulations Overlaid onto Original Curves (Test 2 and New Normalized, dotted lines)

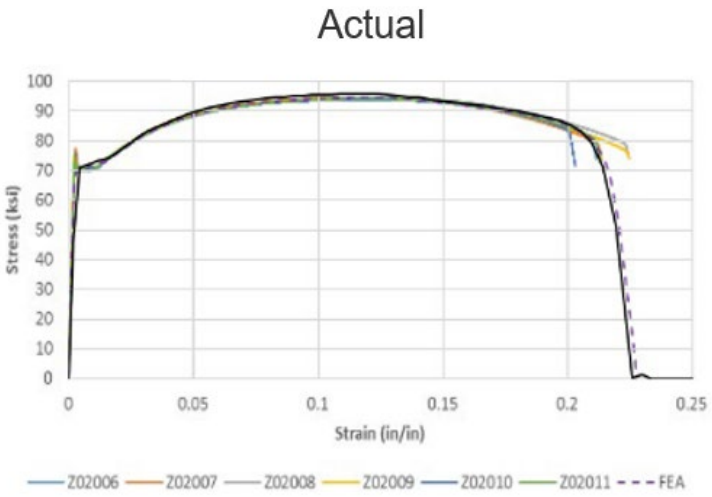

Figure 136. Engineering Stress Strain Curve from Researched Round Bar Simulation (solid black line) Overlaid onto Original Curve (Actual)

In addition to validating the use of the material model parameters developed by Carolan, the results illustrate the variability in material properties of TC128-B. The material specifications for TC128-B are summarized in Table 42. Each of the three versions characterized meet these standards, although the Actual material from Test 6 only just met the required minimum ductility limit of 22 percent elongation. It is also notable that there is an upper limit specification for the Ultimate Tensile Strength (UTS).

Table 42. Requirements of TC128-B Material

Property	Value
Min. Yield Strength	50 ksi (345 MPa)
UTS Range	81 – 101 ksi (558 – 696 MPa)
Elongation at Failure (2-in gauge)	22%
Elongation at Failure (8-in gauge)	16%

Appendix C.
Full-Scale Model, Potentiometer Results

This appendix contains additional output from the full-scale simulation described in Section 2.3 to validate the FE model against test data.

Figure 137 compares the change in length in the FE model versus Test 6 for the string potentiometer located at the center of the tank (i.e., directly behind the impact zone) and oriented in the direction of travel of the indenter.

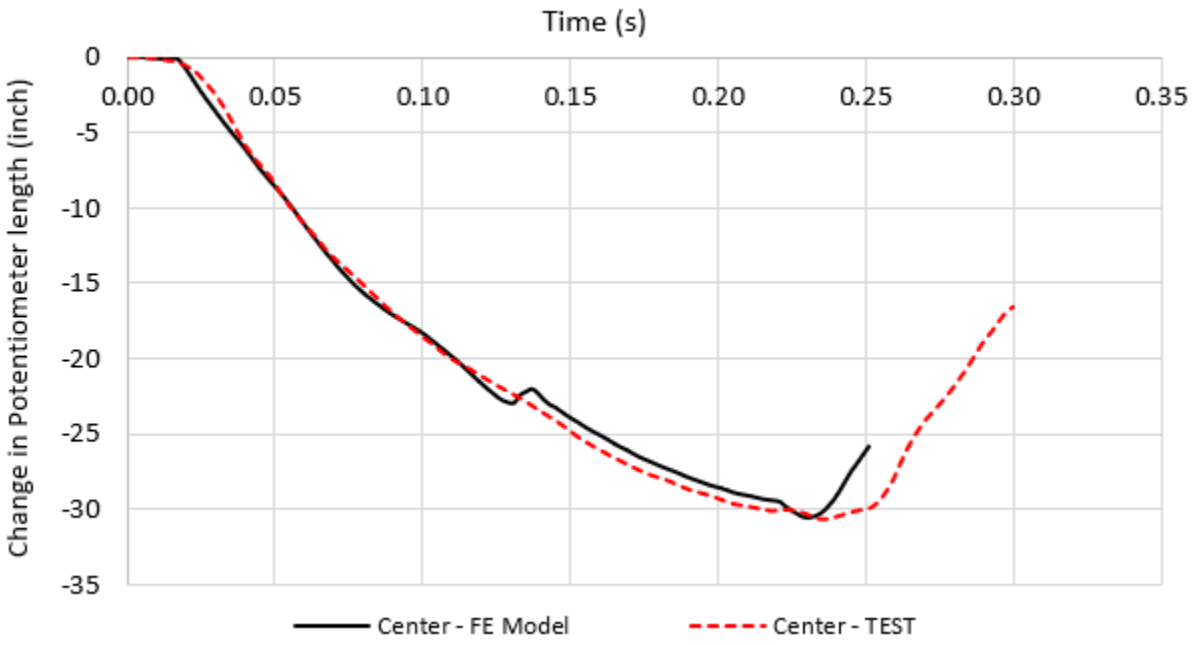

Figure 137. Comparison of String Potentiometer Length vs Time, Centre of Tank

Figure 138 compares the change in length in the FE model versus Test 6 for the string potentiometer located 24 inches from the center of the tank. Figure 139 compares the same for the string potentiometer located 48 inches from the center of the tank and Figure 140 for the skid. Figure 141 compares the vertical response and Figure 142 the response at the head of the tank.

In general, the response of the FE model compares well against the physical test data, particularly until puncture occurs at approximately 220 ms.

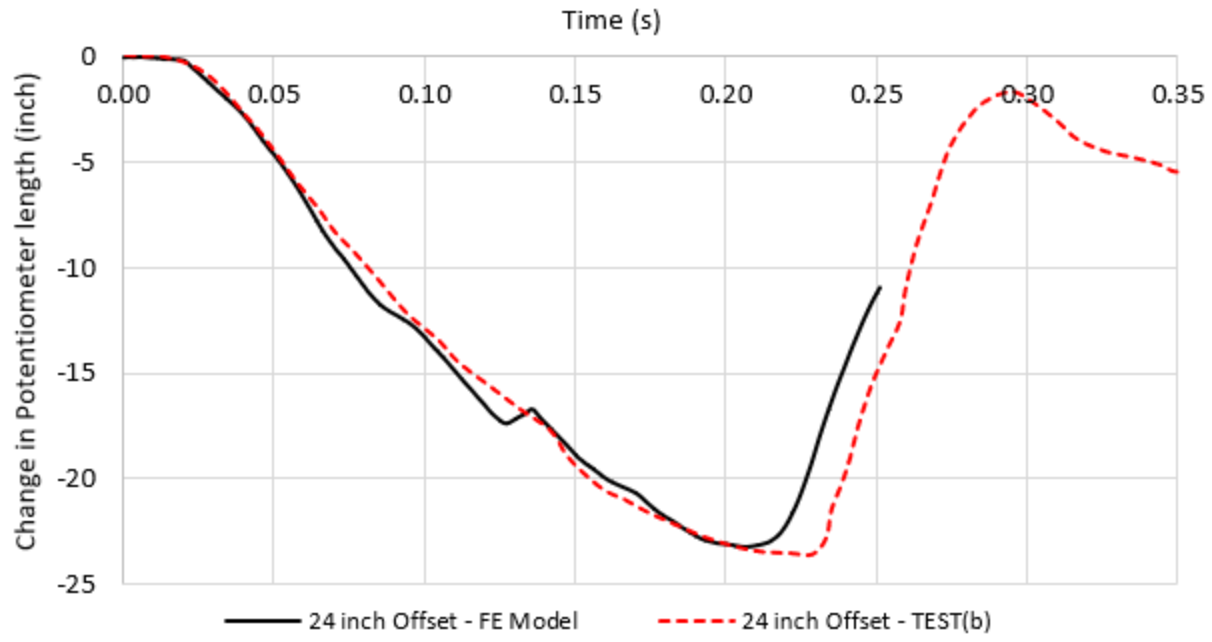

Figure 138. Comparison of String Potentiometer Length vs Time, 24-inch Offset from Center of Tank

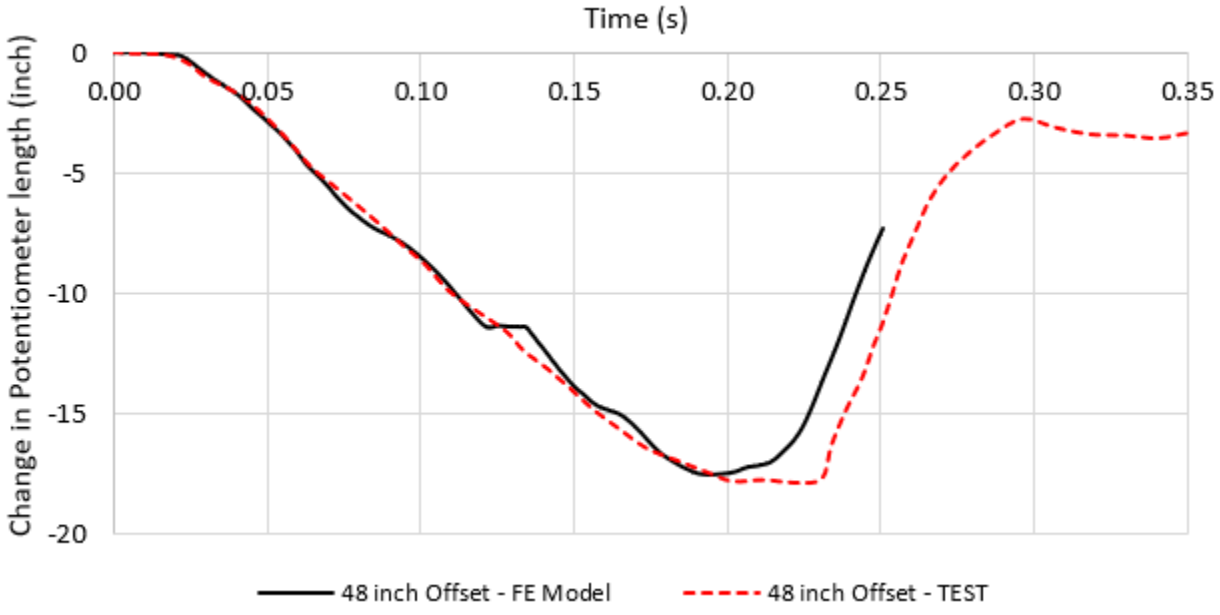

Figure 139. Comparison of String Potentiometer Length vs Time, 48 inch Offset from Center of Tank

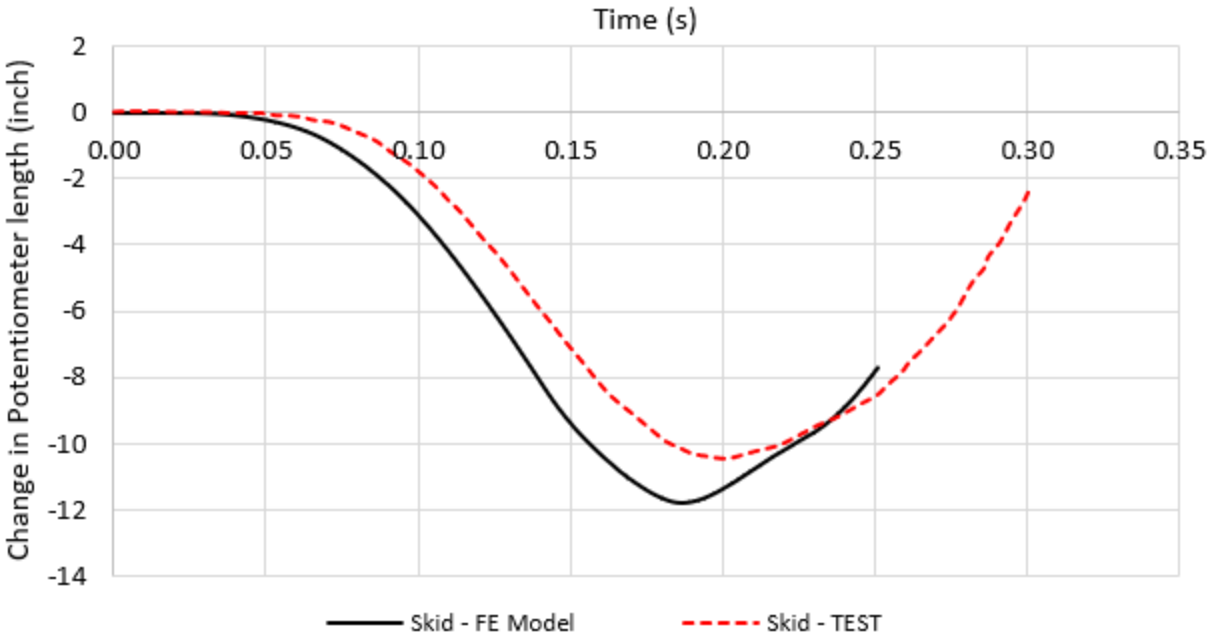

Figure 140. Comparison of String Potentiometer Length vs Time, Skid

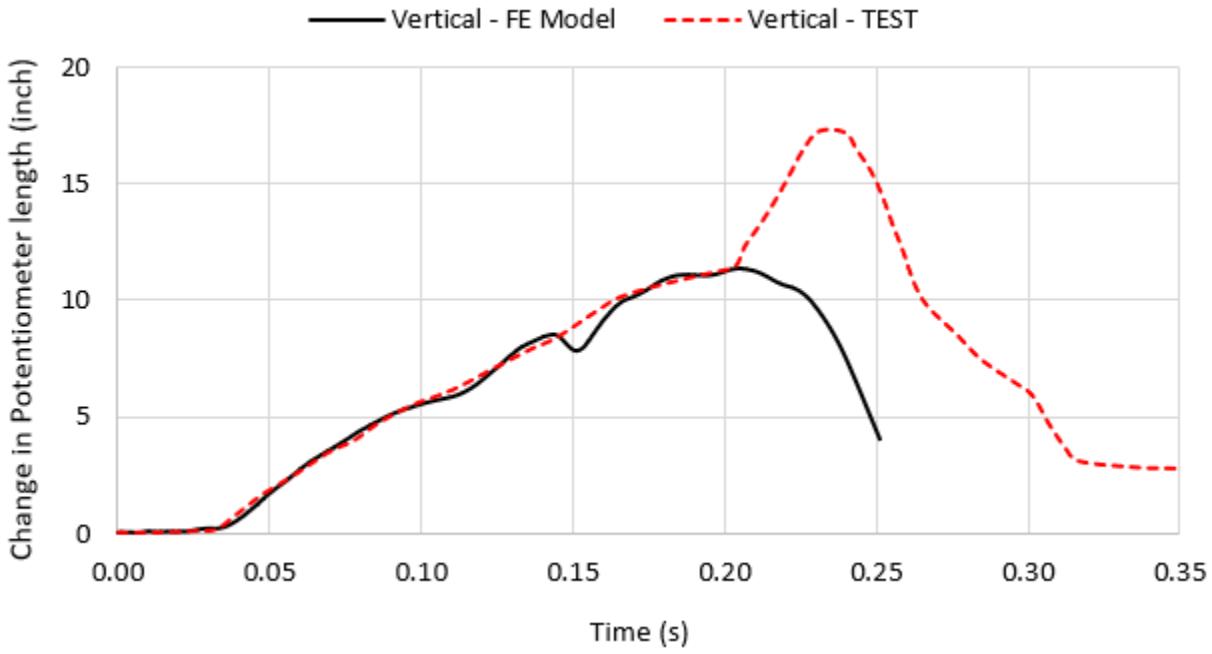

Figure 141. Comparison of String Potentiometer Length vs Time, Vertical

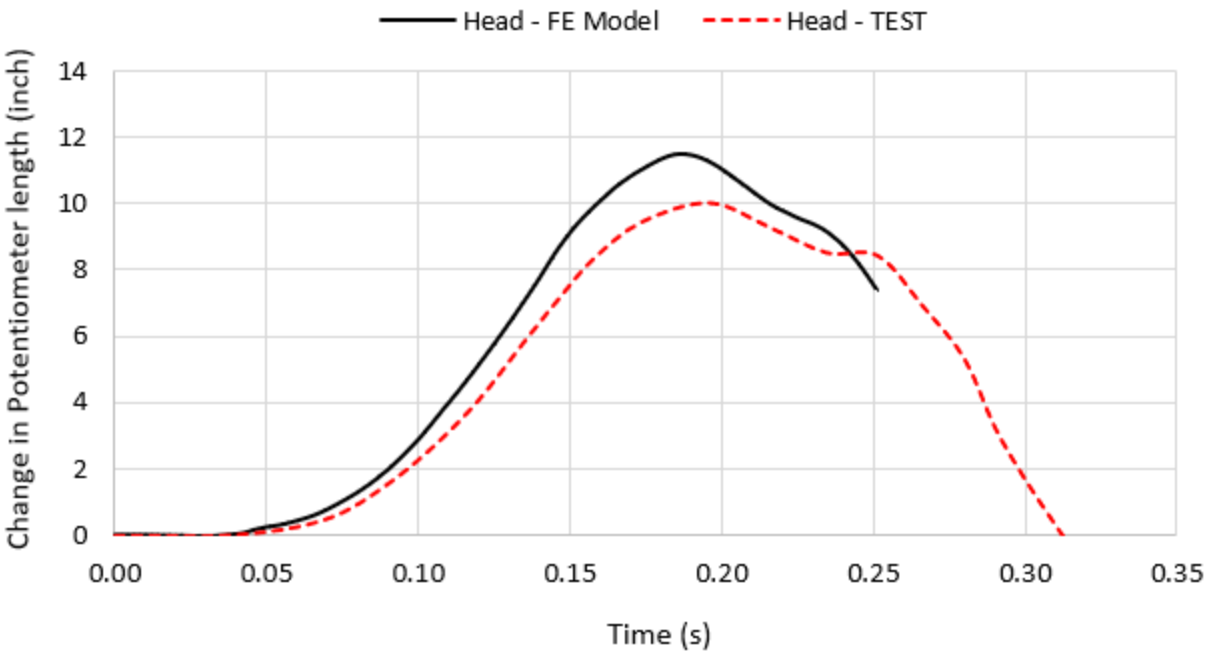

Figure 142. Comparison of String Potentiometer Length vs Time, Head

Appendix D.
Polyurea Material Model

The engineering stress-strain data used to develop the Abaqus material model for the polyurea used in the internal liner assessment is provided in Table 43 and shown in Figure 143. A simplified nonlinear elastic-plastic material model was used to represent the polyurea, where it is assumed that the plastic strain component is non-recoverable. This was considered a reasonable simplification since the primary concern with respect to the integrity of the liner under impact loading is during the initial loading phase and not during recovery. To include plasticity within Abaqus, the stress-strain points past yield must be input in the form of true stress and logarithmic plastic strain. The logarithmic plastic strain required by Abaqus can be calculated with the equation below:

$$\varepsilon_{ln}^{plastic} = \ln(1 + \varepsilon_{eng}) - \frac{\sigma_{true}}{Emodulus}$$

With $\varepsilon_{ln}^{plastic}$: logarithmic plastic strain

$\ln(1 + \varepsilon_{eng})$: total true strain

$\frac{\sigma_{true}}{Emodulus}$: elastic strain (always recoverable part of strain)

$Emodulus$: Young's modulus

The first data point must always correspond to the yield stress (in this case 0.2 ksi, with logarithmic plastic strain = 0) with subsequent stress-strains calculated using the relationships above. Implementing this approach rendered the true stress – logarithmic plastic strain data shown in Figure 144. This is the data used within the Abaqus material model. Other relevant material data is provided in Table 44. Ductile damage behavior was defined to facilitate element deletion. For simplicity, this was assumed to be independent of stress-triaxiality, and a very small displacement to failure upon reaching the fracture strain was assigned to enforce a brittle response.

A single element tensile test was performed on a 0.125-inch-thick by 0.5-inch-wide by 2-inch-long, 4-node fully integrated shell element (S4) to verify the performance of the material model. The initial and deformed shape of the element just prior to failure is shown in Figure 145, with the engineering stress-strain curve extracted from the analysis shown in Figure 146. Very good agreement was obtained between the Abaqus single element test and the experimental stress-strain curve.

Table 43. Polyurea Input Engineering Stress-strain Data

Engineering Strain (-)	Engineering Stress (ksi)
0.000	0.000
0.007	0.200
0.658	2.742
1.400	2.743
1.600	2.800
1.950	2.900
2.250	3.000
2.650	3.150
2.950	3.280
3.250	3.400
3.630	3.520
4.200	3.750
4.900	4.000

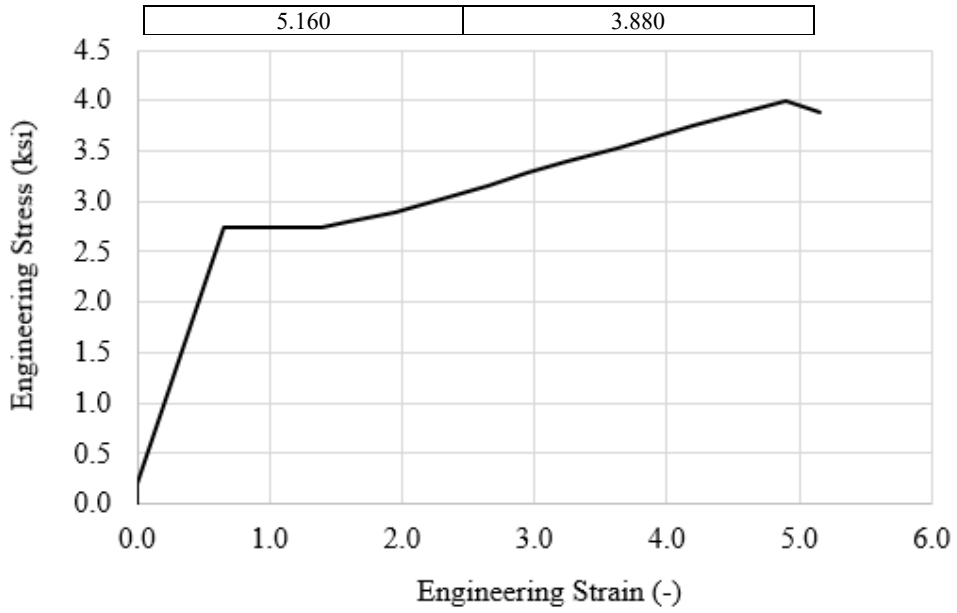

Figure 143. Polyurea, Input Engineering Stress-strain Curve

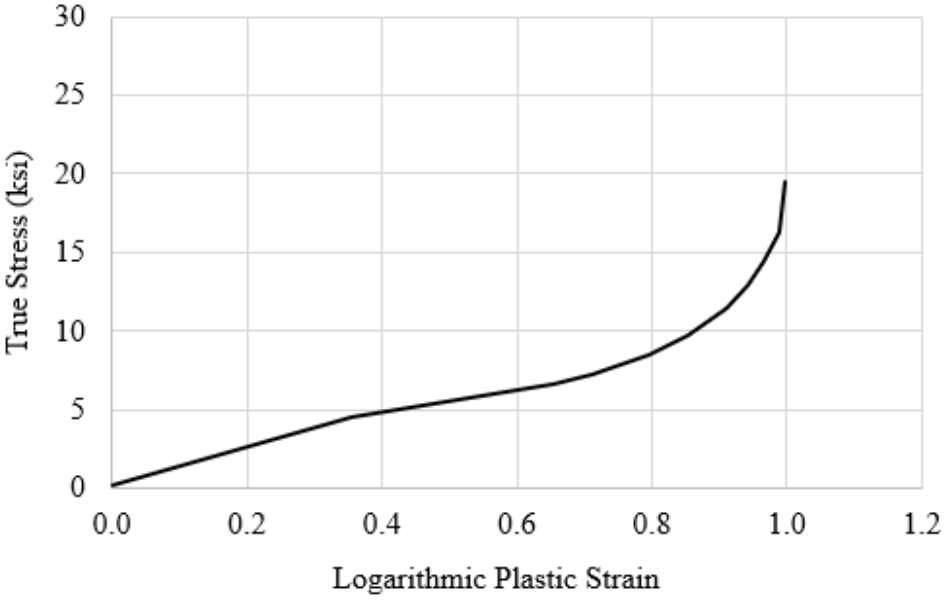

Figure 144. Polyurea, Abaqus True Stress – Logarithmic Plastic Strain Curve

Table 44. Polyurea Material Properties Used in FE Model

Property	Value
Modulus of Elasticity	30,000 psi
Yield Stress	200 psi
Poisson's Ratio	0.49
Density	1.25 lbf*s^2/in
Logarithmic plastic strain to failure	1.024
Damage evolution (linear displacement)	1E-05 in

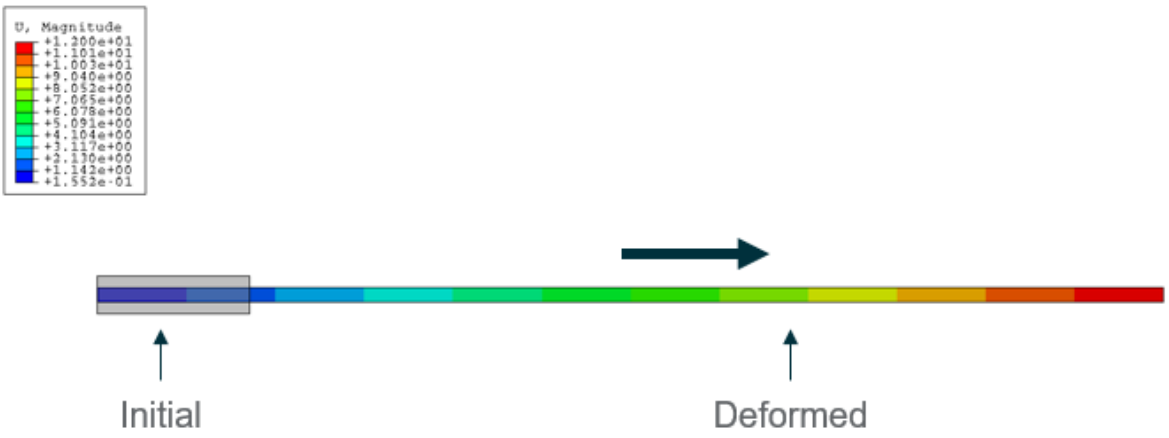

Figure 145. Displacement Response of Polyurea Single Element Test

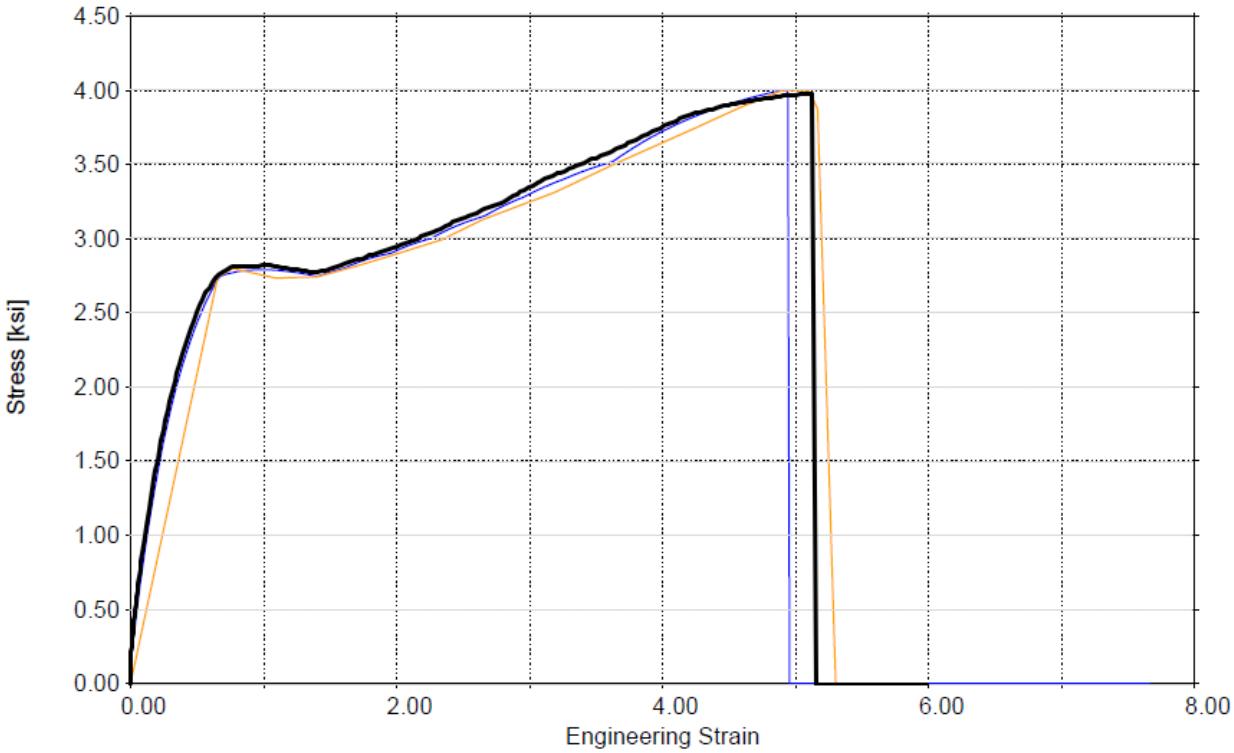

Figure 146. Engineering Stress-Strain Curve Obtained from Abaqus Polyurea Single Element Test (black line) Compared to Experimental Data and NLFlex Single Element Test Results

Abbreviations and Acronyms

ACRONYM	DEFINITION
AAR	Association of American Railroads
AM	ArcelorMittal
ANSI	American National Standards Institute
ARA	Applied Research Associates, Inc.
ASTM	American Society for Testing and Materials
ATCCRP	Advanced Tank Car Collaborative Research Program
B-W	Bai-Wierzbicki
DENT	Double-Edge Notch Tension
DOT	Department of Transportation
FE	Finite Element
FEA	Finite Element Analysis
FRA	Federal Railroad Administration
GTN	Gurson Tvergaard Neddleman
HSLA	High Strength-Low Alloy
KE	Kinetic Energy
LNG	Liquified Natural Gas
MOC	Memorandum of Cooperation
MPC	Multi Point Constraint
MPC	multi-point constraint
NGRTCP	Next Generation Rail Tank Car Program
NPRM	Notice of Proposed Rulemaking
NTSB	National Transportation Safety Board
PHMSA	Pipeline and Hazardous Materials Safety Administration
PIH	Poison Inhalation Hazardous
SPH	Smooth Particle Hydrodynamics
SWRI	Southwest Research Institute
TC	Transport Canada
TIH	Toxic Inhalation Hazmat
TT	Thornton Tomasetti, Inc.

ACRONYM	DEFINITION
TTCI	Transportation Technology Center, Inc.
UHSS	Ultra-High Strength Steels
UP	Union Pacific
USDOT	U.S. Department of Transportation
UTLX	Union Tank Car Company